Deciphering UV Spectroscopy on Earth and Mars

by

Ryan Roppel

B.S. Chemical Biology, University of California Berkeley, 2013

Submitted to the Graduate Faculty of

the Dietrich School of Arts and Sciences in partial fulfillment

of the requirements for the degree of

Doctor of Philosophy

University of Pittsburgh

2023

UNIVERSITY OF PITTSBURGH

DIETRICH SCHOOL OF ARTS AND SCIENCES

This dissertation was presented

by

Ryan Roppel

It was defended on

December 1st 2023

and approved by

Dr. Sanford A. Asher, Distinguished Professor of Chemistry, Department of Chemistry,

University of Pittsburgh

Dr. Jennifer Laaser, Assistant Professor, Department of Chemistry, University of

Pittsburgh

Dr. Sean Garrett-Roe, Associate Professor, Department of Chemistry, University of

Pittsburgh

Dr. Rohit Bhartia, Chief Technology Officer, Photon Systems, Inc.

Deciphering UV Spectroscopy on Earth and Mars

Ryan Roppel, PhD

University of Pittsburgh, 2023

Spectroscopy consists of a variety of techniques that often probe materials with light. Light can be absorbed and excite particular chromophores that give insight into electronic structure or can be scattered that gives insight into vibrational structure. To enable successful measurements, one needs to understand the technology behind the spectroscopy and what parameters can be adjusted to affect signal to noise. The thesis presented here illustrates how absorption, fluorescence, and Raman spectroscopies can all be employed to determine the structure of molecules on Earth and how we can use analog datasets to predict what we observe on Mars.

Table of Contents

List of Tables

List of Figures

1.0 Introduction

1.1 Scope

This thesis will be comprised of only four chapters. Chapter 1 will provide a framework to understand two manuscripts: Chapter 2, which discusses why continuous wave lasers are ideal for Raman spectroscopy and Chapter 3, which summarizes the findings of fluorescence and Raman signatures on Mars using the SHERLOC instrument aboard the Perseverance rover. Chapter 4 will summarize the thesis and provide further outlooks on the field of UV (ultraviolet) spectroscopies.

1.2 Why use deep UV resonance Raman and luminescence spectroscopies?

Deep UV resonance Raman and luminescence spectroscopies can be employed in a variety of fields from biological sciences [65, 61], homeland security [44], and even in geological sciences [105, 107]. However, deep UV Raman adoption has not seen widespread adoption compared with other analytical techniques in part due to a similar, but often misunderstood difficulty found in visible/IR Raman: quantification or identification of certain molecules in complex mixtures. Both visible and deep UV Raman spectroscopy are ideal at identifying bulk chemicals with high specificity due to characteristic vibrational bands. But, deep UV Raman can enhance certain molecules, which can reduce spectral complexity and increase signal to noise, only if the molecule of interest has a chromophore in the deep UV. Understanding electronic structure, and what chromophore to excite is paramount for success in any resonance Raman measurement.

Using a continuously tunable CW laser, like mentioned in Chapter 2, can allow one to select any wavelength needed to enhance a certain molecular chromophore. Additionally, since the laser is continuous wave, the likelihood of non-linearities, which can be common with high-pulse energy lasers is reduced. Ultimately for quantification to succeed, a linear

calibration is required, which requires linear spectroscopic measurements made easier with CW light.

Deep UV spectroscopies can aid in searching for signs of life on another planet by enhancing certain chromophores that are associated with the building blocks of life on Earth. Many aromatic molecules are resonantly enhanced with deep UV light, and are a reasonable candidate to search for on Mars as discussed in Chapter 3. Because the retrieval of materials outside of Earth is expensive, choosing specimens that contain unique organics through non-contact and non-destructive measurements for eventual return to Earth is essential. Once on Earth, an infinite number of analytical techniques can be employed on the samples to discover if life and the chemistries on Earth are unique or ubiquitous across planets.

Analytical chemistry is based on using techniques to identify and/or quantify molecules of interest. The lack of familiarity with deep UV Raman and the incorrect assumptions when compared with visible Raman challenge the success of the field. But the more people hear about deep UV spectroscopies used in high-impact systems and the more commercial systems that are available to solve existing problems, the more successful deep UV spectroscopies will be.

1.3   How does light interact with matter?

All light/matter interactions can essentially be characterized by either absorption or scattering phenomena [59].

In absorption, a photon that is the same energy as an electronic transition of a molecule will excite the molecule from the ground electronic state into an excited electronic state [48]. The molecule, now in a transient excited state, will try and reduce the excess internal energy to return to the ground state [48]. Commonly in condensed matter (liquids and solids), the molecule will return to the ground state through a process known as non-radiative decay and release heat [99]. The molecule can also return to the ground state through a radiative process: fluorescence or phosphorescence [48]. In fluorescence, the molecule usually decays from the lowest vibrational, electronic excited state to some vibrational, ground electronic

state and releases a photon whose frequency matches the energy gap [48]. Phosphorescence is similar to fluorescence in that a molecule emits a photon after returning to the ground state, but in the excited state, the molecule has the same spin as the ground state and must change its spin occupancy before returning to the ground state [48]. The delay in a spin change usually results in phosphorescence being much slower than fluorescence [48].

In scattering, a photon interacts with a molecule that promotes the molecule from the ground electronic state into an intermediate, virtual state [31]. The virtual state is a perturbed ground state of the molecule that has a very short lifetime [85]. The molecule usually returns to the ground state without a change in energy and the scattered photon does not experience a change in energy [31]. If the size of the molecule is similar to the wavelength of light, this process is known as Rayleigh scattering; if the size of the molecule is much larger than the wavelength of the photon, it is known as Mie scattering [132, 136]. Sometimes, the scattered photon is not the same wavelength as the incident photon, as the molecule returns to the ground electronic state in a different vibrational state [31]. This inelastic phenomenon known as Raman scattering can exist in two forms: anti-Stokes, where the photon has more energy than the incident photon energy or Stokes, where the photon has less energy than the incident photon energy [31]. Stokes Raman scattering is more common because molecules typically exist in the ground electronic, ground vibrational state [31]. These scattering phenomena are illustrated in Figure 1.

Resonance Raman scattering is a special case of the "normal" Raman scattering mentioned above, where the virtual state is a perturbed intermediate state [83]. The advantage of this is an enhancement, or an increase in the probability of a Raman photon being generated [83]. This enhancement is because the excited state is a real electronic state instead of a perturbed state [83]. The likelihood of an incident photon being resonantly Raman scattered increases proportionally to the increase in the absorption cross section, or the probability that an incident photon will be absorbed [86].

It is important to note that although the probability of a Raman photon increases when coupled with an electronic transition, the photon can still be absorbed by the same molecule, a process known as self absorption [52]. Self absorption plays a major role in resonance Raman spectroscopy because the sample excitation volume will decrease with increasing
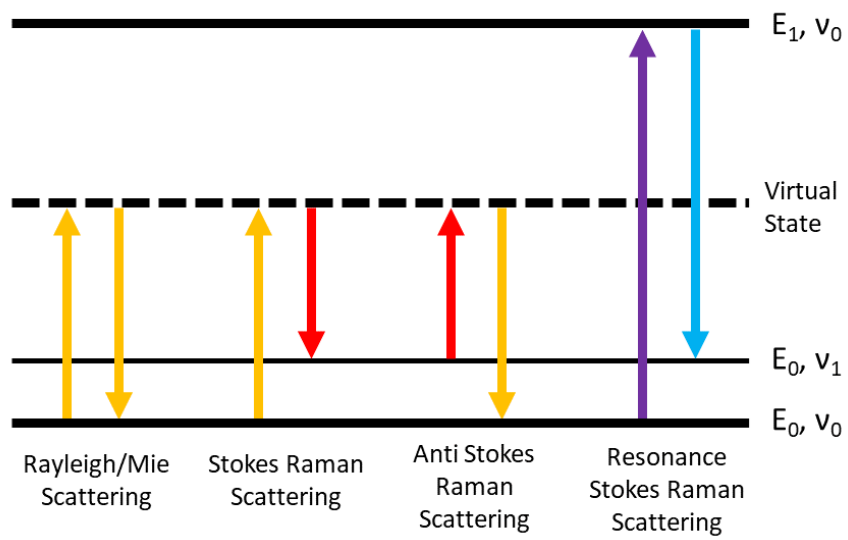
Figure 1: Energy Level Diagram for Light Scattering. The arrow color relates to the wavelength of light, with red being longer wavelengths and purple being shorter wavelengths.

absorption cross section [52]. When measuring mixtures of both resonant and non-resonant molecules, the resonant molecules will have a greater signal intensity than the non-resonant molecules, but the absolute raw Raman signal as measured on a detector depends on a variety of factors that would likely fill an entire volume of textbooks, and will only be briefly discussed in this thesis [49, 56, 83, 91, 100].

1.4 Why use deep UV light?

The dependence on the wavelength of light used can cause significant perturbations within a molecule [84]. The scattering intensity depends on $\frac{1}{\lambda^4}$, with λ being wavelength, which means that at shorter wavelengths, the scattering intensity increases [91]. Section 1.3 also already mentioned how illuminating a chromophore can also increase the resonance Raman scattering intensity. Additionally many molecules fluoresce strongly in the visible wavelength range, which is more intense than Raman scattering, causing increases in the background or out-emitting the Raman intensity altogether [3].

Many biological molecules such as proteins, nucleotides, and aromatics have their strong absorption cross sections in the deep UV [16]. With increased absorbance, non-radiative decay can cause sample heating, so the light intensity can be critical to avoid non-linear phenomena as will be discussed in Chapter 2. Significant efforts have been undertaken to investigate the origin of life and its potential existence on other planets, so deep UV excitation is ideal for studying organic molecules as will be discussed in Chapter 3.

Because of the relatively weak Raman scattering signals from molecules, an intense light source such as a laser is typically used [104]. Laser safety is critical to maintaining a safe workplace environment. Lasers are never operated at eye level, interlocks and beam blocks/curtains prevent stray reflections from glancing the user, safety glasses specific to the wavelength used protect eyesight as well as gloves, and long-sleeved shirts and long-sleeved pants protect the skin [77]. Regrettably, accidents still occur, but using deep UV lasers could be considered safer than traditional visible or IR lasers. For human vision, visible light passes through the lens and is focused on the retina [120]. If a person was illuminated

by a visible wavelength laser, blindness could occur [77]. UV light is absorbed by the lens, before it reaches the retina, significantly reducing the chance of permanent damage [120]. A lens replacement is not ideal, but is commonly performed with patients with cataracts [120]. Additionally, most plastic safety glasses are made of polymers that strongly absorb deep UV light [62].

1.5   How or what instrumentation is used?

1.5.1   UV-Vis Absorption Spectrometers

To probe electronic molecular structure, UV-Vis (ultraviolet-visible) absorption spectroscopy is widely used. This involves illuminating a sample with monochromatic light and measuring the transmission of light through the sample. The Beer-Lambert Law describes the light interaction: $\log \frac{I_0}{I} = A = \epsilon \ell c$, where I_0 is in incident light intensity, I is the transmitted light intensity, A is the absorbance, ϵ is the molar absorptivity, ℓ is the path length, and c is the concentration [60]. The molar absorptivity is then plotted against wavelength; increases in molar absorptivity will yield broad bands that correspond to the various electronic transitions [60]. Sometimes narrower bands within an electronic band will appear which can indicate both vibrational and electronic structure [60].

A typical UV-Vis absorption spectrometer is a Czerny-Turner monochromator design [57]. Monochromatic light illuminates a sample and light not absorbed by the sample is focused onto the slit of the spectrometer [57]. The slit reduces the light intensity, and can increase the resolution of the spectrometer up to the diffraction limit [57]. The light is then collimated onto a grating, dispersed, then focused onto a detector [57]. Because the detector is generally broadband, the grating is angle-tuned which allows specific wavelengths of light to illuminate and be read by the detector [57]. Newer multichannel detectors can measure all wavelengths simultaneously without moving the grating. Variants of the Czerny-Turner design exist including Littrow, which retro-reflects the light or Wadsworth, which uses curved gratings [57]. The excitation light source is typically halogen or xenon in the visible and

6

deuterium in the UV that scans through different wavelengths by a tilting grating [58]. Newer designs can also use a laser driven light source, which is a laser focused in a xenon bulb that generates broadband UV-Vis light that can be easily collimated [28].

1.5.2 Fluorescence/Phosphorescence Spectrometers

Fluorescence and phosphorescence can also be used to probe electronic structure. This involves illuminating a sample with monochromatic light and measuring the emission at a 90 degree incidence [55]. Since a single monochromatic light source can result in broadband emission, the emitted light is typically dispersed, or separated before being read on a detector [55]. If multiple excitation wavelengths are used, the excitation wavelength is plotted against the emission wavelength, which results in a 2D plot [55]. The contours would represent various electronic transitions [55]. A single excitation wavelength could also be used, which would result in a plot similar to the UV-Vis absorption, but would typically be red-shifted due to Kasha's Rule, which states that emission comes from the lowest electronic excited state [68]. An important parameter known as the fluorescent quantum yield is typically reported, ϕ, which is the ratio of the emission intensity to the illuminated light intensity [55]. Detectors can also be time-gated, which measures the fluorescence intensity decay over time known as τ [55].

A typical fluorescence spectrometer will be very similar to a UV-Vis absorption spectrometer with the large difference being that the excitation beam passes through the sample but the detector is 90° to the excitation beam to reduce Rayleigh scattering from the excitation beam [55].

1.5.3 FTIR Spectrometers

To probe the vibrational structure of a molecule, FTIR (Fourier Transform Infrared) spectroscopy or Raman spectroscopy are typically used. Unlike the two electronic spectroscopies in Section 1.5.1 and Section 1.5.2 that give rise to broad bands that aren't extremely diagnostic, vibrational structure can give a more unique fingerprint of a small molecules.

FTIR spectroscopy is an IR absorption technique and not used for any of the work

7

presented in this thesis, but is important to include as it's widely used for vibrational spectroscopy. Although molecules are vibrationally excited by IR light, IR light detection is challenging because detectors are not sensitive to IR as quantum efficiency drops off significantly after 1000 nm [50]. FTIR spectroscopy can be based on a Michelson Interferometer, where a beam of monochromatic IR light passes through a sample and is split into two halves: one that goes directly to a detector and the other path that is delayed by reflecting off a mirror before recombining with the first beam at the detector [54]. The mirror moves some distance over a period of time, which generates an interferogram on the detector. A Fourier transform is then applied to convert to frequency space [54].

1.5.4   Raman Spectrometers

Raman spectrometers are built in several different configurations. All modern configurations require a monochromatic laser to excite a sample [32]. Typically excitation is done in a back-scatter (180°) orientation to reduce contributions from self-absorption [52]. The simplest design would be a Czerny-Turner monochromator design, but requires a steep edge long pass filter at the entrance of the spectrometer to remove the Rayleigh scattered light that is much more intense than the Raman scattered light [32]. There is no way to remove this light as the scattering is an almost instantaneous process [85]. The light is then focused on the slit, to reduce light intensity and increase resolution, where it is collimated onto a grating, dispersed, and focused on a detector [32].

Another design is known as a double monochromator, where two single monochromators are placed in series in an additive configuration [32]. This configuration is not used typically to increase spectral resolution, but to instead reduce stray light, or any light other than the Raman signals of interest [32].

Finally, is a triple monochromator, where one spectrograph disperses the light, then another operates in a subtractive (undispersive) configuration, and finally another that disperses again [32]. This is a very versatile configuration as it allows Raman detection without using a Rayleigh rejection filter [32]. The major downside is the loss of signal intensity due to the large number of optics, but can be the only option when operating a tunable excitation

source or when Rayleigh rejection filters are not available for purchase at a specific wavelength [117]. Modern holographic gratings and optics can help maintain at least one third of the throughput as that of a single monochromator [5]. For deep UV Raman detection, a fluorescent coating is typically applied to the detector which improves sensitivity and evens out the detector wavelength sensitivity [95]. Although deep UV Raman doesn't generally suffer from fluorescence contributions, a time-gated detector can be used to selectively reduce a fluorescence background and enhance the Raman signal [70].

2.0 Continuously Wavelength Tunable, Continuous Wave Laser Ideal for UV Raman Spectroscopy

This chapter includes the full text from the manuscript of the same name was published by the Journal of Raman Spectroscopy on November 20, 2023. The article is copyrighted by John Wiley and Sons, Ltd. but licensed for use in this thesis. The author list is: Ryan D. Roppel and Sanford A. Asher.

2.1 Abstract

We utilize a novel, high-power, tunable, continuous wave (CW) deep UV laser to measure resonance Raman spectra of phenolate solutions with high signal to noise ratios (SNR). In UV resonance Raman (UVRR), increased coupling of the excitation light with a chromophore can transfer molecules into excited states that cause increased heating and photochemistry. Deep UV lasers have traditionally utilized high peak powers to enable efficient single-pass non-linear conversion from visible into near infrared light. Non-linear phenomena such as the formation of transient radical species, Raman saturation, thermal heating, and dielectric breakdown can introduce extraneous light sources that can complicate the interpretation of the Raman spectrum. Dielectric breakdown can increase the baseline, increase noise, and sometimes saturate the detector, preventing Raman detection.

Spontaneous Raman scattering intensities should scale linearly with the excitation light intensity. However, this linear behavior does not always occur with pulsed laser excitation. This occurs because stimulated Raman scattering can cause a superlinear intensity response, or transient absorption can cause sublinear intensity responses. CW laser excitation excites samples with electric fields that are much lower than typical pulsed laser excitation. This eliminates the non-linear responses. The geometry of our new CW laser enables high gain in the harmonic generation cavities that achieve high harmonic generation efficiencies. Average power in the deep UV is >30 mW for wavelengths as short as 206 nm. In the work here, we

demonstrate that CW excitation is ideal for resonance Raman measurements in general to reduce spectral complexity.

2.2 Introduction

Ultraviolet resonance Raman spectroscopy (UVRR) is often a non-destructive, non-contact technique that probes molecular vibrational modes [85, 91]. This spectroscopy has been used in a wide variety of applications. For example, defense organizations have begun to use UVRR for standoff detection of explosives [44, 41]. UVRR has been used to probe the primary, secondary, and tertiary structures of proteins to study the vibrational modes associated with aromatic amino acid side chains [65, 74], the peptide backbone [20, 75], and interactions between side chains [67, 61]. Materials science applications have used UVRR to probe the hybridization of carbon in diamonds and amorphous carbon structures [14, 71]. The most recent NASA rover, Perseverance is attempting to search for signs of life on Mars using UVRR [112].

One of the main benefits of using UVRR is the significant enhancement of the Raman signal due to the resonance effect, which occurs when the excitation wavelength matches the electronic transition of the molecule [85]. This can result in a signal increase of several orders of magnitude, allowing for the detection of low-concentrations of weakly scattering species [76]. Another advantage of UVRR is the reduction of fluorescence interference, which is a common problem in visible Raman spectroscopy [142, 97]. Fluorescence can compete or overwhelm the Raman signal, especially for organic or biological samples [128]. By using UV excitation, the fluorescence emission is shifted to longer wavelengths, away from the Raman spectral region. Furthermore, the Raman scattering intensity is a function of ν^4, where shorter wavelengths scatter more efficiently [82].

Even with the advantages of UV excitation, Raman ultimately require high laser fluences that produce a large number of photons to excite the sample. The most common method for generating UV light is through nonlinear frequency conversion of infrared (IR) and visible light. Traditionally, nanosecond or picosecond pulses are required to achieve high harmonic

conversion efficiencies [90].

Pulsed lasers are not ideal excitation sources for UVRR and have been shown to produce a variety of spectra-degrading phenomena. For example, photochemical transients such as the phenoxy radical are easily formed by exciting a solution of phenol that generate additional bands that can overlap with the Raman bands of interest [64, 19]. Raman saturation can depopulate the ground electronic state and reduce the intensity of the normal Raman bands [4, 66]. Thermal heating can activate certain photochemical pathways, degrading the sample, and/or adding additional transient bands [46]. At worst, the sample can be ionized into a plasma, which generates atomic emission lines that have greater intensities than Raman bands [110], causing a high spectral background. High laser power densities lead to non-linear phenomena.

Lower power densities, found in CW lasers, are key to reducing or eliminating non-linear results. Major advances to improve stability and achieve high average powers in CW lasers involve using feedback mechanisms, such as wavelength locking or power regulation, that monitor and adjust the output parameters as local environmental conditions change. For example, the center wavelength drift from a Ti-Sapphire laser can be compensated by measuring the output wavelength with an interferometer and adjusting the lasing cavity length with a piezoelectric stage [69]. Frequency stabilization can also be achieved by modulating the output of the laser and detecting the throughput of a known gaseous reference cell absorption line [137]. Feedback systems such Pound-Drever-Hall stabilization reduce the linewidths of lasers as they compensate for ambient thermal fluctuations [98]. By measuring laser output power on a power meter, a proportional-integral-differential (PID) controller can provide closed-loop feedback to adjust the laser current and achieve stable output powers [134].

In this work, we describe a new continuously tunable continuous wave deep UV laser for resonance Raman spectroscopy and demonstrate how excitation irradiance can significantly perturb the UVRR spectra of phenolate.

2.3 Methods

Solutions of phenolate were made with reagent grade phenol (EM Science) and adjusted to pH 13 using sodium hydroxide (Sigma Aldrich). 1M sodium perchlorate (Sigma Aldrich) was used as an internal intensity standard.

Two separate 266 nm lasers (pulsed and CW) excited the samples. The pulsed laser was the FHG of a Coherent Infinity 3 nanosecond-pulsed 100 Hz Nd:YAG. The CW laser was a Spectra-Physics Mixtrain-Wavetrain. The focused laser beam diameters were estimated to be ~ 400 μm as measured by burn paper.

Three spectrometers were used to measure UV absorbance, Raman, and LIBS (Laser-Induced Breakdown Spectroscopy) emission: a Varian Cary 5000 spectrophotometer, a custom deep UV optimized triple monochromator as we previously discussed [5] and an Ocean Optics HR4000 spectrometer.

Spectra were plotted, calibrated, and analyzed in Spectragryph [92]. Raman spectra were frequency calibrated with neat acetonitrile.

For both the Raman and LIBS emission measurements, the phenolate solution was pumped into an open air non-circulating ~ 1 mm diameter smooth, cylindrical flow stream. The solution was at room temperature ~ 22 °C.

2.4 Results

Figure 2 shows the UV absorbance of the phenolate solution at pH 13. At 266 nm, the excitation wavelength falls between two electronic transitions, the $^1L_a(S_2)$ and the $^1L_b(S_1)$ [64]. In the resonance Raman spectrum excited with 100 mW of CW power in Figure 3, we can see a variety of normal modes enhanced by two different electronic transitions. The $^1L_a(S_2)$ transition enhances the normal modes at 1582, 1162, 1015, 984, and 810 cm^{-1} [64]. We hypothesize that the $^1L_b(S_1)$ transition enhances the normal modes at 1556, 1260, and 835 cm^{-1} as they were not seen with 245 nm excitation, but only here with 266 nm excitation. The sodium perchlorate internal intensity standard occurs at 932 cm^{-1}. We also measured

the CW 266 nm resonance Raman spectrum with 10 mW of average power. We did not observe any spectral band or intensity differences than with the higher 100 mW average power. We conclude there is no discernible non-linear response in this CW power range as shown in Figure 11.
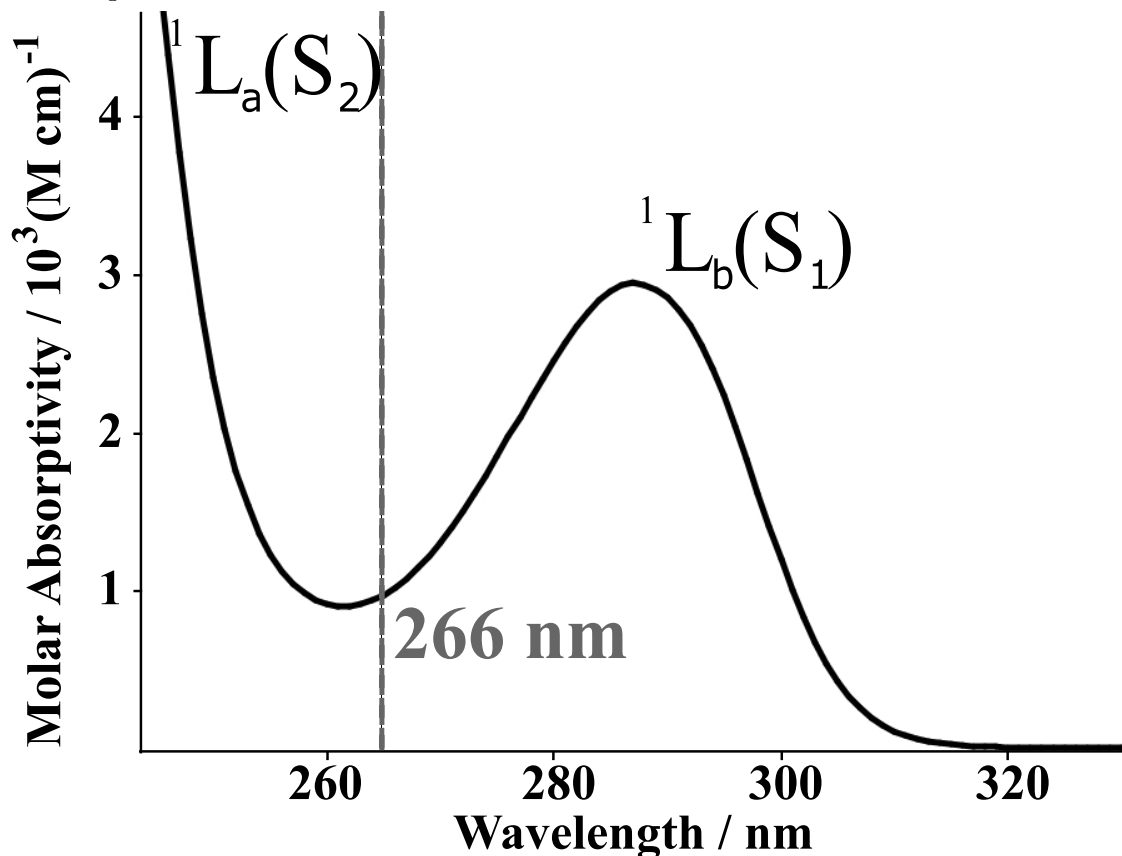
Figure 2: UV absorbance of a 1 cm path length phenolate solution at pH 13. The excitation wavelength of 266 nm has been highlighted for clarity. 266 nm excitation falls between the $^1L_a(S_2)$ and $^1L_b(S_1)$ transitions.

With pulsed excitation, numerous changes occur in the Raman spectrum. At only 1 mW of average power, the Raman spectrum looks nearly identical to that of the CW excitation, but the 1582 cm^{-1} band has decreased in intensity relative to the 1556 cm^{-1} band. Additionally, the overall signal to noise is poor because of our lower average excitation power used. When we increase the average power to 46 mW, we observe significant changes where several new bands are observed at 1138, 1155, 1392, 1413, and 1502 cm^{-1} in addition to changes

in intensity of some of the phenolate normal modes. The new bands observed are primarily due to the formation of the phenoxy radical [64]. At 70 mW of average power, the Raman spectrum is dominated by a high baseline, caused from the formation of a LIBS sample plasma that emits in the deep UV. The emission spectrum is plotted in Figure 4. Three atomic emission lines are observed at 589.7 nm, 657.1 nm, and 778.3 nm. These correspond to atomic lines of sodium, hydrogen, and oxygen, respectively [72]. A solution containing only water yielded an identical spectrum as that of the measured phenolate, but without a sodium line as seen in Figure 12. The observed high baseline nearly overwhelms the Raman spectrum of phenolate. The highest intensity band at 1502 cm^{-1}, derives from the transient phenoxy radical, not the phenolate molecule in solution.

2.5   Discussion

Under pulsed excitation we observe three different phenomena that confound the resonance Raman spectrum of phenolate. These include band intensity changes, the formation of radical bands, and dielectric breakdown. The first evident spectral change is observed at the lowest pulsed average excitation power of 1 mW. This is most evident for the 1556/1582 cm^{-1} bands corresponding to the C-C ring stretching modes [96]. The 1556 cm^{-1} band intensity increases relative to the 1582 cm^{-1} band as described in Table 1. We observe that with increased pulsed excitation power, the band intensity ratio increases non-linearly from 0.82 to 1.83. At the highest 70 mW pulsed power, the LIBS plasma make quantification of band intensities difficult due to the variability in baseline.

There are two possible explanations for the changes in intensities. First, a phenoxy radical band at 1556 cm^{-1} could overlap with the existing phenolate band, to add to the overall intensity of the phenolate band. Alternatively, laser induced sample heating could change the oscillator strength, enhancing one phenolate band over the other [109]. This is an interesting case where changing the excitation power changes relative band intensities, without changing wavelength.

The band intensity does not scale linearly as would be expected in simple spontaneous
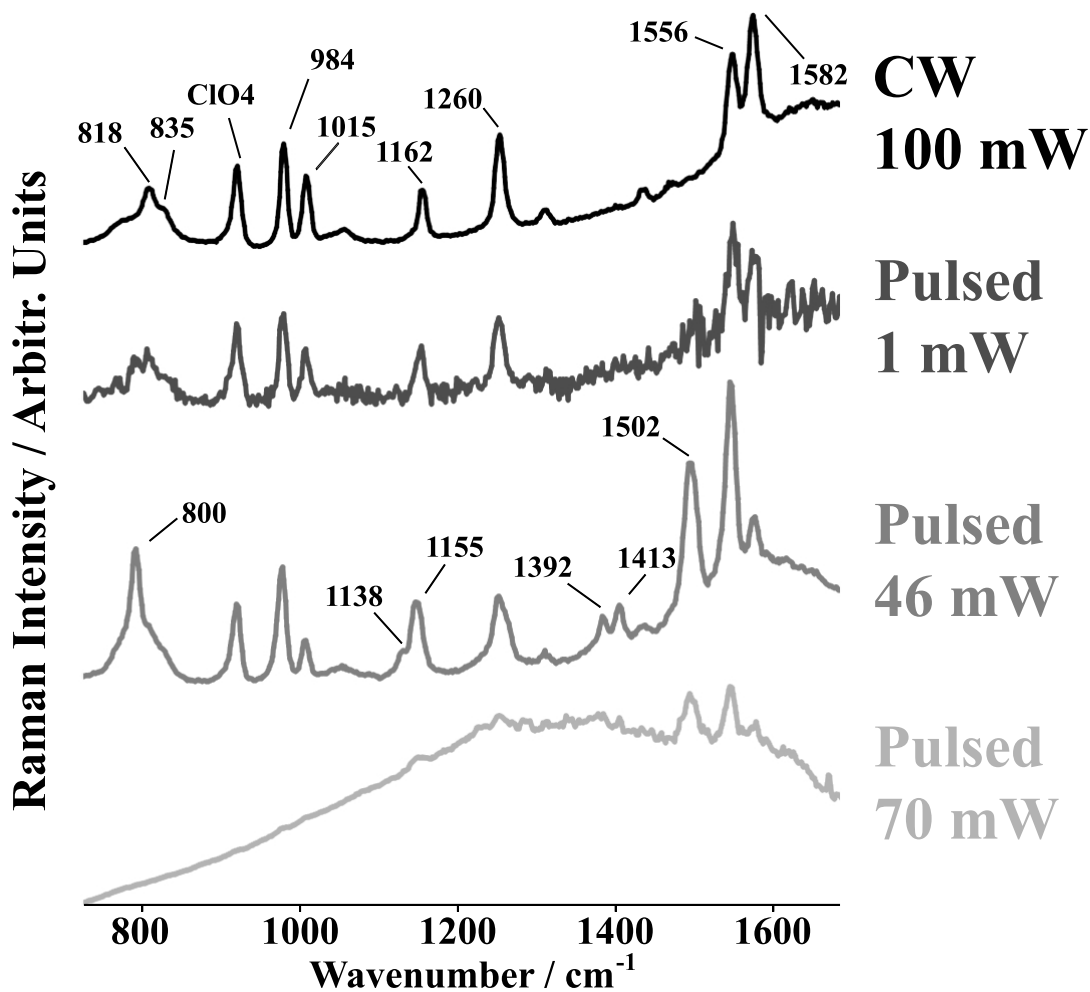
Figure 3: Resonance Raman spectra of 5 mM phenolate solutions at pH 13 collected at various average powers: 100 mW CW, 1 mW pulsed, 46 mW pulsed, and 70 mW pulsed. Key phenolate bands are identified in 100 mW CW spectrum and key phenoxy radical bands are identified in the 46 mW pulsed spectrum. Sodium perchlorate, labeled as ClO4, was used as an internal intensity standard.

Raman. At 266 nm, we are in pre-resonance between two electronic transitions, and so the resonance Raman intensities become very sensitive to small changes in sample temperature.

Laser, Power	Intensity Ratio 1556 cm^{-1}/1582 cm^{-1}
CW, 100 mW	0.82
Pulsed, 1 mW	1.16
Pulsed, 46 mW	1.83
Pulsed, 70 mW	1.74

Table 1: The ratio of band intensities of the phenolate ring stretching mode. As laser peak power increases, the 1556 cm^{-1} band increases in intensity relative to the 1582 cm^{-1} band. With 70 mW pulsed, the signal to noise has degraded substantially which causes the intensity ratios to have higher error.

More evident spectral changes occur due to the formation of the phenoxy radical transient bands. Of the eight easily identifiable Raman bands of phenolate, five phenoxy radical transient bands appear to overlap with the phenolate bands. Phenolate can be difficult to quantitate in a mixture due its large number of bands, but extra complexity occurs when the phenoxy radical bands are also present. Deconvolution of the phenoxy radical bands from the phenolate bands will introduce error.

Finally, the largest spectral change occurs due to the disruptive formation of a LIBS plasma under the higher irradiation fluences. The plasma, an emission process, is 10-fold more intense than all but one of the phenolate Raman bands. Large fluctuations of the plasma intensity occur because of the statistical triggering of the plasma formation by the underlying photophysics. The probability that an electron avalanche occurs within the plasma is controlled by the formation of starter electrons. Although the exact formation mechanism for the starter electrons is still debated [110], exciting on a chromophore could lower the threshold for plasma formation.

The LIBS plasma emission is broad and complex making it difficult to determine the underlying phenolate resonance Raman spectra. The emission spectra contains at least three intense identifiable bands from sodium, hydrogen, and oxygen. The sodium originates
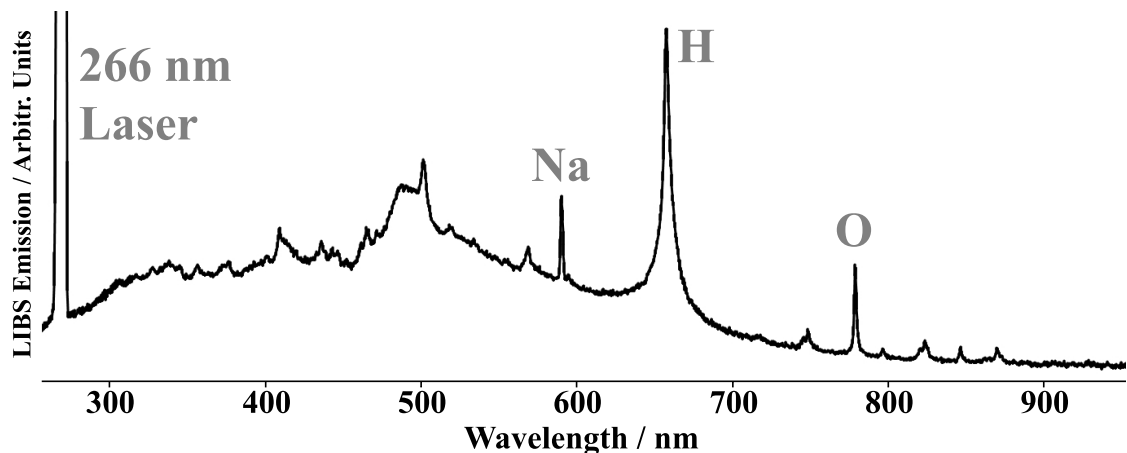
Figure 4: Emission of 5 mM pH 13 phenolate solution with 100 mW average power from pulsed 266 nm laser. A hydrogen line at 656 nm and an oxygen line at 777 nm are caused from the ionization of the water solution. A sodium line at 589 nm is caused by the sodium perchlorate internal standard and sodium hydroxide used to pH adjust.

from the sodium hydroxide, used to pH adjust the solution, and from the internal standard, sodium perchlorate. In the deep UV, various LIBS atomic emission bands overlap, causing continuum-like features to appear. In the 266 nm Raman spectral window of the phenolate solution, we observe a resulting broad band that is centered around 1400 cm^{-1} or 276 nm. The signal to noise of the phenolate Raman spectrum is poor since the standard deviation of the intensity from the fluctuating LIBS plasma is more intense than the standard deviation of the phenolate Raman intensities. Stray light reflections inside the spectrometer may also contribute to this high background, but have not been fully characterized.

Although the number of Raman scattered photons should scale linearly with the number of excitation photons, the duration of time the sample is exposed to that number of photons is critical. Pulsed laser power specifications are generally reported in peak power or average power. Peak power is the energy per pulse divided by the pulse width or the highest instantaneous power, whereas the average power is the total energy from the pulses integrated over one second. For example 1 mW of average power from a 100 Hz 3 ns pulsed laser like was used in these measurements has a peak power of 3.33 kW. This peak power is

more than 4 orders of magnitude more than that of the 100 mW CW laser. Therefore, the Raman spectra of phenolate shows non-linear phenomena even at the lowest pulsed energy used. Defocusing the laser on the sample can be used to reduce the irradiance, but will also decrease the overall Raman signal because the collected light will also be defocused. To maintain high signal to noise, a tightly focused, high average power, continuous wave laser is ideal.

2.6   Conclusion

One typically increases laser power to increase the signal to noise of Raman measurements. However, with high pulse energy excitation, multiple non-linear phenomena can occur that degrade the spectral measurement. We've demonstrated herein that the best way to maintain the Raman spectral integrity, is through the use of CW laser excitation.

2.7   Acknowledgments

2.8   Conflict of Interest

The authors declare no potential conflict of interests.

3.0 Diverse organic-mineral associations in Jezero crater, Mars

This chapter includes the full text from a manuscript of the same name published on July 12, 2023 by Nature. The article is published under a Creative Commons CC BY license, which permits unrestricted use, distribution, and reproduction in any medium. The author list is: Sunanda Sharma, Ryan D. Roppel, Ashley E. Murphy, Luther W. Beegle, Rohit Bhartia, Andrew Steele, Joseph Razzell Hollis, Sandra Siljeström, Francis M. McCubbin, Sanford A. Asher, William J. Abbey, Abigail C. Allwood, Eve L. Berger, Benjamin L. Bleefeld, Aaron S. Burton, Sergei V. Bykov, Emily L. Cardarelli, Pamela G. Conrad, Andrea Corpolongo, Andrew D. Czaja, Lauren P. DeFlores, Kenneth Edgett, Kenneth A. Farley, Teresa Fornaro, Allison C. Fox, Marc D. Fries, David Harker, Keyron Hickman-Lewis, Joshua Huggett, Samara Imbeah, Ryan S. Jakubek, Linda C. Kah, Carina Lee, Yang Liu, Angela Magee, Michelle Minitti, Kelsey R. Moore, Alyssa Pascuzzo, Carolina Rodriguez Sanchez-Vahamonde, Eva L. Scheller, Svetlana Shkolyar, Kathryn M. Stack, Kim Steadman, Michael Tuite, Kyle Uckert, Alyssa Werynski, Roger C. Wiens, Amy J. Williams, Katherine Winchell, Megan R. Kennedy & Anastasia Yanchilina. Ryan D. Roppel and Sunanda Sharma are co-first-authors and contributed equally.

3.1 Abstract

The presence and distribution of preserved organic matter on the surface of Mars can provide key information about the Martian carbon cycle and the potential of the planet to host life throughout its history. Several types of organic molecules have been previously detected in Martian meteorites [126] and at Gale crater, Mars [126, 93, 38]. Evaluating the diversity and detectability of organic matter elsewhere on Mars is important for understanding the extent and diversity of Martian surface processes and the potential availability of carbon sources [126, 123, 124]. Here we report the detection of Raman and fluorescence spectra consistent with several species of aromatic organic molecules in the Máaz and Séí-

tah formations within the Crater Floor sequences of Jezero crater, Mars. We report specific fluorescence-mineral associations consistent with many classes of organic molecules occurring in different spatial patterns within these compositionally distinct formations, potentially indicating different fates of carbon across environments. Our findings suggest there may be a diversity of aromatic molecules prevalent on the Martian surface, and these materials persist despite exposure to surface conditions. These potential organic molecules are largely found within minerals linked to aqueous processes, indicating that these processes may have had a key role in organic synthesis, transport or preservation.

3.2 Introduction

There are multiple origin hypotheses for the presence of organic matter on Mars from meteorite and mission studies. These include in situ formation through water–rock interactions[123] or electrochemical reduction of CO_2 [124], or deposition from exogenous sources such as interplanetary dust and meteoritic infall [126], although a biotic origin has not been excluded. Understanding the fine-scale spatial association between minerals, textures and organic compounds has been crucial in explaining the potential pools of organic carbon on Mars. The Scanning Habitable Environments with Raman and Luminescence for Organics and Chemicals (SHERLOC) instrument is a tool that enables this on the Martian surface.

The Perseverance rover was designed for in situ science with the ability to collect a suite of samples for eventual return to Earth [30]. The rover's landing site within Jezero crater combines a high potential for past habitability as the site of an ancient lake basin [88] with diverse minerals, including carbonates, clays and sulfates [111] that may preserve organic materials and potential biosignatures [26]. The Jezero crater floor includes three formations (fm) [122]; two of these, Máaz and Séítah, were explored as part of the mission's first campaign. Máaz, previously mapped as the crater floor fractured rough unit, is highly cratered and broadly mafic in composition; rover observations to date indicate a composition rich in pyroxene and plagioclase [127]. Séítah, previously mapped as the crater floor fractured 1 unit, is underlying and therefore presumed older than Máaz and contains rocks that rep-

resent an ultramafic olivine-bearing cumulate [80]. SHERLOC has observed three natural (as found) rock surfaces in Máaz and seven freshly abraded surfaces across Máaz and Séítah (Figure 5, Figure 13 and Figure 14). Abrasion consists of removing the outer layer of the rock, which is weathered and covered by Martian dust, using an abrading bit on the drill to create a 45 mm diameter cylindrical hole of 8–10 mm deep. The gaseous dust removal tool then removes residual fines with nitrogen gas [94] to reveal a flat, dust-free surface for analysis. Four abrasion targets are associated with rock cores that may be returned to Earth during the Mars Sample Return campaign.

The SHERLOC instrument is a deep ultraviolet (DUV) Raman and fluorescence spectrometer designed to map the distribution of organic molecules and minerals on rock surfaces at a resolution of 100μm [12]. This approach enables spectral separation of weak Raman scattering from stronger fluorescence emission, which can have cross-sections that are 105–108 times larger than Raman [12], allowing for measurement of both signals simultaneously. SHERLOC can detect Raman scattering from roughly 700 to 4,000 cm^{-1} and fluorescence photons from 253 to 355 nm (see Methods for more detailed descriptions). SHERLOC includes a autofocus context imager (ACI) coboresighted with the spectrometer to collect high spatial resolution (roughly 10.1μm per pixel) grayscale images to place spectral maps within the context of texture and grain sizes. The wide-angle topographic sensor for operations and engineering (WATSON) imager provides colour imaging and broader spatial context. Combined, these enable spatial associations between organics and minerals to assess formation, deposition and preservation mechanisms. SHERLOC has previously observed fluorescence signatures consistent with small aromatic compounds in three targets across the crater floor [113] that align with previous findings on Mars and within Martian meteorites.

3.3 Fluorescence signals in the crater floor

Fluorescence signals were detected on all ten targets observed by SHERLOC in the Jezero crater floor. They can be summarized by four main feature groups (Figure 6). Group 1 is a doublet at roughly 303 and 325 nm; group 2 is a single broad band at roughly 335-350
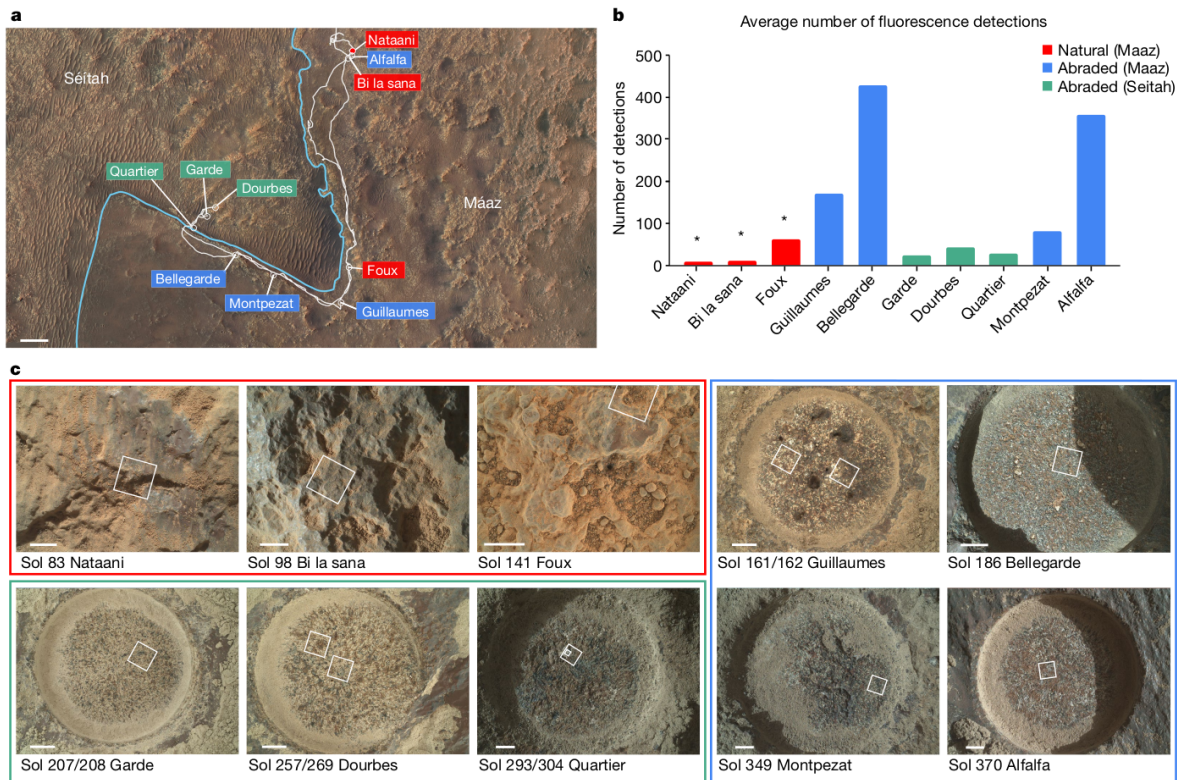
Figure 5: **a**, High Resolution Imaging ScienceExperiment (HiRISE) image of the region studied with the rover's traverse marked in white, the boundary between the Séítah and Máaz fm delineated by the light blue line, and each rock target labelled. Scale bar, 100 m. **b**, Average number of fluorescence detections (out of 1,296 points) from survey scans for each target interrogated by SHERLOC, arranged in order of observation. The acquisition conditions were different for dust-covered natural targets as compared to relatively dust-free abraded targets, possibly resulting in reduced detections. **c**, WATSON images of natural (red box) and abraded targets (Máaz is the blue box, Séítah is the green box) analysed in this study, with SHERLOC survey scan footprints outlined in white. Two survey scans were performed on Guillaumes, Dourbes and Quartier. Sol 141 imaging on Foux had an incomplete overlap of WATSON imaging and SHERLOC spectroscopy mapping. Scale bars, 5 mm.

nm; group 3 is a single broad band between roughly 270 and 295 nm and group 4 is a pair of bands centred at roughly 290 and 330 nm. The scan parameters are given in Figure 19. A two-sample Kolmogorov–Smirnov test was done on the observed fluorescence maxima for each group to determine whether they were statistically distinct from one another and found that groups 1–3 had null probabilities (likelihood that two groups are samples of the same distribution) of less than 10-40. Group 4 was too small for a statistical assessment, but is considered qualitatively different from the others.

The four fluorescence feature categories observed in the ten targets presented here are all consistent with emission in the spectral range shown by single ring aromatics and polycyclic aromatic hydrocarbons [12, 107] (Figure 20 and Figure 13). The number of rings in aromatic compounds can be estimated following the reported trend of emission spectra under DUV excitation [13], in which increasing emission wavelength is positively correlated with number of aromatic rings; this was used to define the four fluorescence feature categories used in this study (Figure 21). However, the potential for non-organic luminescence [43] must also be considered for each group and is discussed herein.

3.3.1 Group 1: doublet at roughly 303 and 325 nm

Two targets, Bellegarde and Quartier, showed the distinctive group 1 fluorescence feature (Figure 7). These peaks appear together with constant relative positions and intensities, probably indicating a single emitter. The Bellegarde target, located on the Rochette rock in the Máaz fm, yielded detections on white crystals that are probably hydrated Ca-sulfate based on SHERLOC and PIXL observations16; the fluorescence doublet feature was associated with these areas (Figure 7a,c). The Quartier target, located on the Issole rock in the Séítah fm, similarly contained white crystals that showed Raman peaks at 1,010–1,020 cm^{-1} and a broad band at roughly 3,500 cm^{-1} whose intensities were positively correlated (Figure 7b,d). Sometimes, minor peaks at roughly 1,140 and at 1,215–1,225 cm^{-1} were also present. These peaks are consistent with a mix of sulfates [105], potentially including both Ca- and Mg-sulfate at different hydration states. PIXL established that two different sulfate minerals were present, namely Mg-rich sulfate (66 wt% SO3, 27 wt% MgO, 3 wt% CaO, 4 wt%
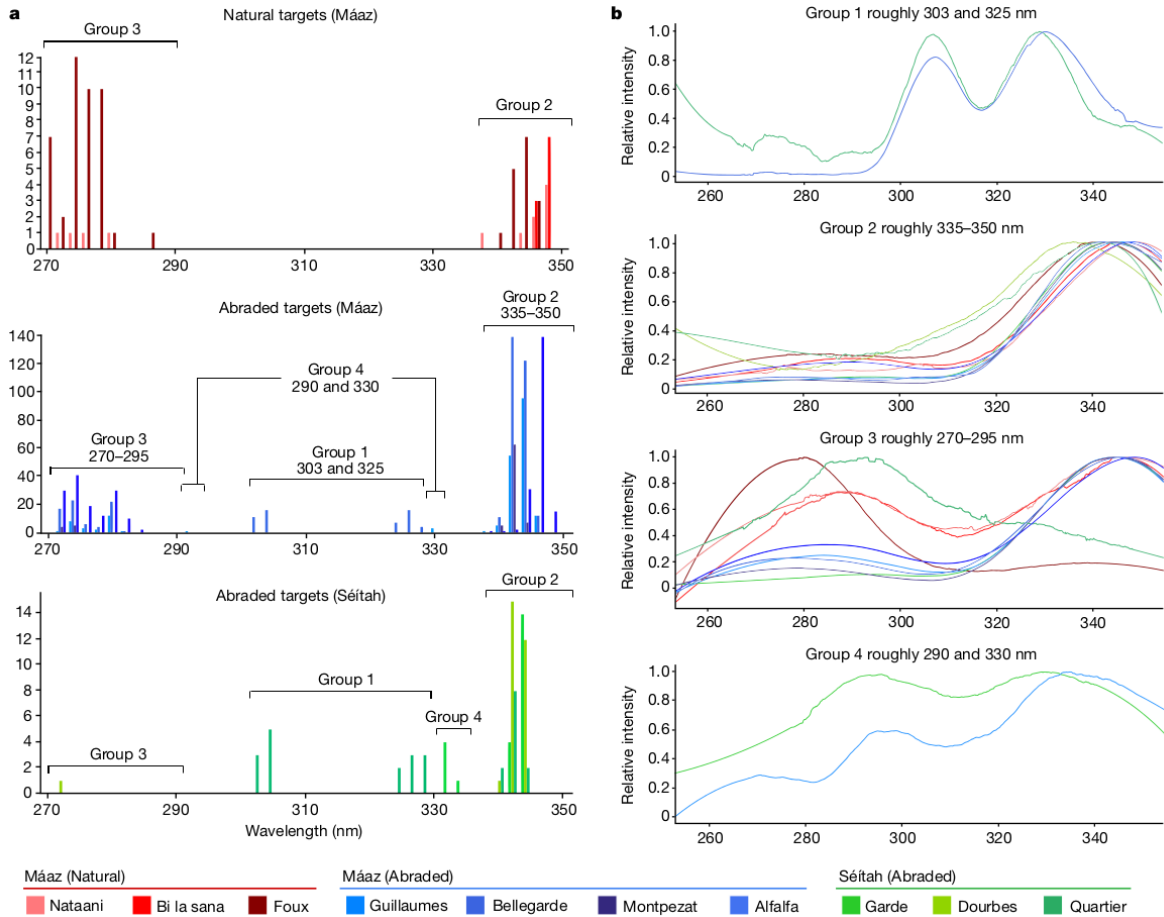
Figure 6: **a**, Histograms of the λ_{max} (measured from raw data) of four fluorescence features that were observed in survey scans in natural targets in Máaz (top, n = 84), abraded targets in Séítah (bottom, n = 82) and abraded targets in Máaz (middle, n = 1070). Bins of 1 nm show variation in band centres, y axes scaled to each dataset. **b**, Filtered mean spectra from each target representing each fluorescence feature category demonstrate characteristic band positions, normalized relative intensities and colocated features between targets. The range of the SHERLOC CCD is 250–354 nm. The rise in baseline below 270 nm is a boundary artefact introduced by the filter and not representative of the sample data. [114]
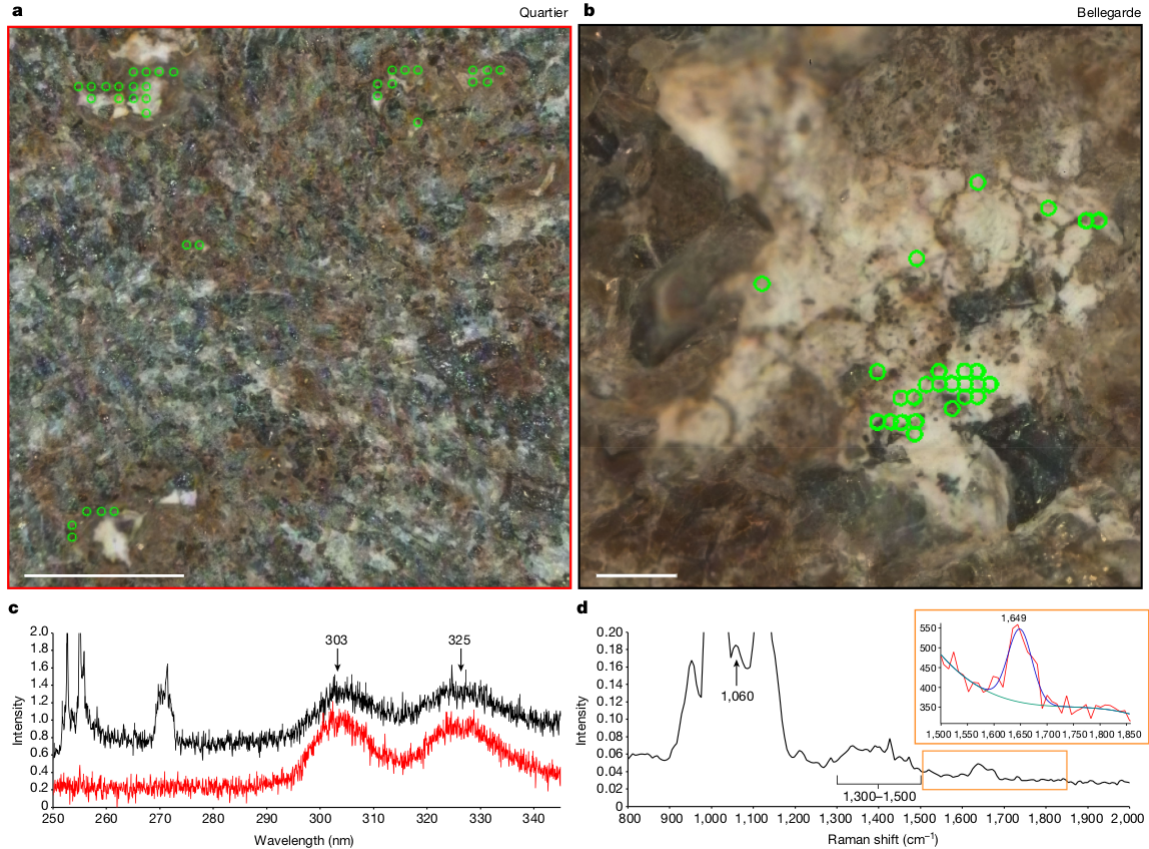
Figure 7: **a**, Colourized ACI image of a region where a survey scan (36 x 36 points over 5 x 5 mm^2) was performed on the Bellegarde target from sol 186. Green rings (rough laser beam diameter) represent locations where the roughly 303 and 325 nm fluorescence doublet was detected. **b**, Colourized ACI image of a region where a detailed scan (10 x 10 points over 1 x 1 mm^2) was performed on the Quartier target from sol 304. Green rings represent locations where the roughly 303 and 325 nm fluorescence doublet was detected. Scale bars, 1 mm. **c**, Median fluorescence spectra (unfiltered) from the green points indicated in Bellegarde (red, n = 33) and Quartier (black, n = 26) normalized to 303 nm band and offset for clarity. **d**, Median Raman spectra of four points with highest fluorescence band intensities from Quartier scans on sols 293 and 304. Roughly 1,010 cm^{-1} sulfate band is off scale; inset shows roughly 1,649 cm^{-1} band with Voigt fit (FWHM 53.737, area 12,559, height 192.79). In the inset, the unfitted spectrum (red), fitted spectrum (blue) and baseline (green) are shown; y axis is intensity.

FeO) and CaMg sulfate (61 wt% SO3, 18 wt% MgO, 19 wt% CaO, 2 wt% FeO). A Raman peak at roughly 1,649 cm^{-1} was detected at one point within the hydrated sulfate crystal where doublet fluorescence was also present. This peak was accompanied by a small peak at roughly 1,050 cm^{-1} and a broader feature that seemed to contain several peaks between 1,330 and 1,410 cm^{-1} (Figure 7d). Eleven sols later, several high-resolution scans subsequently performed on the same area of Quartier showed a nearly identical roughly 1,649 cm^{-1} peak at three points within hydrated sulfate crystals. In each case, the distinctive doublet fluorescence was detected as well as a broader feature at 1,330–1,410 cm^{-1}.

The group 1 fluorescence observations in Quartier (Séítah) are consistent with the presence of a one or two-ring aromatic organic molecule(s) within a hydrated sulfate crystal. It is also possible that the observed emission comes from Ce^{3+} concentrated within the sulfate, given the close match in emission wavelengths in laboratory data. Three Raman peaks at 1,060, 1,330–1,410 and roughly 1,649 cm^{-1} are colocated with the three most intense doublet fluorescence and strong hydrated sulfate signals. They were detected even after 11 sols of surface exposure, although the hydration feature (OH stretch at roughly 3,300–3,500 cm^{-1}) decreased in intensity, indicating a change in the hydration state after exposure to the Martian atmosphere. On the basis of the relative positions and intensities of these peaks, they represent at least two possibilities: vibrational modes of an organic molecule that include a preresonant C=C stretch [121], or asymmetric stretching and bending modes from nitrate within the sample [101]. The possibility of organics occurring within sulfates is supported by evidence from studies of Martian meteorites [123] and in Gale crater [121], which show that sulfates may have a key role in forming, preserving or transporting organic molecules in the Martian environment. The combination of Raman and fluorescence data reported here could constitute two lines of evidence that support the detection of organic molecules within hydrated sulfate crystals, which is the simplest explanation for these observations. If both Raman and fluorescence signals are inorganic in origin, nitrate and Ce^{3+} in sulfate would need to be colocated.

3.3.2 Group 2: single band at roughly 335 to 350 nm

The most common fluorescence feature detected was a single broad (roughly 30–40 nm full-width at half-maximum (FWHM)) band centred at roughly 335–350 nm. Group 2 fluorescence was observed on all targets across both formations and showed the highest intensities among the four fluorescence feature categories (Figure 6). The relative occurrence of this feature observed in survey scans of abraded targets was markedly higher in Máaz (189 ± 96 counts) versus Séítah (26 ± 6 counts). However, the average intensity of this feature was comparable between survey scans performed in the two formations (Máaz 342 ± 76 counts; Séítah 361 ± 80 counts). The measured intensity can vary on the basis of several factors, including the concentration of the emitter, the focus of the spectrometer and the presence of an absorbing material; therefore, large standard deviations are expected. Scans from all abraded targets show group 2 fluorescence detections that seem to be at or near grain boundaries in most cases (Figure 20 and Figure 13). In Máaz, the group 2 feature had an average band centre position of 344.1 ± 1.5 nm in survey scans and was observed to have band centres varying from roughly 338 to 349 nm, whereas in Séítah, the average band centre position was 343.1 ± 0.5 nm and the variance of the band centre had a narrower range, from roughly 340 to 345 nm (Figure 6a). In abraded targets in both formations, the group 2 feature was associated with a common set of minerals detected with Raman spectroscopy, including carbonate, phosphate, sulfate, silicate and occasionally, potential perchlorate (Figure 9 and Figure 16) [113, 105]. The key difference in mineral associations was that in three Máaz fm targets (Montpezat, Bellegarde and Alfalfa), this feature was also associated with possible detections of pyroxene. By contrast, in the Séítah fm, this feature was associated with a possible detection of olivine in at least one point on each target (Figure 20).

One point in the high dynamic range (HDR) scan on Montpezat showed a Raman peak at 1,597 cm^{-1} as well as weak fluorescence at roughly 340 nm (Figure 8a,b), and was colocated with a detection at roughly 1,080 cm^{-1}. The roughly 1,080 cm^{-1} signal shows a broad-shaped Raman band consistent with laboratory studies of carbonate and silicate minerals [43]. Raman spectroscopy cannot resolve silicate phases well because of the small degree of polarizability of the silicon-oxygen tetrahedron [47]; therefore, it is provisionally

assigned here as simply silicate or carbonate. The roughly 1,597 cm^{-1} peak closely matched the known graphitic (G) band observed on a sample from the Martian meteorite Sayh al Uhaymir (SaU008) calibration target in position and shape (Figure 8c,d and Figure 17). In the calibration target, the Raman peak at roughly 1,599 cm^{-1} is known to be from macro-molecular carbon[12, 39]; thus, the 1,597 cm^{-1} peak is consistent with a carbon–carbon bond. This point on SaU008 similarly shows weak group 2 fluorescence at roughly 340 nm, although it seems to have lower intensity and longer emission wavelength than the point on Montpezat. Higher confidence in a specific Raman assignment would have been possible if the peak was detected at a greater signal-to-noise and seen at more than one point. Several nearby points showed possible peaks below the detection threshold.

The mean spectrum of points where the highest intensity group 2 features were detected on Garde (Séítah fm) yielded a Raman peak at roughly 1,403 cm^{-1} (Figure 8e,f). These points were correlated to Raman detections consistent with olivine (823 cm^{-1}), phosphate (960 cm^{-1}) and carbonate (1,086 cm^{-1}). Another possible peak in the mean spectrum was visible at roughly 1,540 cm^{-1}, but was at the lower limit of detectable width (less than 3 pixels FWHM) so is unassigned. The roughly 1,403 cm^{-1} peak could be due to an organic compound, such as a C=O stretching vibration of an organic salt [40]. Organic salts are possible oxidation and radiolysis products of organic matter and have been indirectly detected on Mars previously [78]. Carbonyl groups and aromatic or olefinic carbon have been correlated with carbonate in a Martian meteorite [123]. Further work is continuing to rule out secondary modes of matrix minerals.

The group 2 fluorescence (roughly 335–350 nm) feature is consistent with a two-ring aro-matic molecule, such as naphthalene. Alternatively, the emission spectra are also consistent with Ce^{3+} in phosphates, on the basis of laboratory data [113]. Both aromatic organics6 and Ce^{3+} have been associated with phosphate minerals in Martian meteorites [118, 133]. With the data collected from Perseverance and our laboratory analyses, we cannot rule out a contribution from both inorganic and organic sources. The aromatic compounds would probably exist with some degree of chemical substitution or in specific steric configurations with respect to surrounding minerals, that would result in blue- or red-shifting from the ex-pected fluorescence wavelengths for benzene and naphthalene. Red-shifting of fluorescence
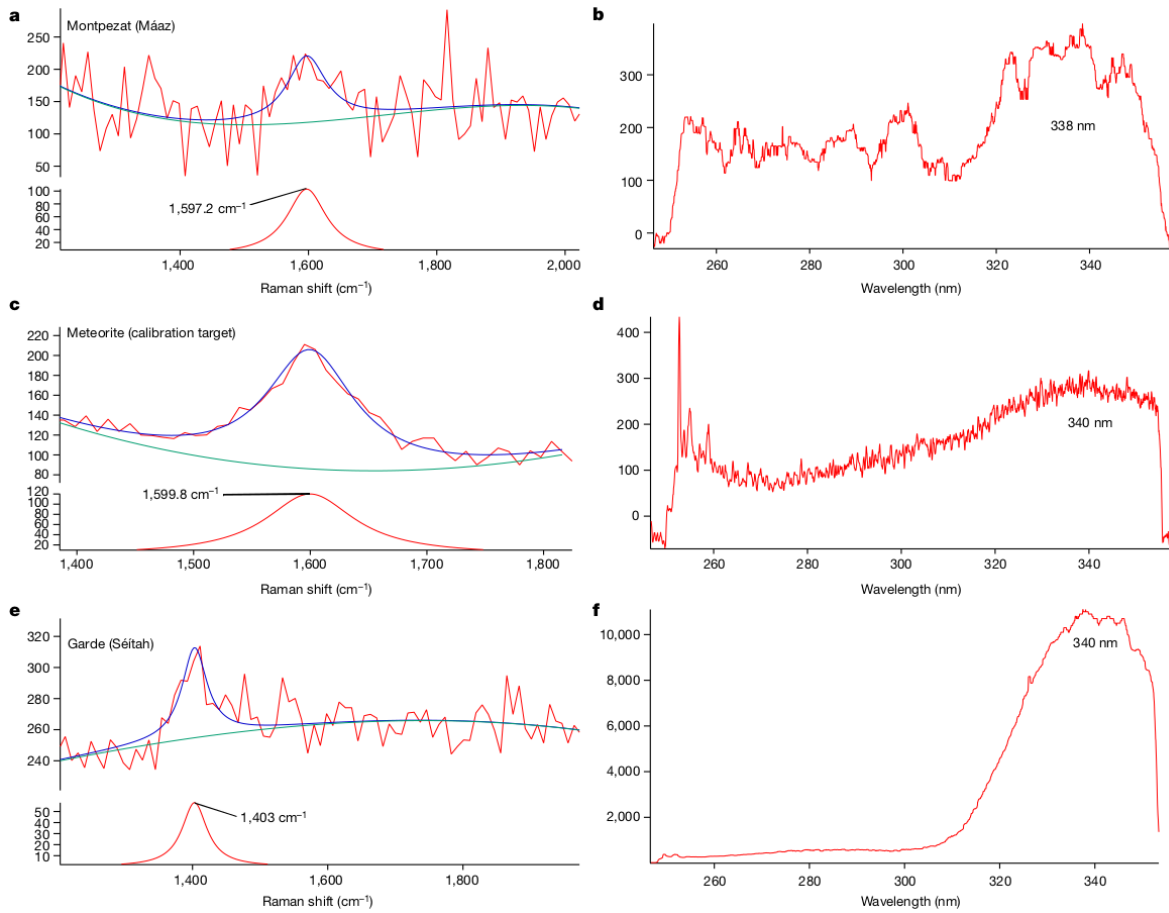
Figure 8: **a**, Raman spectrum from point 40 of an HDR scan on Montpezat (sol 349) with a Lorentzian fit (FWHM 49.873, area 8,069.1, height 103). **b**, Corresponding average fluorescence spectrum to a (lambda max roughly 338 nm). **c**, Median Raman spectrum (n = 100) from an HDR scan on the SaU008 meteorite calibration target (sol 181), which contains the known graphitic (G) band, with a Lorentzian fit (FWHM 61.784, area 11,646, height 120). **d**, Corresponding average fluorescence spectrum to c (lambda max roughly 338 nm). **e**, Average Raman spectrum of points with the highest group 2 fluorescence (n = 28) on Garde (sol 207–208) with a Lorentzian fit (FWHM 47, area 4,500, height 60.953). **f**, Corresponding average fluorescence spectrum to c (lambda max roughly 340 nm). In all graphs, the unfitted spectrum (red), fitted spectrum (blue) and baseline (green) are shown; the y axis is intensity.

30

due to the formation of carboxylic acids on or near the aromatic ring is highly probable as these compounds are exposed to high energy radiation in an oxidative environment [11, 138], and previous studies of refractory organic carbon in Martian meteorites have shown carboxyl functionality [123, 124]. It is highly probable that the detected fluorescence features, if organic, represent mixes of organic moieties rather than single emitters, and their overlapping spectra could cause variability in the apparent position and the FWHM of observed bands. This would align with the colocated detections of many fluorescence features on the same points. If the fluorescence is inorganic, the emissions could also be varied as Ce^{3+} luminescence is highly matrix dependent and affected by changes in mineralogy and mineral composition [43].

3.3.3 Group 3: single band at roughly 270 to 295 nm

Fluorescence bands between roughly 270 and 295 nm (FWHM of roughly 20 nm) were observed at many points in survey scans of three abraded (Guillaumes, Bellegarde, Alfalfa) and one natural target (Foux) in Máaz, and at few or no points in all other scans (Figure 13 and Figure 14). On the targets with a substantial number of detections, points where group 3 fluorescence was detected often appeared clustered together on brown-toned, possibly iron-stained material (Figure 14 and Figure 17). In many cases, this feature was colocated with the group 2 feature and was comparatively weaker in intensity (Figure 6, and Figure 16). The average band centre position in natural targets (276.1 ± 0.8 nm) and abraded targets (276.1 ± 1.4 nm) in Máaz were similar. Given the few overall detections in Séítah, no quantitative comparison was possible. No clear mineral associations were detected with group 3 fluorescence in Máaz abraded targets, except Alfalfa. Here, fluorescence was associated with a broad Raman peak at roughly 1,040–1,080 cm^{-1}, assigned to possible silicate [27, 43], and peaks at roughly 1,085–1,100 cm^{-1}, assigned to carbonate [27, 43], at or near boundaries of black and grey grains. As with the group 2 feature, no clear textural associations were observed in natural targets, and no mineral signatures could be identified in the spectra. The group 3 (roughly 270–295 nm) feature is consistent with a single ring aromatic compound, such as benzene16; possible non-organic sources, such as silica defects, are discussed in the

Methods.

3.3.4 Group 4: roughly 290 and 330 nm features

The feature with bands centred at roughly 290 and 330 nm was observed on two targets, Guillaumes (Máaz) and Garde (Séítah). In both, it was observed on several points in intergranular spaces; this was particularly apparent on Garde as previously reported [113]. On Guillaumes, group 4 fluorescence was not clearly associated with specific minerals. On Garde, it was colocated with Raman peaks at roughly $1{,}087$–$1{,}096$ cm^{-1} and a broad peak at roughly $1{,}080$ cm^{-1}, assigned to carbonate and silicate, respectively [27, 43] (Figure 18). The relative intensities of the two peaks were not constant between points, indicating that they could be from several emitters. It is also possible that it is not a distinct category but simply a combination of group 2 and 3 species. The spectra are consistent with a one or two-ringed aromatic compound(s), though the possible inorganic sources of groups 2 and 3 may also apply to group 4.

3.4 Relative abundance of organic compounds

The observed fluorescence response, if solely from organic molecules, can be used to provide a conservative estimate of concentration using a single ring aromatic (benzene) with a weak fluorescence cross-section and an assumed depth of penetration of 75 μm [113, 18]. This depth is a conservative estimate based on DUV transmission of more than 150μm through Mars simulants [18]. Comparing the survey scans of the abraded surfaces, the localized concentrations are varied and range from 20 to 400 pg of organics where Alfalfa (Máaz) has some of the highest number of occurrences and localized concentrations. Furthermore, the bulk concentration in Máaz is an order of magnitude higher than in Séítah (roughly 20 versus 2 ppm).

3.5 Diverse fluorescence across formations

The Máaz and Séítah fm are two geologically and compositionally distinct formations that also show two different patterns of fluorescence. Following the hypothesis of the fluorescence being entirely organic in origin, these findings would indicate different bulk quantities of organic material, with Máaz having an order of magnitude more than Séítah. While colocations between organic features and minerals associated with aqueous processes were found in both formations, the colocation with primary igneous minerals was different. The group 2 feature was associated with olivine at many points in all Séítah targets and to pyroxene in two Máaz targets (Figure 9). This suggests several mechanisms of synthesis or preservation, which may be at least partially unique to each formation. A similar pattern of organics associated with pyroxene and olivine has been shown in studies on meteorites ALH84001, Nakhla and Tissint. In these cases, the organic material has been shown to be synthesized in situ [123]. Further observation of the cored samples is needed to confirm the provenance and formation mechanism of this material.

Previous findings indicate that the two formations underwent different alteration processes. Máaz seems to be aqueously altered basaltic rock that contains Fe^{3+} bearing alteration minerals [29]. Séítah is proposed to be an olivine cumulate [80] altered by fluids at low water to rock ratios [18], and contains mafic minerals that have higher abundances of total FeO than Máaz rocks [129]. Owing to the presence in Máaz of Fe^{3+} bearing minerals, which can attenuate the fluorescence response [23], we would expect fewer and lower intensity fluorescence detections than in Séítah. However, our observations demonstrate the opposite, with Máaz targets having more fluorescence detections and highest localized fluorescence intensities. If the fluorescence is organic, this demonstrates a correlation of organics occurrence and abundance with the degree of water-driven alteration and suggests that these signatures are driven by synthesis and/or transport mechanisms rather than meteoritic deposition, which would probably affect both formations in a similar manner. The concentrations of organics associated with more aqueously altered surfaces are consistent with known bulk concentrations of organics observed in Martian meteorites at roughly 11 ppm [126] and in situ analysis performed by Curiosity rover in Gale crater that indicated
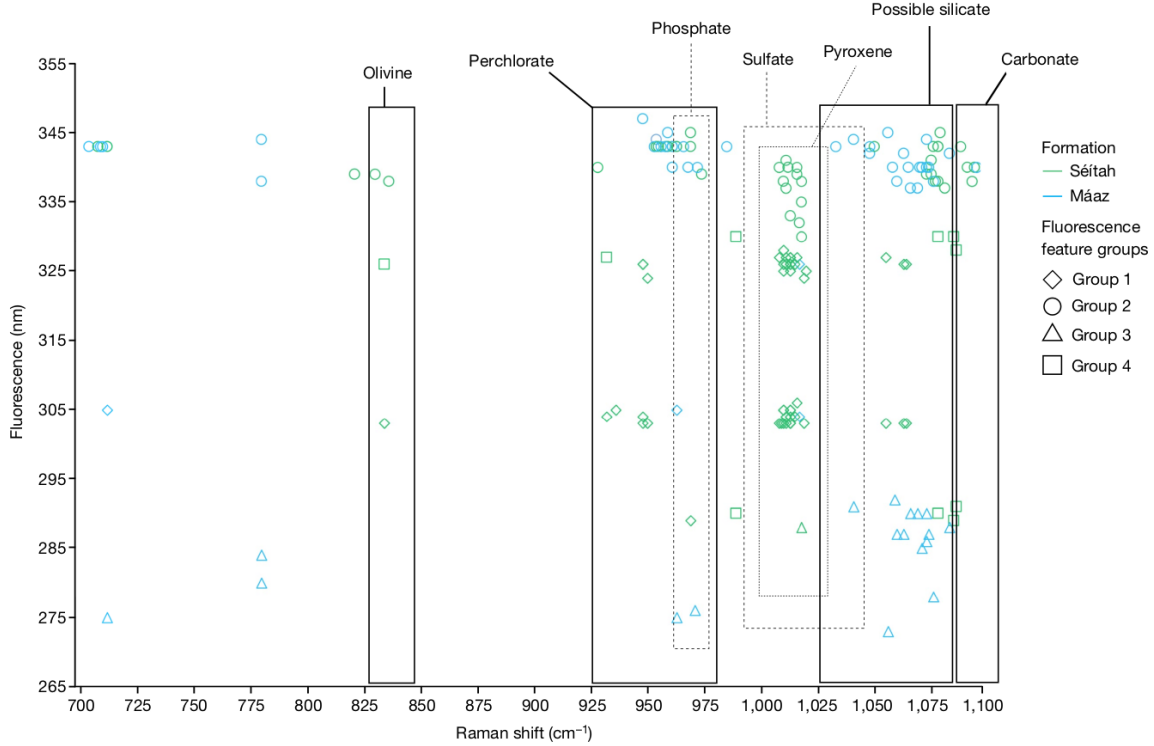
Figure 9: Select mineral detections (Raman shift, cm^{-1}) and their fluorescence features (λ_{max}, nm) for abraded targets analysed using unsmoothed data from HDR and detail scans; both Raman and fluorescence data are measured on the same point. Máaz scans (blue) used between 250 and 500 ppp, yielding low signal-to-noise ratio (less than 2) in some cases that were not included; Séítah scans (green) all used 500 ppp, allowing for comparatively more Raman detections. Mineral classifications based on high confidence Raman detections of major peaks are indicated by boxed regions: olivine (roughly 825-847 cm^{-1}) [27, 43, 78] range of hydrated and dehydrated perchlorate (roughly 925-980 cm^{-1}) [78, 73], phosphate (roughly 961-975 cm^{-1}) [43] [78, 73], pyroxene (roughly 1,000–1,026 cm^{-1}) [43], sulfate (roughly 990-1,041 cm^{-1}) [27, 43, 78], amorphous silicate (broad peak at roughly 1,020-1,080 cm^{-1}) [27, 78] and carbonate (roughly 1,085-1,102 cm^{-1}) [43, 73]. Markers outside a boxed region do not have a mineral assignment. Disambiguation of overlapping regions can generally be resolved by consideration of minor Raman peaks (not marked here) and corroboration by other instrument(s) (for example, PIXL/SuperCam) [106].

organics concentrations from roughly 7 ppb to 11 ppm [27].

The two formations also showed different types of fluorescence features. Whereas the group 1, 2 and 4 features were detected in both formations, Séítah showed a near-complete absence of group 3 features. This could indicate selective synthesis or preservation mechanisms that favour the organics associated with the longer wavelength fluorescence or a degradation process that only affected the group 3 associated organic molecules. The group 2 feature was most frequently detected in both formations, but showed differences in the abraded targets in Máaz and Séítah. Although the average band centre positions of the group 2 detections in both units were similar (Máaz 344.1±1.5 nm; Séítah 343.1±0.5 nm), the range of band centres in abraded Séítah targets was narrower (roughly 340–345 nm), whereas the band centres in abraded Máaz targets were more broadly distributed (roughly 338–349 nm).

3.6   Potential mechanisms affecting organic matter

The four fluorescence features observed on the ten targets interrogated by SHERLOC each show varying degrees of mineral association and spatial patterning, suggesting that these features may originate from more than one mechanism of formation, deposition or preservation. Two of the features, groups 1 and 4, were highly localized to specific minerals, whereas the other two features were associated with several minerals and more broadly distributed. Continuing the organic hypothesis, the clearest association between a specific organic detection, mineral detection and texture was the group 1 feature found on Bellegarde and Quartier associated with white sulfate grains (Figure 7). One possible mechanism consistent with this association is abiotic aqueous organic synthesis. Aromatic molecules, including sulfur-containing species, associated with sulfate have been found in Tissint, Nakhla and NWA 1950 [123] and were proposed in these cases to be the result of electrochemical reduction of aqueous CO_2 to organic molecules due to interactions of spinel-group materials, sulfides and a brine. Organics in ALH84001 have been shown to be produced during carbonation and serpentinization reactions, indicating that several abiotic organic synthesis

mechanisms can occur on Mars. Alternatively, this organic-mineral association could be the result of mineral-mediated selective preservation of transported organic compounds in sulfate. Previous work has shown that sulfates, including gypsum and magnesium sulfate, can protect organic molecules within their crystal lattices from UV radiation and oxidation [35] and terrestrial evaporitic sulfate minerals can preserve organic material over geological timescales [37, 115].

The group 2 feature was the most frequently detected across all target types and formations, suggesting that a common synthesis, deposition, preservation or alteration process was responsible. Previous literature has implied that primary organic carbon is potentially ubiquitous in Martian basaltic rocks and there may be an abiotic reservoir of organic carbon on the planet [125]. Although most of the mineral associations of the group 2 feature were common across both formations, the association with pyroxene in Máaz targets and olivine in Séítah targets suggests that potentially distinct mineral-mediated processes influenced these organics (Figure 9). These could include formation of an aromatic radiolysis product by means of a mineral-mediated alteration reaction [11, 138, 36, 24]. The paucity of fluorescence detections and near absence of group 3 detections in Séítah suggest that there was different synthesis or deposition in this formation or the organic compounds were more thoroughly degraded. The relative ages of the two units are such that increased degradation in Séítah would have to be due to another phenomenon, such as accelerated erosion processes or potential brief exposure to a more acidic fluid than in Máaz that could affect organic matter.

In natural targets, fluorescence detections do not seem to correlate with morphological features or textures, which is consistent with the aromatic emitters present within the ubiquitous Martian dust. Meteoritic infall and interplanetary dust particles transport organic molecules to the surface of Mars, which are subsequently oxidized [34, 22]. The presence of dust would also explain the fewer detectable signals on natural targets, as it may absorb or scatter incident light.

3.7 Conclusions

Samples analysed in two formations within Jezero crater yielded detections by both fluorescence and Raman spectroscopy consistent with organic material that is colocated with specific mineral assemblages. The general spatial correlation between these detections and minerals that have undergone substantial aqueous processing suggests that organic molecules may have been abiotically aqueously deposited or synthesized within these altered volcanic materials within the crater floor. Differences in the nature and distribution of organic molecules in the formations would indicate that different aqueous alteration or deposition processes occurred, possibly contributing to the diversity of organic matter still present. The confirmation of organic origin and specific identification of these molecules will require samples to be returned to Earth for laboratory analysis. However, these results indicate a more complex organic geochemical cycle may have existed than has been described from previous in situ measurements on Mars, as evidenced by several distinct pools of possible organics. In summary, key building blocks for life may have been present over an extended period of time (from at least roughly 2.3–2.6 Ga, [51]), along with other as yet undetected chemical species that could be preserved within these two potentially habitable paleo-depositional settings in Jezero crater.

3.8 Methods

3.8.1 Further observations for group 2 fluorescence features

The overlap between the Raman signals from dehydrated perchlorates and phosphates coupled with low signal-to-noise made distinguishing between these assignments challenging in some cases. The key difference in mineral associations was that in three Máaz fm targets (Montpezat, Bellegarde and Alfalfa), the group 2 fluorescence feature was also associated with possible detections of pyroxene. By contrast, in the Séítah fm, this feature was associated with a possible detection of olivine in at least one point on each target (Figure

37

20).

Group 2 fluorescence bands in the natural targets (Máaz fm.) showed a similar shape to those in abraded targets, but the average band position in survey scans was 346.1 ± 2.0 nm, although it may be higher and obscured as it overlaps with the edge of the SHERLOC spectral range. This feature was not correlated to any specific texture. No identifiable Raman bands were detected on these targets, probably due to lower pulses per point (ppp) in the performed scans as well as signal attenuation due to out-of-focus regions and a dust layer; this precluded mineral identification. Signal attenuation aligns with the lower average intensity observed with the group 2 feature on natural targets (188 ± 42 counts) in comparison to dust-free abraded targets.

3.8.2   Potential non-organic luminescence

Luminescence can be caused by non-organic sources as well as organic; however, excitation in the deep UV (less than 250 nm) has the advantage of being in the wavelength range to resonantly excite one- and two-ring aromatics and to avoid most of the interfering luminescence responses from rare earth ions. Nevertheless, the features of the presented dataset (including mineral associations, spatial distribution, frequency of detection, maximum lambda value (lambda max) of the emission bands, and context from previous Mars missions and Martian meteorites) should be compared in the context of each proposed source.

Fluorescence in inorganic minerals, such as feldspars [73], can be due to emitters such as rare earth elements (REEs), or lanthanides and other metals within a mineral matrix that can act as activators [43]. REEs, in most cases, have emissions at wavelengths higher than the SHERLOC spectral range (that is, more than 360 nm) [108, 43]. The most relevant REE to the reported detections is cerium, which can generate emissions within certain minerals in the detection range of SHERLOC. Under 266 nm excitation, Ce^{3+} in phosphates has been reported to emit roughly 340 nm luminescence [119] that resembles some group 2 detections. In the dataset presented here, group 2 fluorescence is not always associated with a Raman identification of a phosphate mineral phase. However, Raman scattering of phosphates is not resonantly enhanced with the SHERLOC DUV laser, so the lack of a Raman detection

colocated with 340 nm fluorescence does not preclude Ce^{3+} in phosphates as the source of the roughly 340 nm emission. The emission spectra of Ce^{3+} is highly matrix dependent and changes in mineralogy and mineral composition can notably affect the emission profile [43]. As shown in Figure 9, the observed fluorescence is associated with a variety of minerals from aqueous processes that include sulfates, phosphates and carbonates, and is similar in position and shape regardless of association. Simple aromatic organic molecules can be preserved in these phases, and therefore are also potential sources for the reported fluorescence. However, it is possible that both organic and inorganic sources, or inorganic sources alone, contribute to the group 2 signals, as REE-bearing phosphates and organics preserved in phosphates have both been reported within Martian meteorites [81, 2].

In a laboratory study of synthetic ceric sulfate decomposition, strong photoluminescence emissions were reported [6]. In this study, both laboratory-synthesized and commercial ceric sulfate were heated to 500 °C for 16 h, then observed with a spectrofluorimeter. Ce^{3+} in both pentahydrated sulfates and anhydrous sulfate yielded double peaked emissions, at 319/339 and 322/339 nm, respectively. This latter observation aligns with other photoluminescence studies [42]. The closest emissions of cerium within sulfate reported in literature (at 304/327 nm), to the authors' knowledge, is in a study of synthetic heat-treated anhydrite doped with Ce^{3+} and observed with cathodoluminescence [9]. There is an unexplained 12–13 nm difference in emissions of synthetic Ce-doped anhydrite and Ce^{3+} in natural anhydrite from many locations also measured in this study, indicating that the synthetic sample may not be the most accurate comparison to our dataset. As such, further laboratory analyses on both natural and synthetic cerium-containing sulfate samples are continuing. The lambda max of luminescence emission of cerium in sulfates is expected to shift on the basis of the hydration state of the mineral [6]. SHERLOC observed sulfates in different states of hydration, for instance on the several observations of the Quartier target, yet the observed fluorescence remained consistent in lambda max. Given the reported emissions of several organic molecules under DUV excitation (Figure 15) in this range, it seems likely that one or more of these molecules may be present in the sulfate minerals. The presence of organics could also possibly explain the Raman detections between roughly 1,300 and 1,650 cm^{-1}. Finally, in the dataset presented here, group 1 was associated with sulfates in all cases;

however, many points across targets showed clear Raman peaks of sulfates without the colocated fluorescence signal. This heterogeneity also aligns with the expected patterns of organics distribution. Further examination of the Quartier scans through more detailed analysis and laboratory comparisons is currently underway.

A subset of the signals in group 3 (roughly 281 nm) are also consistent with luminescence associated with defects in irradiated silica caused by oxygen deficiency centres [139]. However, we do not anticipate that the SHERLOC laser would create such defects, given the high power required to do so. Furthermore, we do not see a clear increase in detections at roughly 281 nm in higher ppp scans in comparison to low ppp, which would be expected if SHERLOC's laser was inducing such damage. Investigation of other mechanisms (for example, radiation) that would cause localized silica defects that could produce luminescence consistent with group 3 features is continuing.

3.8.3 Future possibilities for Mars sample return

The potential detection of organic molecules by SHERLOC in the abraded targets marked the corresponding cores as high priority for sampling during the crater floor campaign. If these samples are returned to terrestrial laboratories, a more diverse suite of tools can be used to study the samples, including at higher spatial resolution and with much greater specificity and sensitivity. The organic material and mineral relationships can be interpreted within the context of their original locations and stratigraphy, unveiling new insights into organic geochemical cycling on Mars.

3.8.4 SHERLOC spectroscopy general operations

The use of a DUV wavelength may enable more sensitivity to aromatic organic molecules in complex matrices. At 248.6 nm wavelength excitation, a 10 to 1,000-fold increase in Raman scattering is provided by resonance and preresonance with aromatic organic molecules that have a large absorption cross-section. Measured Raman intensities are governed by both their Raman cross-sections and also the number of molecules excited. Transparent minerals with high scattering cross-sections can lead to large intensities whereas relatively

few organic molecules in resonance with the SHERLOC laser can lead to similar intensities. Measured fluorescence intensities of mixtures are affected by their quantum yields but also self-absorption. Förster energy transfer can result in the measured intensity of only a single fluorophore even though a mixture of several species exists. Analysis of both fluorescence and Raman data can yield unique insight into mixtures of minerals and organics.

SHERLOC spectroscopy measurements are colocated with 1,648 x 1,200-pixel ACI autofocus full-frame images and placed on the desired target at a 48 mm standoff distance. Activities are constrained by the time of day the laser is operating, optimizing the temperature of the spectrometer CCD to be below -20 °C and reducing contributions from ambient light. Of the 14 instances SHERLOC spectroscopy has run on the surface of Mars to date, there was only one activity that occurred slightly outside this optimal temperature range (the first abraded target, Guillaumes run on sol 161). This temperature constraint to generate valuable science data for SHERLOC means that it is optimal for SHERLOC spectroscopy to be run in the evening, after 20:00 (or early in the morning, but evening is preferred). SHERLOC spectroscopy was conducted on natural samples at midday and abraded samples in the evening, after local sunset, with the abovementioned exception of Guillaumes on sol 161. The robotic arm is capable of placing SHERLOC within 12 mm of a targeted location; SHERLOC's internal scanning mirror has a positioning error of less than 22 μm at the target. The spectrometer has an estimated uncertainty of ±5 cm^{-1} (±0.004 nm) in the 700–1,800 cm^{-1} region, on the basis of the calibration performed on sols 59 and 181. SHERLOC spectroscopy on natural and abraded targets has evolved since the initial natural surface measurement on sol 83. In general, there are two standard suite measurements, with slight modifications where necessary, for SHERLOC spectroscopy and ACI imaging scans: (1) HDR and survey scans, ACI four-image mosaic, ACI 31-image z-stack and (2) detailed scans, which are usually coupled with a survey scan run before the detail scans, for context. In this study, spatial correlations, histograms and average number of detections of fluorescence were conducted using survey scans; mineral-textural-organic correlations were performed using HDR and detailed scans. In the cases of two sols of observation on the same target, the following sols observations were used: Guillaumes 161, Quartier 293 and 304 and Dourbes 257 and 269. Two survey scans were performed on Guillaumes, Dourbes

and Quartier. Sol 141 imaging on Foux had an incomplete overlap of WATSON imaging and SHERLOC spectroscopy mapping.

3.8.5   SHERLOC spectroscopy sequences

3.8.5.1   Natural targets

HDR scans consisted of three sets of 100 spectra, coarse-spaced (780 μm step size), 7 x 7 mm^2 scan area, at high ppp (100 ppp for the first two scans, 300 ppp for the final scan). The first natural sample, Nataani, uplinked on sol 83, had 5, 50 and 100 ppp. The survey scan consisted of one scan of 1,296 spectra, 144 μm step size, 5 x 5 mm^2 scan area at low ppp; typically, 15 ppp, but 10 ppp and a step size of 200 μm was used for Nataani.

3.8.6   Abraded targets

The first abraded target, Guillaumes, followed the typical HDR scan sequencing, and consisted of three sets of 100 spectra; coarse-spaced (780 μm step size); 7 x 7 mm^2 scan area; 100, 100 and 300 ppp followed by a survey scan of 1,296 spectra; 144 μm step size; 5 x 5 mm^2 scan area and 15 ppp. In the targets analysed after Guillaumes, HDR scans were changed to two maps of 250 ppp (that is, 250/250) but conserved the total number of laser pulses (500), producing two 50 spectra maps for a total of 100 spectra when combined. The abraded samples also universally used a high laser current (25 A compared to the previous natural surface targets, which were shot at 20 A). When analysing the target, Garde, we had an option to use detailed mode scans for the first time. The initial scan on Garde on sol 207 used the standard suite HDR and survey scans. On sol 208, we did two sets of 50 spectra, 100 μm step size, 1 x 1 mm^2 scan area and 500 ppp detailed scans. Although the survey scan was not included in sol 208, it became standard to include for subsequent detail scans (for example, Dourbes on sol 269 and Quartier on sol 304). The scan start position for all HDR and survey scan is at the centre, whereas for the detail scans the scanner starts in the corner or offset position.

3.8.7   SHERLOC imaging operations

The two imaging systems, WATSON and ACI, are mounted atop a rotatable turret on the rover arm and are used during each SHERLOC observation. They are not coboresighted but the resulting images can be registered and overlaid to provide colour and textural information for a single target. WATSON acquires 1,600 x 1,200-pixel colour images of targets of interest from 2.5–40 cm standoff distances to provide broader context within the rock and outcrop. ACI images are always taken before spectroscopy and begin with two 256 x 256-pixel autofocus subframe and full-frame images. Further contextual imaging to support SHERLOC spectroscopy and correlation to images taken by other instruments, spectroscopy operations typically include a four-image ACI mosaic and a 31-image z-stack. The timing and lighting conditions of these products have been adjusted accordingly over the course of the ten targets (and 14 individual sample measurements) that SHERLOC has investigated. Typical operations for LED lighting are to take ACI images with all white LEDs turned on. Dourbes (sol 257) was the first time we had experimented with different lighting conditions on a target. For subsequent standard suite measurements, this update to the LED configuration (different group LEDs on and the use of UV LEDs) became a standard part of the sequences. The scanner is in the home position for the acquisition of the z-stack, which provides surface topographic relief when the in-focus images are assessed on the ground. The scanner is in the mosaic position for acquisition of the mosaic.

3.8.8   Abrasion operations

Each selected target studied after sol 141 was abraded using the rover's abrasion tool before SHERLOC observation. This tool grinds away the upper layer of rock, cuttings of which are then removed using the gaseous dust removal tool to reveal a fresh surface for analysis [94]. The resulting abrasion patch is a 45 mm diameter circle with a depth of 8–10 mm.

3.8.9 Spectral data processing

Unsmoothed data without outlier removal were used to determine intensities and band positions. Preliminary spectral data processing was performed using an open-source software package named Loupe developed at the NASA Jet Propulsion Laboratory by K. Uckert. This software enables dark frame subtraction, laser normalization and selection of regions of interest (ROI), as well as the correlation of individual spectra to locations on the ACI image on the basis of the scanning mirror positioning. Exported Loupe data were then further processed using custom Python scripts, Microsoft Excel and Spectragryph [92]. These were used to perform baseline subtraction, outlier removal, peak detection and median smoothing in a semi-automated manner (the last only for fluorescence data in Figure 8 and Figure 15). Outliers, generally caused by cosmic rays or charge buildup on the detector, were removed through subtraction and then the remaining data were interpolated across the spectrum. Requirements for fluorescence peak detection included FWHM of at least 100 pixels and more than five times the neighbouring background signal estimated by measurement in Loupe. A 10/1 signal-to-noise ratio was required for quantification, which may have excluded a small number points with actual signal but was deemed a robust criterion for accurate measurement of lambda max and FWHM. Fluorescence spectra used in Figures 6, 7, 8, Figure 20, 18 and Figure 17 were smoothed using the Savitzky–Golay algorithm with parameters manually tweaked after comparison to non-processed spectra. This was performed using the SciPy Python package [131]. This algorithm is known to introduce boundary artefacts [114], which can be seen less than 270 nm in several spectra that are not representative of the true data. Fluorescence data were also fitted in Igor64 (Wavemetrics) to allow for measurement of lambda max and FWHM. Bands were fitted using Gaussian or exponentially modified Gaussian functions; baselines were fitted using constant, linear or cubic functions on the basis of visual analysis and chi-squared goodness-of-fit values. For cases in which the fluorescence band was cut off by the edge detector, such as in group 2, the band was always assumed to be symmetric beyond the cut off. For Figure 9, lambda max and FWHM of each fluorescence spectrum was measured before association to a Raman signal (and possible mineral association) was considered, to maintain objectivity and avoid bias. Requirements

for Raman peak detection included FWHM of at least 4 pixels and more than twice the neighbouring (10 pixels) background signal intensity estimated by measurement in Loupe. This width threshold was selected on the basis of the spectral resolution of the instrument (roughly 3–4 pixels) [130]. FWHM of Raman spectra in Figure 8 were baselined using the airPLS algorithm [141] implemented in Python. Unsmoothed Raman data were fitted using the Multipeak Fit package in Igor64 (Wavemetrics), which enabled peak identification and fitting as well as baseline fitting and chi-squared value approximation. The signal-to-noise ratio for SHERLOC data from the rock surfaces was lower as expected than on calibration targets (Figure 8); in applicable cases, data from several points were averaged to remove the impact of cosmic rays and improve signal.

3.8.10 Image processing

Image processing on both WATSON and ACI products was performed using a Python script to register several images for a single target to create an overlay. The script uses the OpenCV library built in classes to implement BRISK keypoint detection and a FLANN-based matcher to match keypoints to generate the overlays. ACI ECM products and WATSON ECM or ECZ (roughly 4 to 10 cm standoff) images were used in all cases. Colourized ACI products used for correlating spectral, colour and textural information were generated as previously described16. Small artefacts of bright colours are visible in these colourized images in certain cases.

3.8.11 SHERLOC analogue instrument data

Reference spectra presented were collected on two laboratory instruments, Brassboard (Jet Propulsion Laboratory) and MORIARTI (Mineralogy and Organics Raman Instrumentation for the Analysis of Terrestrial Illumination) (University of Pittsburgh), that are analogues of SHERLOC modified to operate under terrestrial ambient conditions. Brassboard configuration and operations are described in previous literature [105]. MORIARTI is a custom DUV Raman microscope coupled with several spectrometers to cover the entire Raman and fluorescence (UV and visible light) spectral range. Samples can be illuminated with ei-

ther a Coherent Industries Innova 300 FreD frequency-doubled Ar+ laser (248.3 nm, roughly 10 mW average power) or a Photon System NeCu laser (248.6 nm, roughly 20 μJ per pulse, 80 Hz). Laser light passes through a 248.6 nm laser clean up filter before being focused onto a turning prism and directed onto the sample as a roughly 120 μm diameter spot. Scattered and emitted light is collected in a 180° backscatter geometry using an f1.25 reflective cassegrain objective and passes through a Semrock 248 nm long-pass filter before entering one of the spectrometers. For Raman, light is dispersed from 250 to 278 nm to a resolution of 9 cm^{-1} inside an f/6.8 Czerny–Turner spectrograph and focused onto a Princeton Instruments liquid nitrogen cooled Pylon 400B CCD. For UV fluorescence, light is dispersed from 180 to 350 nm to a resolution of 0.5 nm by a custom Ocean Optics QE Pro spectrograph. For visible fluorescence, light is dispersed from 250 to 1,100 nm, to a resolution of 1.5 nm by an Ocean Optics HR4000 spectrograph. The sample can also be illuminated by a halogen white light, in which it is imaged onto a 1.6MP Thorlabs CMOS camera.

3.9   Data availability

The data used for this study are released on the Planetary Data System (PDS) at `https://pds.nasa.gov/`. Data from the SHERLOC instrument are accessible at `https://pds-geosciences.wustl.edu/missions/mars2020/sherloc.htm`. Spectral data are organized by sol number and accessible in csv format at `https://pds-geosciences.wustl.edu/m2020/urn-nasa-pds-mars2020_sherloc/data_processed/`. Fundamental data record image data acquired by the ACI are organized by sol number and accessible in IMG format at `https://pds-imaging.jpl.nasa.gov/data/mars2020/mars2020_imgops/data_aci_imgops/sol/`. Fundamental data record image data acquired by the WATSON are organized by sol number and accessible in IMG format at `https://pds-imaging.jpl.nasa.gov/data/mars2020/mars2020_imgops/data_watson_imgops/sol/`.

3.10   Code availability

All code used for image and data processing in this manuscript uses open-source libraries or previously published methods described herein. The code for ACI colorization is available under the Apache 2.0 licence at `https://github.com/nasa-jpl/ACI-colorization`. Loupe software is open source under the Apache 2.0 licence and available at `https://github.com/nasa/Loupe`.

3.11   Acknowledgements

3.12   Author Information

These authors contributed equally: Sunanda Sharma, Ryan D. Roppel

3.12.1   Contributions

S.S. and R.D.R. contributed equally to data analysis, drafting the manuscript and figures with substantial contributions from A.E.M. and A.S. A.E.M., R.B., A.S., J.R.H., S.V.B.,

A.C. and R.S.J. helped in data analysis and interpretation. A.E.M., L.W.B., R.B., A.C., A.S., W.J.A., B.L.B., E.L.C., P.G.C., A.D.C., K.E., A.C.F., D.H., J.H., S.I., L.C.K., C.L., A.M., M.M., A.P., C.R., A.W., R.C.W. A.J.W., K.W., M.W. and A.Y. helped with M2020 surface operations. L.W.B. and R.B. are the former principal investigator and deputy investigator, respectively, of the SHERLOC instrument. M.M. is the current interim principal investigator of the SHERLOC instrument and K.U. is the current deputy investigator. K.A.F. and K.M.S. are the project scientist and deputy project scientists, respectively, of the M2020 mission. All authors reviewed and edited the manuscript before submission.

3.12.2 Ethics Declaration

The authors declare no competing interests.

3.13 Peer Review

Nature thanks Philippe Schmitt-Kopplin and Dominic Papineau for their contribution to the peer review of this work.

4.0   Conclusions

This thesis demonstrated the utility of continuous wave instead of pulsed deep UV lasers for UV resonance Raman measurements and also how the first deep UV Raman spectrometer on another planet was used for fluorescence and Raman detection on Mars.

Chapter 1 discussed: a background of light/matter interactions, why deep UV Raman is important, and how various instruments can measure electronic and vibrational molecular information. This discussion provides a context for the reader to appreciate the more technical chapters that followed.

In Chapter 2, phenolate is shown to exhibit non-linear behavior such as changes in band intensity, the formation of a phenoxy radical, and LIBS plasma formation when using a pulsed deep UV laser. These non-linear behaviors affect the spectral integrity of the sample by introducing additional bands and reducing signal to noise. By using a CW laser, not only were the spectral artifacts eliminated, but by increasing the amount of average power on the sample, more Raman photons were generated and detected, which significantly increased signal to noise.

In Chapter 3, numerous fluorescent signals were detected during the Jezero crater floor campaign that may be interpreted as potentially organic due to their variability and band-shape. Inorganic contributions from Lanthanide metals trapped within the matrix cannot be ruled out as fluorescence results in broad, non-identifiable bands that tend to overlap in the same spectral window as those of the potential organic bands. Additionally, one particular Raman spectrum contained a peak that could be a potential graphitic carbon band or ring mode of an aromatic molecule. These are the first results to summarize the diversity of fluorescence detected and becomes the first step towards characterizing the samples when they return in the early 2030s as part of the Mars Sample Return program.

4.1 Future Work

There has been significant technological development of deep UV Raman systems in the past decade. A deep UV Raman system requires 3 main components: a laser, a spectrometer, and a computer with an analysis package. Reducing SWaP (**S**ize, **W**eight, **a**nd **P**ower) requirements enables deep UV Raman systems to moved out of the laboratory and into field applications.

Previous deep UV lasers, such as an Ar-ion or Excimer lasers, were large, bulky, and very power inefficient. These lasers were only being used in controlled laboratory conditions. Recently the Asher group has co-developed and commercialized with UVisIR two compact diode-pumped solid-state lasers at 213 and 228 nm for use in standoff explosive detection using Raman spectroscopy [15, 16]. Other companies such as Passat and Quantum Light Instruments have also brought compact deep UV lasers to market. Even continuously wavelength tunable systems have begun to be ruggedized for field use, such as one by M Squared that could be dropped out of a building and required minimal alignment to lase. Continuously tunable lasers can enable exciting on multiple different transitions, which could be useful to measure complex mixtures of compounds [8, 102]. Additionally, in Chapter 2, continuously wavelength tunable lasers can be designed to be continuous wave, which reduces or eliminates non-linear behavior from samples with high optical absorbances.

Deep UV spectrometers generally require high dispersion and long path-lengths in order to resolve Raman bands as their frequencies are close to the laser line and their bandwidths are narrow. For example, a 1000 cm^{-1} band will have a wavelength shift of of 4.64 nm when excited with 213 nm light and a 1010 cm^{-1} band will have a wavelength shift of 4.68 nm, a difference of only 0.04 nm. To resolve a small change on a detector, a large path-length of 100s of cm is needed, far from compact. Optical design software packages such as Zemax can aid in the construction of smaller systems. Recently developed spectrometers have begun to use folded optical designs, such as in SHERLOC, so that the spectrometer optical path does not need to be in the same plane, which can significantly reduce the size, but at a cost of potentially more stray light and artifacts from optical components [130, 53].

Laptop and desktop computers are currently used along with some analysis software to

communicate with the laser and spectrometer and display the Raman data. However, advances in smaller lower-SWaP edge computing devices such as the Arduino, Google Coral, and Nvidia Jetson will leverage the power of GPU (graphics processing unit) and specialized AI (artificial intelligence) chips to enable fast acquisition and analysis of Raman measurements [7]. Currently AI and neural networks are widely used in image recognition and are beginning to be used in planetary observation and Raman spectral identification [25, 79, 140]. For spectral identification, large data sets of Raman spectra will need to be compiled, and since deep UV Raman resonantly enhances bands and their peak intensities and frequencies, a multi-wavelength database will be needed as well. With continuously tunable deep UV lasers communicating with the grating position in the spectrometer, it is possible to scan at multiple different excitation frequencies and generate hyper-spectral data sets. Another approach is to forego the use of Raman for exact identification of a molecule, but instead use AI to solve a problem such as in forensics or disease diagnostics [33, 103].

Once field portable deep UV Raman systems become widely available and reduce in cost, they will likely outperform most visible Raman systems. Fluorescence has long plagued the visible Raman spectrometer industry and although there are clever tricks to reduce its influence, such as differential Raman spectroscopy or specialized baseline-compensating algorithms, eliminating it completely from the measurement is ideal [87, 135]. Deep UV Raman can utilize specific wavelengths to resonantly enhance key molecules so that complex mixtures can be easier to characterize. Overall the future for deep UV Raman remains promising due to the rapid innovations in lasers, optics, and computing.

Appendix A Chapter 2 Supplementary

A.1   Spectra-Physics Continuously Tunable Continuous Wave Laser

The Spectra-Physics laser system is single-mode continuously tunable, continuous wave from 206-1000 nm. It is composed of numerous modules as seen in Figure 10. The Millennia eV, a 532 nm diode pumped solid state laser, pumps a Ti-Sapphire rod inside of the Matisse CR, which lases from 650-1000 nm. This light can be doubled in the first Wavetrain module to generate 350-500 nm light, and then can be quadrupled in a second Wavetrain module to generate 206-250 nm light. Or, the Ti-Sapphire light can be mixed with a 1.95 μm AdValue Photonics fiber laser/amplifier inside of the Mixtrain module, which generates 500-700 nm light and then can be doubled in a third Wavetrain module to generate 250-350 nm light.

The Matisse CR module contains a Ti-Sapphire rod that lases in a continuum. A birefrigent filter acts as a coarse bandpass filter and a thin etalon acts as a fine bandpass filter to reduce the bandwidth of the Ti-Sapphire output. To enable single frequency operation, the Matisse CR uses a piezo tunable etalon for a top-of-fringe lock to a single cavity mode. The Matisse CR has a linewidth <0.0003 cm^{-1}, much narrower than the natural Raman linewidth [89].

The Wavetrain modules are second (SHG) or fourth (FHG) harmonic generation cavities. Typically CW lasers do not have enough power to enable non-linear conversion with high efficiencies. The Wavetrains use enhancement cavities that allow multiple passes through the harmonic generation crystal to enable high efficiency. The Wavetrains are Pound-Drever-Hall stabilized to the input mode to ensure high conversion efficiency.

The Mixtrain module enables sum frequency generation (SFG) to shift the wavelength of the Ti-Sapphire. SFG is enabled by temperature tuning a periodically poled (PP) crystal. The temperature of the crystal, is stabilized using a PID controller, which allows narrow wavelength control.

We tuned the laser to 266 nm, where the Matisse-Mixtrain-Wavetrain is capable of outputting more than 200 mW of average power. Neutral density filters were used to decrease

the power as needed.
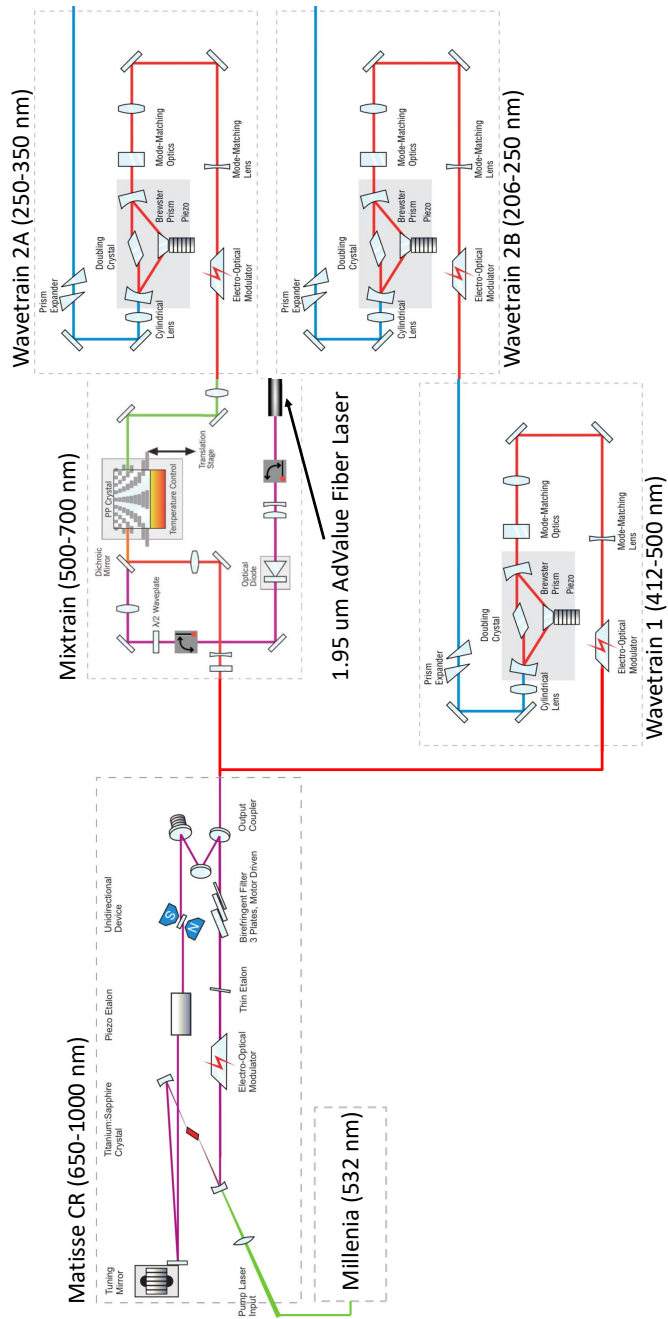
Figure 10: Block diagram of Spectra-Physics continuous wave laser system. Continuously tunable from 206-1000 nm.
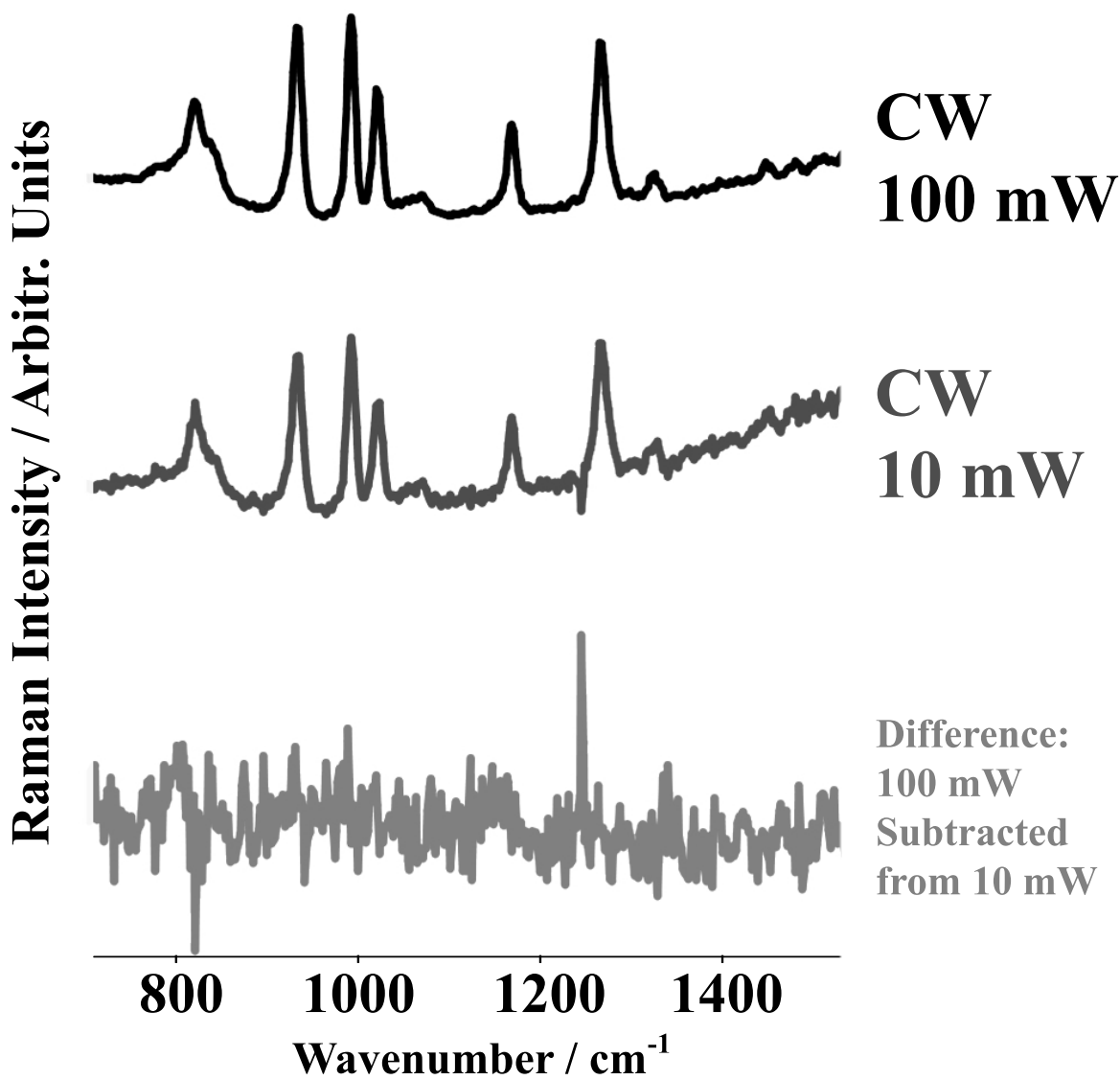
Figure 11: Lack of power dependence of CW excited resonance Raman spectra of phenolate solution at high and low CW average power: 100 mW (top), 10 mW (middle), and difference of 100 mW and 10 mW (bottom). The spike at 1250 cm^{-1} is a subtraction artifact due to noise on the CCD and is not a real peak.
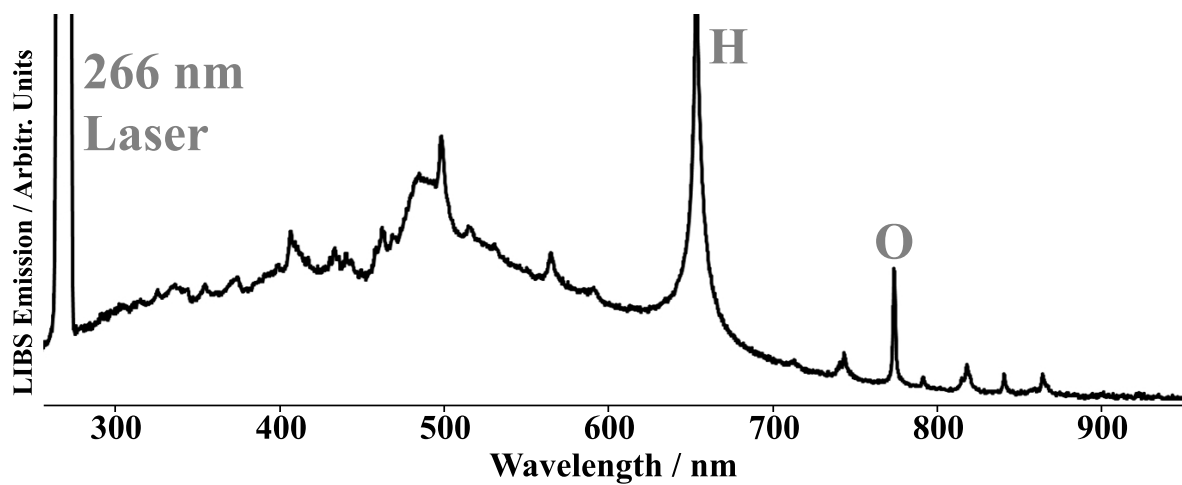
Figure 12: Emission of deionized water with 100 mW average power from pulsed laser. A hydrogen line at 656 nm and an oxygen line at 777 nm are caused from the photoionization of water.

Appendix B Chapter 3 Supplementary
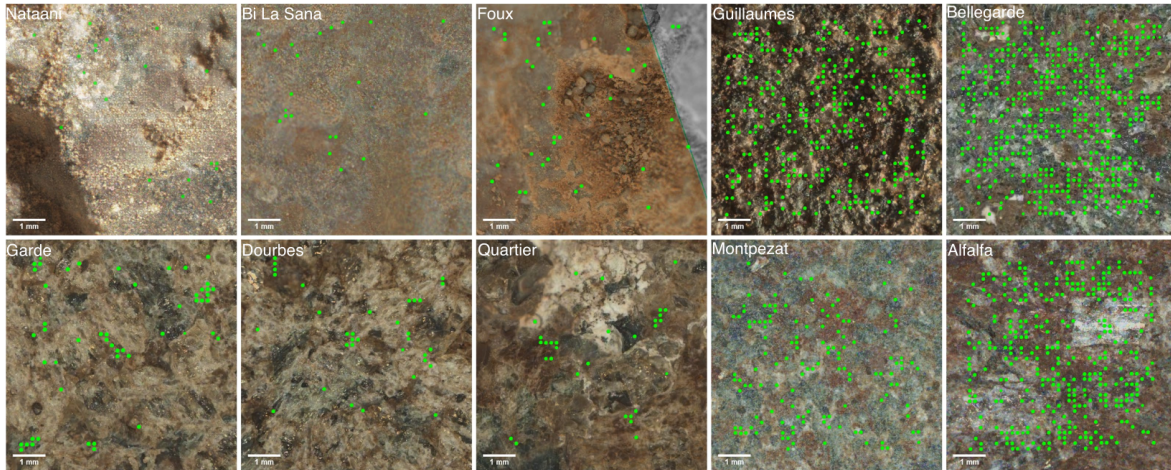
Figure 13: Colorized ACI images from survey scans of each of the 3 natural targets (top left), 4 Máaz abraded targets (right), and 3 Séítah abraded targets (bottom left). Green spots represent the relative laser beam diameter that have a positive identification for the ~335–350 nm fluorescence
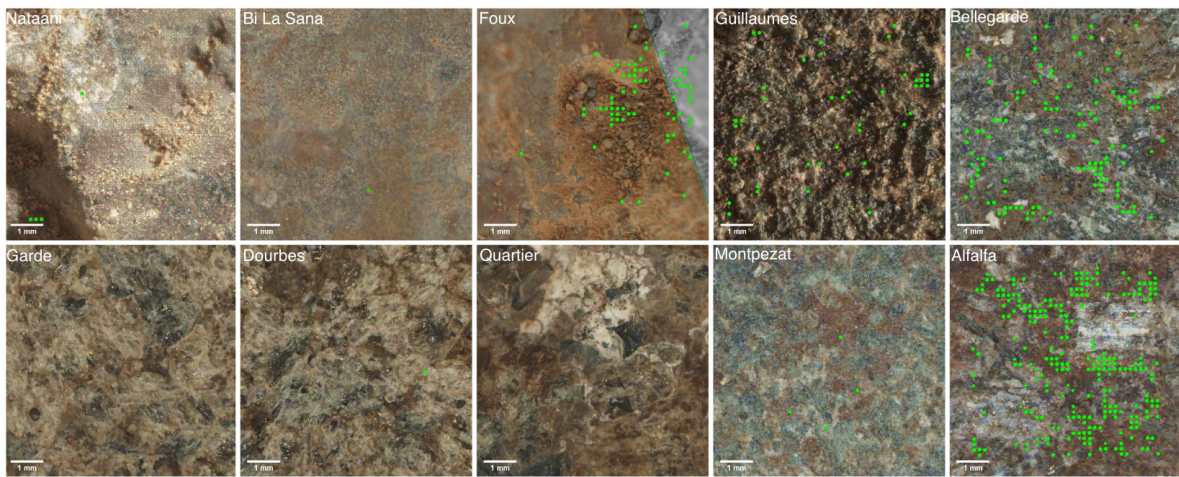
Figure 14: Colorized ACI images from survey scans of each of the 3 natural targets (top left), 4 Máaz abraded targets (right), and 3 Séítah abraded targets (bottom left). Green spots represent the relative laser beam diameter that have a positive identification for the ~270–295 nm fluorescence. No ~270–295 nm fluorescence was observed on survey scans in Garde and Quartier.

Benzothiophene
C$_8$H$_6$S
302
310

Benzoic Acid
C$_7$H$_{12}$O$_2$
306

Biphenyl
C$_{12}$H$_{10}$
318

Naphthalene
C$_{10}$H$_8$
338

Phthalic Acid
C$_8$H$_6$O$_4$
341

280   300   320   340

Wavelength (nm)
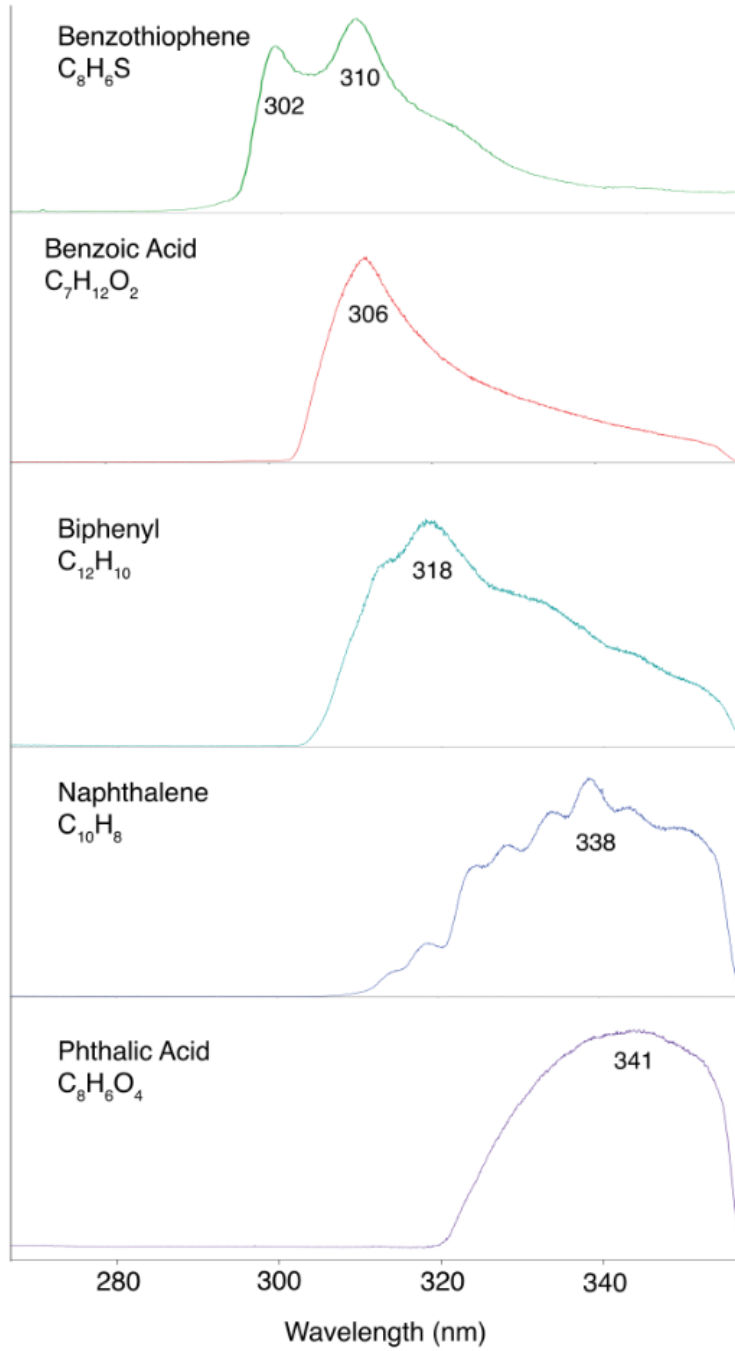
Figure 15: Fluorescence emissions of a sample set of 1- and 2-ring organic compounds analyzed on a SHERLOC analog instrument.
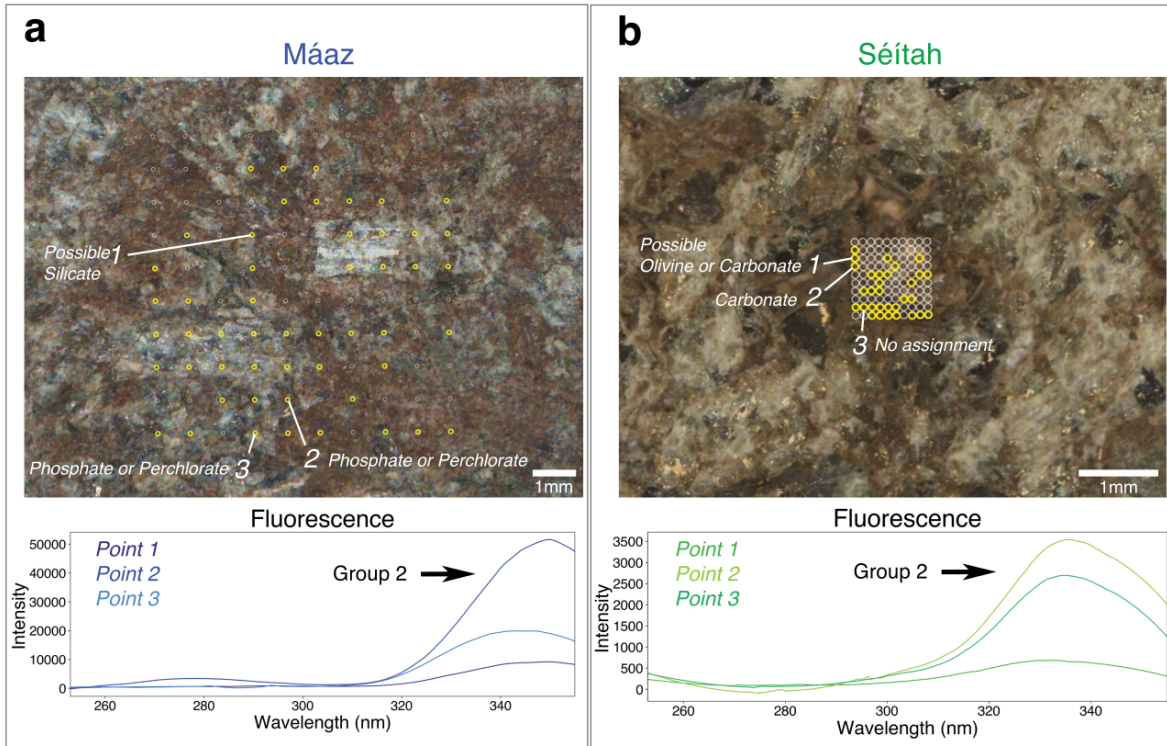
Figure 16: A) Colorized ACI of Alfalfa (Máaz fm.) HDR scan on sol 370 with laser overlay (grey = no fluorescence detected, yellow = fluorescence at ~335–350 nm detected). Three points of interest with clear fluorescence are marked in white and correlate to the smoothed mean spectra below. Point 1 was co-located with Raman detections of amorphous silicate (broad ~1063 cm^{-1}); Point 2 and 3 were co-located with potential perchlorate detections (961 cm^{-1}). B) Colorized ACI of Dourbes (Séítah fm.) Detail 1 scan on sol 269 with laser overlay (gray = no fluorescence detected, yellow = fluorescence at ~335–350 nm detected). Three points of interest with clear fluorescence are marked in white and correlate to the spectra below. Point 1 was co-located with Raman detections of potential olivine (~823 cm^{-1}) and carbonate (~1077 cm^{-1}); Point 2 was co-located with a potential carbonate detection (~10 cm^{-1}); and Point 3 with an unassigned peak at ~1015 cm^{-1}.
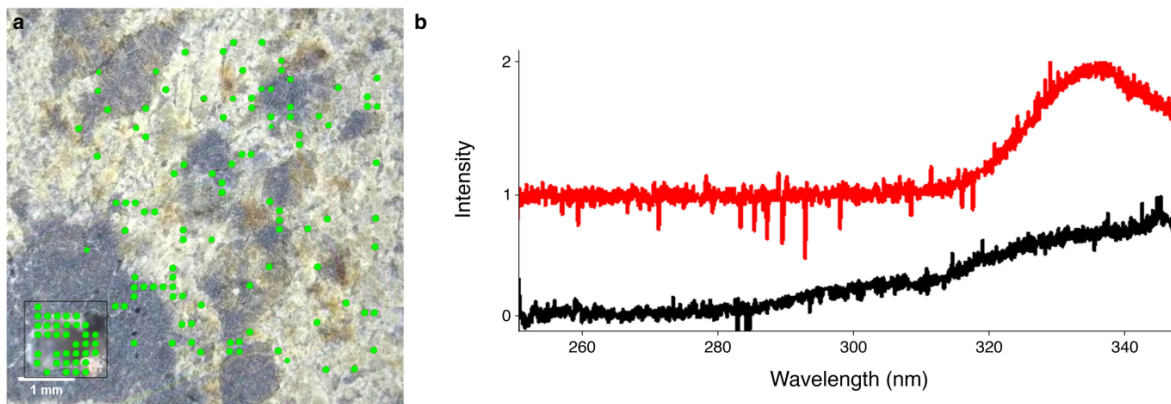
Figure 17: A) Colorized ACI image from a survey scan of the meteorite calibration target from sol 181. Green spots represent the relative laser beam diameter that have a positive identification for the ~335–350 nm fluorescence. B) Mean fluorescence spectra from locations by all green spots in A (red spectrum, n = 137) and mean fluorescence spectra from green spots bounded by the black box from the vug (black spectrum, n = 36).
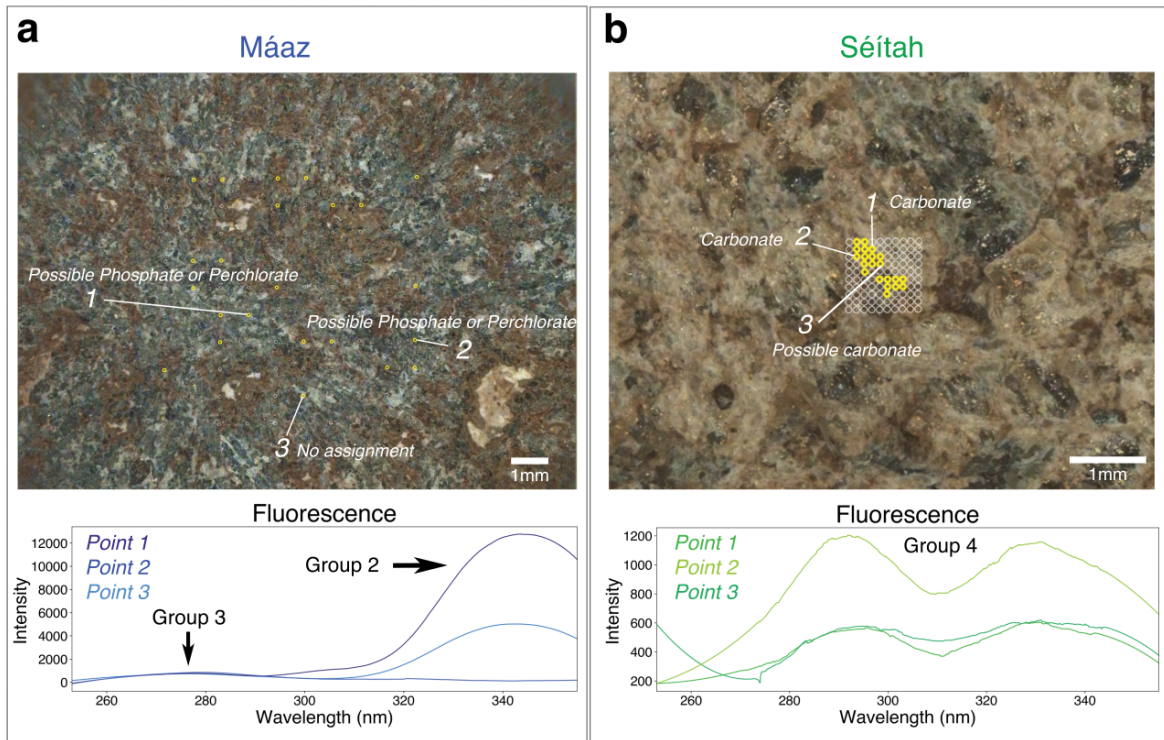
Figure 18: A) Colorized ACI of Bellegarde (Máaz fm.) HDR scan on sol 186 with laser overlay (gray = no fluorescence detected, yellow = fluorescence at 270–295 nm detected). Three points of interest with Group 3 fluorescence are marked in white and correlate to the smoothed mean spectra below. Point 1 and 2 were co-located with a potential phosphate or perchlorate detection ($\sim$973, $\sim$965 cm^{-1}); Point 3 was not co-located with a mineral detection. In all of these points, high intensity Group 2 fluorescence was also detected. B) Colorized ACI of Garde (Séítah fm.) Detail centre 1 scan on sol 208 with laser overlay (gray = no fluorescence detected, yellow = fluorescence at $\sim$290 & 330 nm doublet detected). Three points of interest with clear fluorescence are marked in white and correlate to the spectra below. All three points were co-located with Raman detections of potential carbonate ($\sim$1088, $\sim$1080, $\sim$1085 cm^{-1}).

Unit Name	Target Name	Target Type	Sol Number	Scan Parameters			
				Scan Size	Step Size	Spectra/scan	Pulses/point
Máaz	Nataani	Natural	83	7x7 mm	780 μm	100	5 ppp
				7x7 mm	780 μm	100	50 ppp
				7x7 mm	780 μm	100	100 ppp
				5x5 mm	200 μm	1296	10 ppp
Máaz	Bi la sana	Natural	98	7x7 mm	780 μm	100	100 ppp
				7x7 mm	780 μm	100	100 ppp
				7x7 mm	780 μm	100	300 ppp
				5x5 mm	144 μm	1296	15 ppp
Máaz	Foux	Natural	141	7x7 mm	780 μm	100	100 ppp
				7x7 mm	780 μm	100	100 ppp
				7x7 mm	780 μm	100	300 ppp
				5x5 mm	144 μm	1296	15 ppp
Máaz	Guillaumes	Abraded	161	7x7 mm	780 μm	100	100 ppp
				7x7 mm	780 μm	100	100 ppp
				7x7 mm	780 μm	100	300 ppp
				5x5 mm	144 μm	1296	15 ppp
Máaz	Guillaumes	Abraded	162	7x7 mm	780 μm	100	250 ppp
				7x7 mm	780 μm	100	250 ppp
				5x5 mm	144 μm	1296	15 ppp
Máaz	Bellegarde	Abraded	186	7x7 mm	780 μm	100	250 ppp
				7x7 mm	780 μm	100	250 ppp
				5x5 mm	144 μm	1296	15 ppp
Séítah	Garde	Abraded	207	7x7 mm	780 μm	100	500 ppp
				5x5 mm	144 μm	1296	15 ppp
Séítah	Garde	Abraded	208	1x1 mm	100 μm	100	500 ppp
				1x1 mm	100 μm	100	500 ppp
				1x1 mm	100 μm	100	500 ppp
Séítah	Dourbes	Abraded	257	7x7 mm	780 μm	100	500 ppp
				5x5 mm	144 μm	1296	15 ppp
Séítah	Dourbes	Abraded	269	1x1 mm	100 μm	100	500 ppp
				1x1 mm	100 μm	100	500 ppp
				1x1 mm	100 μm	100	500 ppp
				5x5 mm	144 μm	1296	15 ppp
Séítah	Quartier	Abraded	293	7x7 mm	780 μm	100	500 ppp
				5x5 mm	144 μm	1296	15 ppp
Séítah	Quartier	Abraded	304	1x1 mm	100 μm	100	500 ppp
				1x1 mm	100 μm	100	500 ppp
				1x1 mm	100 μm	100	500 ppp
				1x1 mm	100 μm	100	500 ppp
				1.75x1.75 mm	50 μm	1296	15 ppp
Máaz	Montpezat	Abraded	349	7x7 mm	780 μm	100	500 ppp
				5x5 mm	144 μm	1296	15 ppp
Máaz	Alfalfa	Abraded	370	7x7 mm	780 μm	100	500 ppp
				5x5 mm	144 μm	1296	15 ppp

Figure 19: Each scan analyzed in this study is listed here with its respective parameters; including size in millimeters, step size in microns, number of spectra per map, and pulses per point (ppp).

Target	Type	Formation	Sol / Scan / ppp	303 & 325	335-350	270-295	295 & 330	Mineral Association	Texture Assocation	ROI Fluorescence Spectrum
Nataani	Natural	Máaz	83 / HDR / 100		X			Not detected	No clear association	
Nataani	Natural	Máaz	83 / HDR / 100			X		Not detected	No clear association	
Bi la sana	Natural	Máaz	98 / HDR / 300		X			Not detected	No clear association	
Bi la sana	Natural	Máaz	98 / HDR / 300			X		Not detected	No clear association	
Foux	Natural	Máaz	141 / HDR / 300		X			Not detected	No clear association	
Foux	Natural	Máaz	141 / HDR / 300			X		Not detected	No clear association	
Garde	Abraded	Séitah	208 / Detail / 500		X			Carbonate, Silicate, Olivine, Phosphate or Perchlorate	Grain boundaries; On brown and off white grains	
Garde	Abraded	Séitah	208 / Detail / 500				X	Carbonate, Silicate	Intergranular spaces	
Dourbes	Abraded	Séitah	269 / Detail / 500		X			Olivine, Carbonate, Hydrated Sulfate, Phosphate or Perchlorate	On brown and off white grains	
Quartier	Abraded	Séitah	304 / Detail / 500	X				Hydrated Sulfate, Phosphate or Perchlorate, Olivine	On white grains	
Quartier	Abraded	Séitah	304 / Detail / 500		X			Carbonate, Olivine, Sulfate, Perchlorate, Possible Phosphate	On brown, black, and off-white grains	
Guillaumes	Abraded	Máaz	161 / HDR / 300		X			Sulfate, Perchlorate, Possible Phosphate	Grain boundaries; on grains	
Guillaumes	Abraded	Máaz	161 / HDR / 300			X		No clear association	Grain boundaries; on grains	
Guillaumes	Abraded	Máaz	161 / HDR / 300				X	No clear association	No clear association	
Bellegarde	Abraded	Máaz	186 / HDR / 250		X			Pyroxene or Sulfate, Silicate, Phosphate or Perchlorate	Grain boundaries, cracks; on black, brown, and off-white grains	
Bellegarde	Abraded	Máaz	186 / HDR / 250			X		Phosphate or Perchlorate; mostly not clearly associated	On black-brown grains	
Bellegarde	Abraded	Máaz	186 / HDR / 250	X				Sulfate, Perchlorate or Phosphate	On white grains	
Montpezat	Abraded	Máaz	349 / HDR / 500		X			Silicate, Possible Pyroxene, Phosphate or Perchlorate	Grain boundaries; on grains of many colors	
Montpezat	Abraded	Máaz	349 / HDR / 500			X		No clear association	Grain boundaries; on brown, reddish, off-white grains	
Alfalfa	Abraded	Máaz	370 / HDR / 500		X			Silicate, Pyroxene, Phosphate or Perchlorate, Carbonate	Grain boundaries; on brown, gray, off-white grains	
Alfalfa	Abraded	Máaz	370 / HDR / 500			X		Silicate, Phosphate or Perchlorate	Boundaries of black and gray grains	

Figure 20: A summary table indicating fluorescence, mineral, and textural observations for each target alongside representative fluorescence spectra for region of interest (ROI) for the detected feature group, defined by all the points within the scan that exhibited spectra with that group. All data shown here is compiled from the highest signal-to-noise ratio scan performed on each target.

Group	Compound	λ Max (nm)	Raman Peak (cm-1)	Citation	Previous Mars Detection	Martian Meteorite Detection	Description
303 & 325	Benzothiophene	~306, ~316	~1589, ~1494, ~1310, ~1252, ~1012, ~792	Extended Data Figure 3	Eigenbrode et al. 2018, Millan et al. 2021	not detected	Aromatic organic heterocycle
335-350	Naphthalene	337	1377 (Ring s.), 1623 (C=C s.)	Razzell Hollis et al. 2022	Eigenbrode et al. 2018	Tissint (Jaramillo et al. 2019), EET79001 (Sephton et al. 2002)	Polycylic aromatic hydrocarbon
335-350	Phenanthrene	350	1353 (Ring s.), 1612 (C=C s.)	Razzell Hollis et al. 2022	not detected	ALH84001 (Becker et al. 1999), DaG 476 (Steele et al. 2012)	Polycyclic aromatic hydrocarbon
335-350	Fluorene	338	1602 (C=C s.)	Razzell Hollis et al. 2022	not detected	EET79001 (Becker et al. 1997)	Polycyclic aromatic hydrocarbon
335-350	L-Lysine	350	1337 (NH2 r.), 1433 (COOH s.), 2925 (C-H s.)	Razzell Hollis et al. 2022	not detected	not detected	L-alpha amino acid
335-350	L-Aspartic Acid	350	1412 (COOH s.), 1685 (C=O s.), 2967 (C-H s.)	Razzell Hollis et al. 2022	not detected	Nakhla (Glavin et al. 1999)	Aliphatic carboxylic amino acid
270-295	L-Tyrosine	~280	not reported	Bhartia et al. 2008	not detected	not detected	Aromatic amino acid
270-295	L-Tyrosine	303	842 (Ring br.), 1201 (Ring s.), 1614 (Ring s.)	Razzell Hollis et al. 2022	not detected	not detected	Aromatic amino acid
270-295	L-Tyrosine	~295	1202 (C=C s.), 1617 (C=C s.)	Bhartia et al. 2021, Abbey et al. 2017	not detected	not detected	Aromatic amino acid
270-295	L-Phenylalanine	~280	not reported	Bhartia et al. 2008	not detected	not detected	Aromatic amino acid
270-295	L-Phenylalanine	294	1004 (Ring br.), 1204 (Ph-C s.), 1623 (Ring s.)	Razzell Hollis et al. 2022	not detected	not detected	Aromatic amino acid
270-295	L-Histidine	278	1317 (NH2 R.), 1492 (imidazole b.), 1568 (imidazole b.)	Razzell Hollis et al. 2022	not detected	not detected	Aromatic heterocyclic polar amino acid
270-295	Phthalic Acid	339	1601 (C=C s.)	Bhartia et al. 2021, Abbey et al. 2017	not detected	not detected	Aromatic carboxylic acid
270-295	Benzene	~280	1600-1685 (Ring s.)	Bhartia et al. 2021, Abbey et al. 2017	Eigenbrode et al. 2018	Tissint (Jaramillo et al. 2019), DaG 476 (Steele et al. 2012), Nakhla and EET79001 (Sephton et al. 2002)	1 ring aromatic
270-295	Benzoic Acid	304	1614 (C=C s.), 3227 (overtone)	Razzell Hollis et al. 2022	Millan et al. 2021	not detected	Aromatic carboxylic acid
Other	Mellitic acid	315	1608 (C=C s.), 1685 (COOH s.)	Bhartia et al. 2021, Abbey et al. 2017	not detected	not detected	Aromatic carboxylic acid
Other	Mellitic acid	315	1200-1700 (Ring s., carboxylic acid s.), 3100-3300 (O-H s.)	Razzell Hollis et al. 2022	not detected	not detected	Aromatic carboyxlic acid
Other	L-Tryptophan	333	1014 (Both rings br.), 1349 (Pyrrole s.), 1617 (Phenyl s.)	Razzell Hollis et al. 2022	not detected	not detected	Aromatic amino acid
Other	L-Valine	292	1341 (NH2 r.), 1408 (COOH s.), 2915 & 2980 (C-H s.)	Razzell Hollis et al. 2022	not detected	RBT04262 (Callahan et al. 2013)	Aliphatic amino acid
Other	L-Isoleucine	293	1338 & 1410 (C-H b.), 2890 & 2950 (C-H s.)	Razzell Hollis et al. 2022	not detected	not detected	Aliphatic amino acid

Figure 21: The four fluorescence feature categories were developed based on known patterns of fluorescence of one-ring and polycyclic aromatic compounds. Each compound of relevance is presented with known fluorescence bands and Raman peaks, [12, 113, 107, 73, 63, 116, 10, 45, 17, 1]description, and previous detection on Mars [93, 38] or within Martian meteorites [121, 106, 43, 119, 81, 2].

Appendix C Laser Alignment Tips and Tricks

The famous science fiction writer Arthur C. Clarke once wrote, "Any sufficiently advanced technology is indistinguishable from magic." [21]. Generating laser light does appear at first glance to be "magic." However, a laser simply manipulates light with a series of physical optics and crystals while simultaneously obeying Maxwell's equations of electromagnetism. This chapter will provide some basic tips for most any laser alignment and also a standard operating procedure I wrote specifically for Spectra Physics laser that generates continuous wave, continuously tunable deep UV photons as mentioned previously in Chapter 2 and in Appendix A. The standard operating procedure is not comprehensive, but anyone with a familiarity with the system should be comfortable following it.

C.1   3 Tips for Troubleshooting and Maintaining a Laser

1. **Read the schematic or manual.** These provide a lot of background to get started. Even if a manual is not provided, search for manuals from other similar laser classes, as lasers from the same class (gas ion, YAG, Ti-Sapphire) aren't going to vary significantly from one manufacturer to another. Some laser manufacturers are a bit cautious of sending out manuals without a service call, so another way to obtain information about a laser is by searching scientific publications and contacting the graduate or postdoctoral student who used the laser. Hopefully there is a logbook or service paperwork that lists how much power the laser can output at various current/voltage settings to use as a starting point. Components can age or degrade over time, so resist the urge to run a laser at the highest power settings as this will damage parts faster. For lasers with doubling or mixing stages, ensure that the pump power before the doubling or mixing stage is sufficient for lasing before adjusting the harmonic cavities.

2. **Inspect and clean optics frequently.** Unless the laser is located in a class 1 cleanroom or under vacuum, dust and organic contaminants can easily deposit onto anything.

Keeping the laser under positive pressure by purging with a dry inert gas can help. While the laser is off, use a small mirror and a flashlight to check if optics are hazy, have spots, or cracks. If an optic does appear dirty, use spectroscopic grade acetone or methanol on a folded square of a Kimwipe or lens paper to clean. It is best practice to minimize water absorption of the solvent by storing the solvent with clean, baked molecular sieves or using fresh solvent. Water will permanently dissolve crystals and gain media. Wipe across the surface once, applying moderately strong pressure and then discard the lens paper. Even if an optic cannot be cleaned or has a chip or crack, it is most often still salvageable by moving the beam onto an undamaged part of the optic.

3. **Adjust optics in a logical and methodical way.** The optics farthest away from the laser cavity generally affect output power the least and become more sensitive closer or inside the cavity. If any optic is adjusted, always know how to return back to the same position before the optic was adjusted. Adjusting multiple optics at a time is a recipe for disaster, because once the laser stops lasing, it is orders of magnitude more difficult to get it to lase again. Depending on the wavelength, some lasers are invisible to the human eye, so an IR beam viewer or a white business card can aid with visibility. In either case, be careful that the laser power is not too high or the beam viewer phosphor can be damaged or the paper card can burn.

C.2   Spectra-Physics Continuously Tunable Continuous Wave Laser Operating Procedure

The Spectra Physics continuously tunable CW laser system likely has the largest footprint that can be purchased from Spectra Physics and the most components that may need to be adjusted for operation. This makes this system quite versatile, but also requires patience. The Wavetrain harmonic stages in particular can be challenging because they are manually phase-matched and mode-matched to generate light. There are three main steps to starting up the laser: turning on the pump laser, aligning the Ti-Sapphire fundamental cavity, and peaking the power from the harmonics cavities.

C.2.1 Millennia (532 nm Pump Laser)

1. Check that the pump is on, at temperature (20C), and that the water fill line is at the full mark.

Figure 22: Laser Chiller

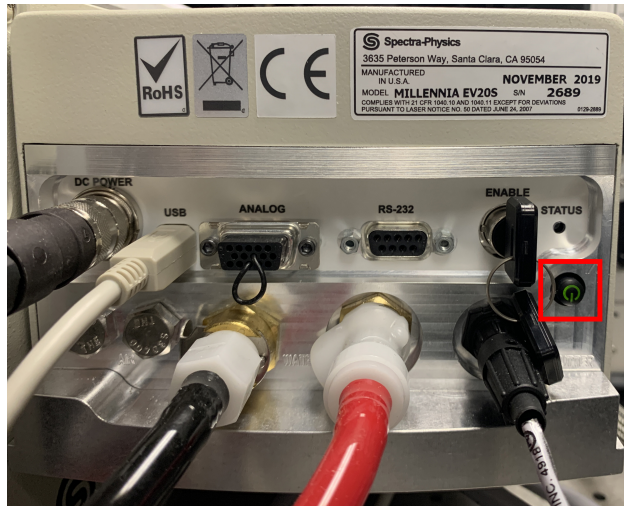2. Check that the power button is on the rear of the laser. It should be green.

Figure 23: Millennia Rear

3. Click the Spectra-Physics icon on the desktop to open the Millennia control software.
4. The control window should open. If the system status is ready, you can toggle the emission switch to the on position by clicking the icon in the right-hand corner. A window will pop-up confirming your decision to turn on the laser.
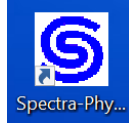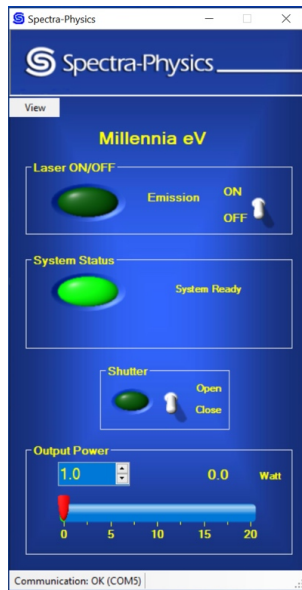
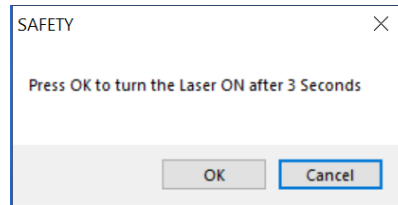Figure 24: Millennia Icon

Figure 25: Millennia Software Main Screen

Figure 26: Millennia Safety Pop-up

5. When the green Laser ON/OFF indicator turns green, you can open the shutter and increase the current. It is not necessary to ramp the current, as the software will automatically do this. To get UV power, you need 12-13W of Millennia power. It is very important that you have the shutter open during the warm up, so that the optics in the Ti-Sapphire cavity can stabilize.
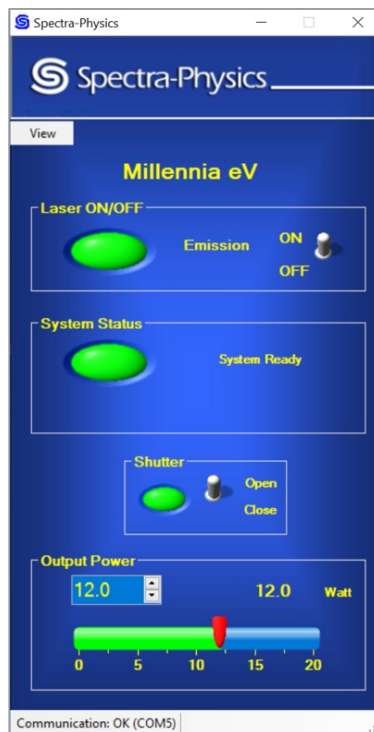
Figure 27: Millennia Software Running

6. Now wait for 1 hour. Do not rush this step. If you don't allow the laser to stabilize it will be very difficult to maintain a stable lock in the next step.

C.2.2 Matisse (Ti-Sapphire Laser)

1. Open the Matisse Commander software with the icon on the desktop.

Figure 28: Matisse Icon

2. Open the picomotor by going to Picroscrew Plug-In -> Picomotor.
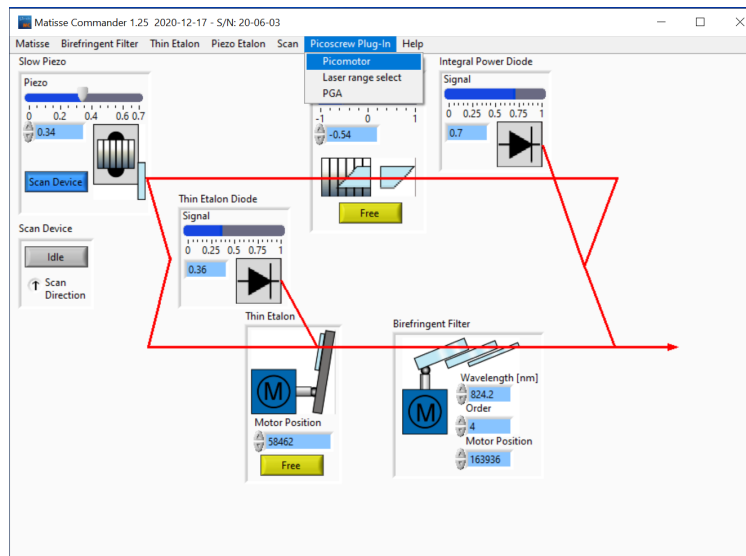
Figure 29: Matisse Commander Main Screen Picomotor

3. Click Refresh Laser. After it finishes, close the window by clicking Ok.
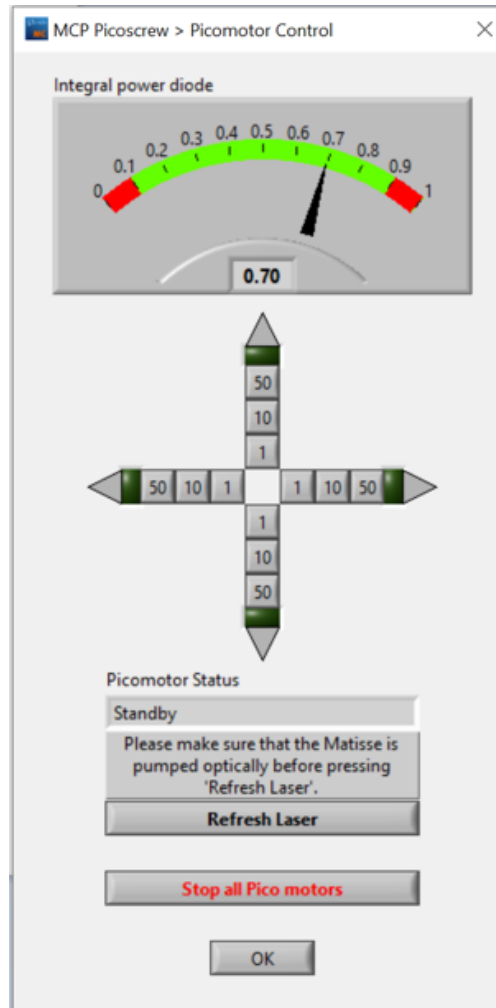
Figure 30: Picomotor Main Screen

4. Right click the Birefringent filter and select Scan.
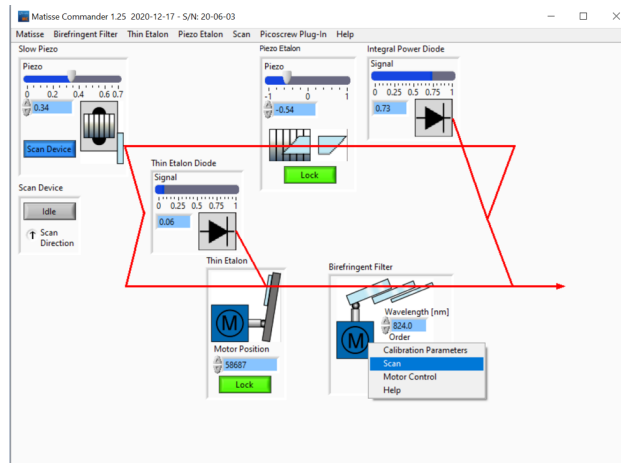
Figure 31: Matisse Commander Main Screen BiFi

5. In the new window click Start Scan. After the scan completes, you want the vertical red line, indicating the current motor position, to be centered on the center of a red/blue band. See below for an example. Then close the window.
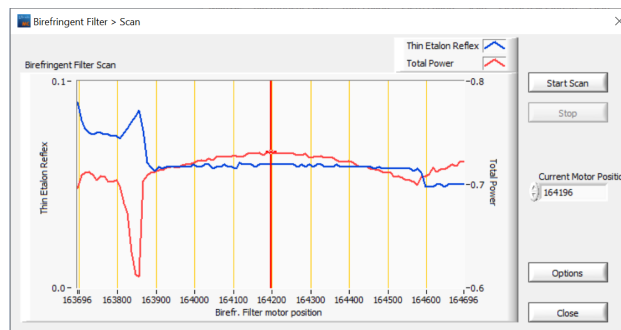
Figure 32: BiFi Main Screen

C.2.3 Wavetrains (Harmonics)

1. Check that the oscilloscope is on and that the connections are as follows, the upper box controls the FHG and the lower box controls the SHG:

   a. Channel 1: Error; 100mV scale

   b. Channel 2: Intensity; 1-5V scale

   c. Channel 3: Trigger; set channel 1 and 2 to use 3 as trigger

2. Flip the Scan/Stabilize switch on the Wavetrain control box to the Scan position.
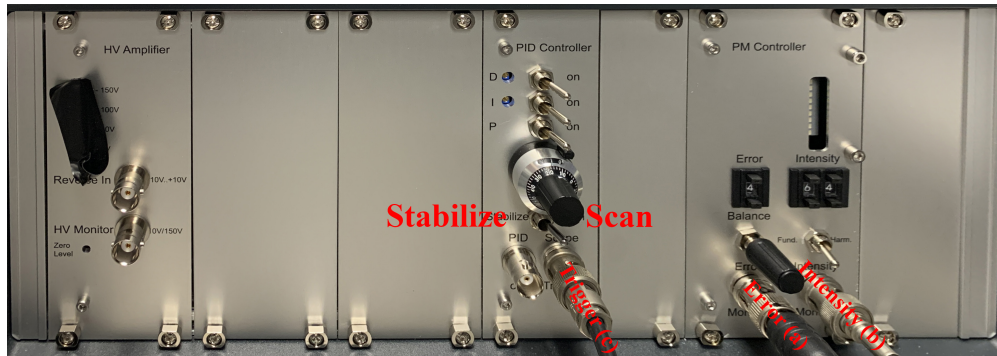
Figure 33: Wavetrain Control Box Scan/Stabilize

3. Remove the cover from the Wavetrain box to gain access to the cavity. There are 7 knobs that can be adjusted. The knobs on the right move a thin quartz plate that adjusts the input beam position. The red knobs control the vertical position of the cavity end mirrors. The yellow knobs control the horizontal position of the cavity end mirrors. The silver knob in the middle adjusts the crystal angle.
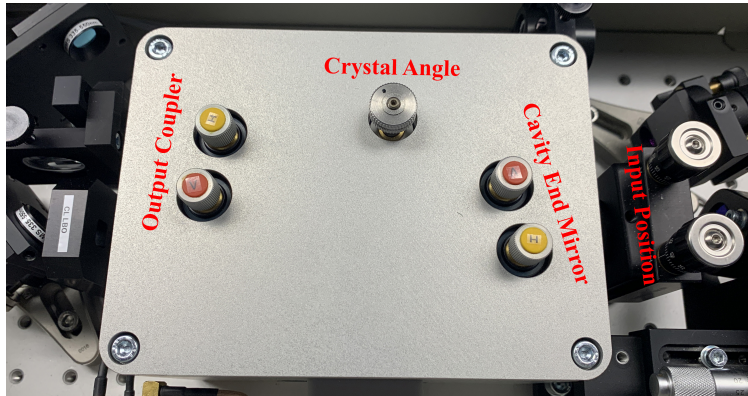
Figure 34: Wavetrain Cavity Controls

4. Starting with the input beam knobs, adjust until the oscilloscope shows something that looks like the picture below. The blue trace is the intensity and should show only one tall peak. The yellow trace is the error signal and should show a derivative shape. If needed you can also move the cavity end mirrors vertically or horizontally until you get a single tall peak in the blue trace. Note, the 2 peaks to the right of the tall blue peak and yellow error signal are signal reflections and irrelevant. Also, you'll see a duplicate of the peaks on the left, due to the long time constant.
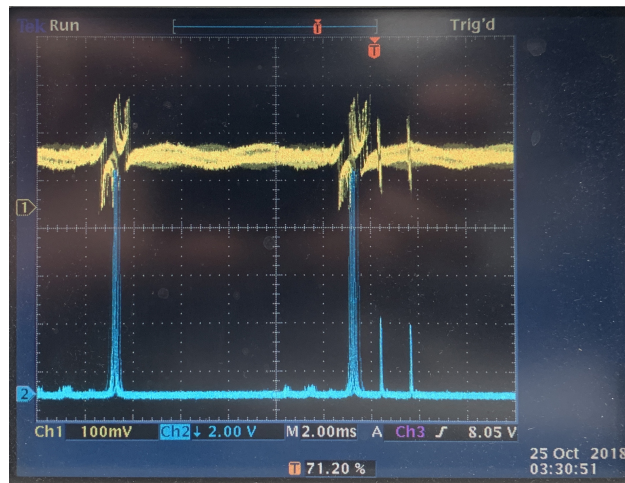
Figure 35: Oscilloscope Scan Mode

5. Once satisfied, flip the Scan/Stabilize switch on the Wavetrain control box to the Stabilize position. You should get similar traces on the oscilloscope as seen below.
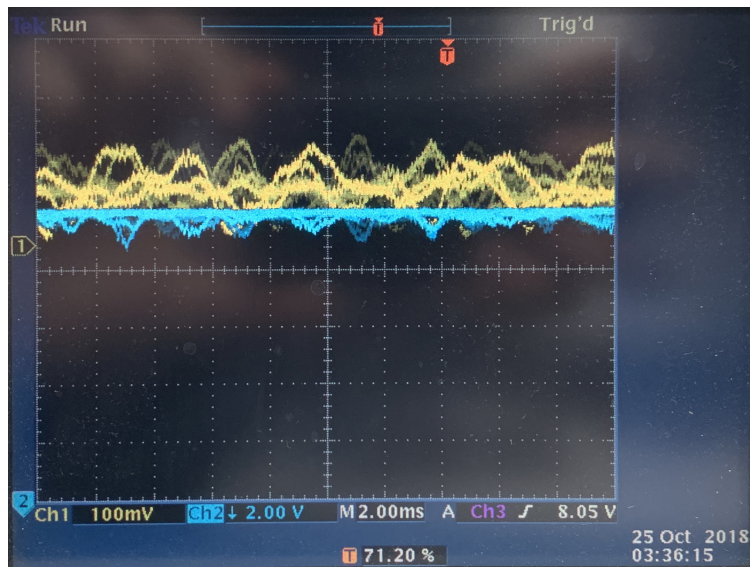
Figure 36: Oscilloscope Stabilize Mode

6. If the blue trace is not moving, if there is flickering in the vertical direction, or if you hear an audible clicking sound from the cavity, first adjust the DC balance knob on the control box until the blue trace appears stabilized.

Figure 37: Wavetrain Control Box DC Knobs

7. Place a power meter on the outside of the box, collecting the output SHG beam.
8. Starting with the input beam knobs, optimize the cavity so that the highest power is measured on the power meter. Any of the knobs can be adjusted: input, cavity end mirrors, or crystal angle and the DC balance and DC gain on the control box. If at any time you completely lose power and can't get it back, flip the switch back to Scan and check to ensure you see a good error signal and a single blue peak.
9. Once satisfied with power, replace the cover for the Wavetrain, remove the power meter so that the output beam can enter the next Wavetrain and wait 20-30 minutes for the FHG Wavetrain to stabilize.
10. Repeat all the same steps in 3 for the FHG Wavetrain, ensuring that the cables are flipped to the other box, but the same channels on the oscilloscope. The FHG is much more sensitive than the SHG, so be sure your SHG is as stable as possible before moving onto the FHG. Note, even with active stabilization, it can be useful to refresh and check the picomotor and the birefringent filter (steps 2b-e) as they can sometimes drift after a couple of hours.

C.2.4 Shutdown

1. Put both Scan/Stabilize switches in the middle position (not scan or stabilize).

2. Flip the emission switch to Off in the Millennia control software.

3. Turn off oscilloscope.

4. Everything else can stay on, as long as the Millennia is off and the piezo stages are not clicking (scan/stabilize switch) on the Wavetrains are set to the middle position.

Bibliography

[1] William J. Abbey, Rohit Bhartia, Luther W. Beegle, Lauren DeFlores, Veronica Paez, Kripa Sijapati, Shakher Sijapati, Kenneth Williford, Michael Tuite, William Hug, and Ray Reid. Deep UV Raman spectroscopy for planetary exploration: The search for in situ organics. *Icarus*, 290:201–214, July 2017.

[2] Carl B Agee, Nicole V Wilson, Francis M McCubbin, Karen Ziegler, Victor J Polyak, Zachary D Sharp, Yemane Asmerom, Morgan H Nunn, Robina Shaheen, Mark H Thiemens, Andrew Steele, Marilyn L Fogel, Roxane Bowden, Mihaela Glamoclija, Zhisheng Zhang, and Stephen M Elardo. Unique meteorite from early Amazonian Mars: Water-rich basaltic breccia Northwest Africa 7034. *Science*, 339(6121):780–785, February 2013.

[3] Sanford A Asher. Ultraviolet Raman Spectrometry. In *Handbook of Vibrational Spectroscopy*, volume 1, pages 1–15. John Wiley and Sons Ltd, New York, NY, 2002.

[4] Sanford A. Asher, Richard W. Bormett, X. G. Chen, Donald H. Lemmon, Namjun Cho, Pete Peterson, Marco Arrigoni, Luis Spinelli, and Jeff Cannon. UV resonance raman spectroscopy using a new cw laser source: Convenience and experimental simplicity. *Applied Spectroscopy*, 47(5):628–633, May 1993.

[5] Sanford A. Asher, Craig R. Johnson, and James Murtaugh. Development of a new UV resonance Raman spectrometer for the 217–400-nm spectral region. *Review of Scientific Instruments*, 54(12):1657–1662, December 1983.

[6] M. A. Bakane, C. P. Joshi, S. V. Moharil, P. L. Muthal, and S. M. Dhopte. Luminescence studies of decomposition of ceric sulfate. *Luminescence*, 26(6):553–556, November 2011.

[7] Stephan Patrick Baller, Anshul Jindal, Mohak Chadha, and Michael Gerndt. DeepEdgeBench: Benchmarking Deep Neural Networks on Edge Devices. *arXiv*, 2021.

[8] G. Batignani, E. Pontecorvo, G. Giovannetti, C. Ferrante, G. Fumero, and T. Scopigno. Electronic resonances in broadband stimulated Raman spectroscopy. *Scientific Reports*, 6(1):18445, January 2016.

[9]   A. Baumer, Ph. Blanc, F. Cesbron, and D. Ohnenstetter. Cathodoluminescence of synthetic (doped with rare-earth elements) and natural anhydrites. *Chemical Geology*, 138(1):73–80, May 1997.

[10]   L. Becker and T. E. Bunch. Fullerenes, fulleranes and polycyclic aromatic hydrocarbons in the Allende meteorite. *Meteoritics & Planetary Science*, 32(4):479–487, July 1997.

[11]   S A Benner, K G Devine, L N Matveeva, and D H Powell. The missing organic molecules on Mars. *Proc. Natl. Acad. Sci. U. S. A.*, 97(6):2425–2430, March 2000.

[12]   Rohit Bhartia, Luther W Beegle, Lauren DeFlores, William Abbey, Joseph Razzell Hollis, Kyle Uckert, Brian Monacelli, Kenneth S Edgett, Megan R Kennedy, Margarite Sylvia, David Aldrich, Mark Anderson, Sanford A Asher, Zachary Bailey, Kerry Boyd, Aaron S Burton, Michael Caffrey, Michael J Calaway, Robert Calvet, Bruce Cameron, Michael A Caplinger, Brandi L Carrier, Nataly Chen, Amy Chen, Matthew J Clark, Samuel Clegg, Pamela G Conrad, Moogega Cooper, Kristine N Davis, Bethany Ehlmann, Linda Facto, Marc D Fries, Dan H Garrison, Denine Gasway, F Tony Ghaemi, Trevor G Graff, Kevin P Hand, Cathleen Harris, Jeffrey D Hein, Nicholas Heinz, Harrison Herzog, Eric Hochberg, Andrew Houck, William F Hug, Elsa H Jensen, Linda C Kah, John Kennedy, Robert Krylo, Johnathan Lam, Mark Lindeman, Justin McGlown, John Michel, Ed Miller, Zachary Mills, Michelle E Minitti, Fai Mok, James Moore, Kenneth H Nealson, Anthony Nelson, Raymond Newell, Brian E Nixon, Daniel A Nordman, Danielle Nuding, Sonny Orellana, Michael Pauken, Glen Peterson, Randy Pollock, Heather Quinn, Claire Quinto, Michael A Ravine, Ray D Reid, Joe Riendeau, Amy J Ross, Joshua Sackos, Jacob A Schaffner, Mark Schwochert, Molly O Shelton, Rufus Simon, Caroline L Smith, Pablo Sobron, Kimberly Steadman, Andrew Steele, Dave Thiessen, Vinh D Tran, Tony Tsai, Michael Tuite, Eric Tung, Rami Wehbe, Rachel Weinberg, Ryan H Weiner, Roger C Wiens, Kenneth Williford, Chris Wollonciej, Yen-Hung Wu, R Aileen Yingst, and Jason Zan. Perseverance's scanning habitable environments with Raman and Luminescence for organics and chemicals (SHERLOC) investigation. *Space Sci. Rev.*, 217(4), June 2021.

[13]   Rohit Bhartia, Willam F Hug, Everett C Salas, Ray D Reid, Kripa K Sijapati, Alexandre Tsapin, William Abbey, Kenneth H Nealson, Arthur L Lane, and Pamela G Conrad. Classification of organic and biological materials with deep ultraviolet excitation. *Appl. Spectrosc.*, 62(10):1070–1077, October 2008.

[14]   Richard W. Bormett, Sanford A. Asher, Robert E. Witowski, William D. Partlow, Robert Lizewski, and Fred Pettit. Ultraviolet Raman spectroscopy characterizes chemical vapor deposition diamond film growth and oxidation. *Journal of Applied Physics*, 77(11):5916–5923, June 1995.

[15] Sergei V. Bykov, Michael Mao, Katie L. Gares, and Sanford A. Ashera. Compact solid-state 213 nm laser enables standoff deep ultraviolet raman spectrometer: Measurements of nitrate photochemistry. *Applied Spectroscopy*, 69(8):895–901, 2015.

[16] Sergei V. Bykov, Ryan D. Roppel, Michael Mao, and Sanford A. Asher. 228-nm quadrupled quasi-three-level Nd:GdVO4 laser for ultraviolet resonance Raman spectroscopy of explosives and biological molecules. *Journal of Raman Spectroscopy*, 51(12):2478–2488, 2020.

[17] Michael P. Callahan, Aaron S. Burton, Jamie E. Elsila, Eleni M. Baker, Karen E. Smith, Daniel P. Glavin, and Jason P. Dworkin. A search for amino acids and nucleobases in the Martian meteorite Roberts Massif 04262 using liquid chromatography-mass spectrometry. *Meteoritics & Planetary Science*, 48(5):786–795, May 2013.

[18] B L Carrier, W J Abbey, L W Beegle, R Bhartia, and Y Liu. Attenuation of ultraviolet radiation in rocks and minerals: Implications for Mars science. *J. Geophys. Res. Planets*, 124(10):2599–2612, October 2019.

[19] Xiyi Chen, Delmar S. Larsen, Stephen E. Bradforth, and Ivo H. M. van Stokkum. Broadband spectral probing revealing ultrafast photochemical branching after ultraviolet excitation of the aqueous phenolate anion. *The Journal of Physical Chemistry A*, 115(16):3807–3819, 2011.

[20] Zhenhuan Chi, X. G. Chen, Janet S. W. Holtz, and Sanford A. Asher. UV resonance raman-selective amide vibrational enhancement: Quantitative methodology for determining protein secondary structure. *Biochemistry*, 37(9):2854–2864, 1998.

[21] Arthur C. Clark. *Profiles of the Future: An Inquiry Into the Limits of the Possible*. Gollancz, London, UK, 2013.

[22] S J Clemett, C R Maechling, R N Zare, P D Swan, and R M Walker. Identification of complex aromatic molecules in individual interplanetary dust particles. *Science*, 262(5134):721–725, October 1993.

[23] E Cloutis, K Mccormack, J Belliii, A Hendrix, D Bailey, M Craig, S Mertzman, M Robinson, and M Riner. Ultraviolet spectral reflectance properties of common planetary minerals. *Icarus*, 197(1):321–347, September 2008.

[24] Richard W Court, Mark A Sephton, John Parnell, and Iain Gilmour. The alteration of organic matter in response to ionising irradiation: Chemical trends and implications

for extraterrestrial sample analysis. *Geochim. Cosmochim. Acta*, 70(4):1020–1039, February 2006.

[25] Ivica Dimitrovski, Ivan Kitanovski, Dragi Kocev, and Nikola Simidjievski. Current trends in deep learning for Earth Observation: An open-source benchmark arena for image classification. *ISPRS Journal of Photogrammetry and Remote Sensing*, 197:18–35, March 2023.

[26] Bethany L Ehlmann, John F Mustard, Caleb I Fassett, Samuel C Schon, James W Head, III, David J Des Marais, John A Grant, and Scott L Murchie. Clay minerals in delta deposits and organic preservation potential on Mars. *Nat. Geosci.*, 1(6):355–358, June 2008.

[27] Jennifer L Eigenbrode, Roger E Summons, Andrew Steele, Caroline Freissinet, Maëva Millan, Rafael Navarro-González, Brad Sutter, Amy C McAdam, Heather B Franz, Daniel P Glavin, Paul D Archer, Jr, Paul R Mahaffy, Pamela G Conrad, Joel A Hurowitz, John P Grotzinger, Sanjeev Gupta, Doug W Ming, Dawn Y Sumner, Cyril Szopa, Charles Malespin, Arnaud Buch, and Patrice Coll. Organic matter preserved in 3-billion-year-old mudstones at Gale crater, Mars. *Science*, 360(6393):1096–1101, June 2018.

[28] Energetiq. EQ-99X LDLS, 2023.

[29] K A Farley, K M Stack, D L Shuster, B H N Horgan, J A Hurowitz, J D Tarnas, J I Simon, V Z Sun, E L Scheller, K R Moore, S M McLennan, P M Vasconcelos, R C Wiens, A H Treiman, L E Mayhew, O Beyssac, T V Kizovski, N J Tosca, K H Williford, L S Crumpler, L W Beegle, J F Bell, 3rd, B L Ehlmann, Y Liu, J N Maki, M E Schmidt, A C Allwood, H E F Amundsen, R Bhartia, T Bosak, A J Brown, B C Clark, A Cousin, O Forni, T S J Gabriel, Y Goreva, S Gupta, S-E Hamran, C D K Herd, K Hickman-Lewis, J R Johnson, L C Kah, P B Kelemen, K B Kinch, L Mandon, N Mangold, C Quantin-Nataf, M S Rice, P S Russell, S Sharma, S Siljeström, A Steele, R Sullivan, M Wadhwa, B P Weiss, A J Williams, B V Wogsland, P A Willis, T A Acosta-Maeda, P Beck, K Benzerara, S Bernard, A S Burton, E L Cardarelli, B Chide, E Clavé, E A Cloutis, B A Cohen, A D Czaja, V Debaille, E Dehouck, A G Fairén, D T Flannery, S Z Fleron, T Fouchet, J Frydenvang, B J Garczynski, E F Gibbons, E M Hausrath, A G Hayes, J Henneke, J L Jørgensen, E M Kelly, J Lasue, S Le Mouélic, J M Madariaga, S Maurice, M Merusi, P-Y Meslin, S M Milkovich, C C Million, R C Moeller, J I Núñez, A M Ollila, G Paar, D A Paige, D A K Pedersen, P Pilleri, C Pilorget, P C Pinet, J W Rice, Jr, C Royer, V Sautter, M Schulte, M A Sephton, S K Sharma, S F Sholes, N Spanovich, M St Clair, C D Tate, K Uckert, S J VanBommel, A G Yanchilina, and M-P Zorzano. Aqueously altered igneous rocks sampled on the floor of Jezero crater, Mars. *Science*, 377(6614):eabo2196, September 2022.

[30] Kenneth A Farley, Kenneth H Williford, Kathryn M Stack, Rohit Bhartia, Al Chen, Manuel de la Torre, Kevin Hand, Yulia Goreva, Christopher D K Herd, Ricardo Hueso, Yang Liu, Justin N Maki, German Martinez, Robert C Moeller, Adam Nelessen, Claire E Newman, Daniel Nunes, Adrian Ponce, Nicole Spanovich, Peter A Willis, Luther W Beegle, James F Bell, III, Adrian J Brown, Svein-Erik Hamran, Joel A Hurowitz, Sylvestre Maurice, David A Paige, Jose A Rodriguez-Manfredi, Mitch Schulte, and Roger C Wiens. Mars 2020 mission overview. *Space Sci. Rev.*, 216(8), December 2020.

[31] John R. Ferraro, Kazuo Nakamoto, and Chris W. Brown. Basic Theory. In *Introductory Raman Spectroscopy*, pages 1–94. Elsevier Science, San Diego, CA, 2003.

[32] John R. Ferraro, Kazuo Nakamoto, and Chris W. Brown. Instrumentation and Experimental Techniques. In *Introductory Raman Spectroscopy*, pages 95–146. Elsevier Science, San Diego, CA, 2003.

[33] Marisia A. Fikiet, Shelby R. Khandasammy, Ewelina Mistek, Yasmine Ahmed, Lenka Halámková, Justin Bueno, and Igor K. Lednev. Forensics: Evidence examination via Raman spectroscopy. *Physical Sciences Reviews*, 4(2), February 2019.

[34] G J Flynn. The delivery of organic matter from asteroids and comets to the early surface of Mars. *Earth Moon Planets*, 72(1-3):469–474, 1996.

[35] Teresa Fornaro, Andrew Steele, and John Robert Brucato. Catalytic/protective properties of Martian minerals and implications for possible origin of life on Mars. *Life (Basel)*, 8(4):56, November 2018.

[36] A C Fox, J L Eigenbrode, and K H Freeman. Radiolysis of macromolecular organic material in Mars-relevant mineral matrices. *J. Geophys. Res. Planets*, 124(12):3257–3266, December 2019.

[37] P François, C Szopa, A Buch, P Coll, A C McAdam, P R Mahaffy, C Freissinet, D P Glavin, R Navarro-Gonzalez, and M Cabane. Magnesium sulfate as a key mineral for the detection of organic molecules on Mars using pyrolysis. *J. Geophys. Res. Planets*, 121(1):61–74, January 2016.

[38] C Freissinet, D P Glavin, P R Mahaffy, K E Miller, J L Eigenbrode, R E Summons, A E Brunner, A Buch, C Szopa, P D Archer, H B Franz, S K Atreya, W B Brinckerhoff, M Cabane, P Coll, P G Conrad, D J Des Marais, J P Dworkin, A G Fairén, P François, J P Grotzinger, S Kashyap, I L Ten Kate, L A Leshin, C A Malespin, M G Martin, F J Martin-Torres, A C McAdam, D W Ming, R Navarro-González, A A Pavlov, B D

Prats, S W Squyres, A Steele, J C Stern, D Y Sumner, B Sutter, and M-P Zorzano. Organic molecules in the Sheepbed mudstone, Gale Crater, Mars. *J. Geophys. Res. Planets*, 120(3):495–514, March 2015.

[39]   Marc D Fries, Carina Lee, Rohit Bhartia, Joseph Razzell Hollis, Luther W Beegle, Kyle Uckert, Trevor G Graff, William Abbey, Zachary Bailey, Eve L Berger, Aaron S Burton, Michael J Callaway, Emily L Cardarelli, Kristine N Davis, Lauren DeFlores, Kenneth S Edgett, Allison C Fox, Daniel H Garrison, Nikole C Haney, Roger S Harrington, Ryan S Jakubek, Megan R Kennedy, Keyron Hickman-Lewis, Francis M McCubbin, Ed Miller, Brian Monacelli, Randy Pollock, Richard Rhodes, Sandra Siljeström, Sunanda Sharma, Caroline L Smith, Andrew Steele, Margarite Sylvia, Vinh D Tran, Ryan H Weiner, Anastasia G Yanchilina, and R Aileen Yingst. The SHERLOC Calibration Target on the Mars 2020 Perseverance rover: Design, operations, outreach, and future human exploration functions. *Space Sci. Rev.*, 218(6), September 2022.

[40]   R L Frost and J T Kloprogge. Raman spectroscopy of the acetates of sodium, potassium and magnesium at liquid nitrogen temperature. *J. Mol. Struct.*, 526(1-3):131–141, August 2000.

[41]   M. Gaft and L. Nagli. UV gated Raman spectroscopy for standoff detection of explosives. *Optical Materials*, 30(11):1739–1746, 2008.

[42]   M. Gaft and Y. Raichlin. Luminescence of 5d–4f transitions of Pr3+ in natural fluorite CaF2, anhydrite CaSO4 and apatite Ca5(PO4)3F. *Physics and Chemistry of Minerals*, 47(1):5, January 2020.

[43]   Michael Gaft and Gerard Panczer. Laser-induced time-resolved luminescence spectroscopy of minerals: A powerful tool for studying the nature of emission centres. *Mineralogy and Petrology*, 107(3):363–372, June 2013.

[44]   Katie L. Gares, Kyle T. Hufziger, Sergei V. Bykov, and Sanford A. Asher. Review of explosive detection methodologies and the emergence of standoff deep UV resonance Raman. *Journal of Raman Spectroscopy*, 47(1):124–141, 2016.

[45]   Daniel P. Glavin, Jeffrey L. Bada, Karen L. F. Brinton, and Gene D. McDonald. Amino acids in the Martian meteorite Nakhla. *Proceedings of the National Academy of Sciences*, 96(16):8835–8838, 1999.

[46] G. Grabner, G. Koehler, J. Zechner, and N. Getoff. Temperature dependence of photoprocesses in aqueous phenol. *The Journal of Physical Chemistry*, 84(23):3000–3004, 1980.

[47] W P Griffith. Raman studies on rock-forming minerals. Part I. Orthosilicates and cyclosilicates. *J. Chem. Soc.*, page 1372, 1969.

[48] Daniel C. Harris and Michael D. Bertolucci. Electronic spectroscopy. In *Symmetry and Spectroscopy*, pages 307–419. Dover Publications, Inc., New York, NY, 1978.

[49] Daniel C. Harris and Michael D. Bertolucci. Vibrationl spectroscopy. In *Symmetry and Spectroscopy*, pages 93–224. Dover Publications, Inc., New York, NY, 1978.

[50] Chris Hicks, Mark Kalatsky, Richard A. Metzler, and Alexander O. Goushcha. Quantum efficiency of silicon photodiodes in the near-infrared spectral range. *Applied Optics*, 42(22):4415, August 2003.

[51] S Holm-Alwmark, K M Kinch, M D Hansen, S Shahrzad, K Svennevig, W J Abbey, R B Anderson, F J Calef, III, S Gupta, E Hauber, B H N Horgan, L C Kah, J Knade, N B Miklusicak, K M Stack, V Z Sun, J D Tarnas, and C Quantin-Nataf. Stratigraphic relationships in jezero crater, mars: Constraints on the timing of fluvial-lacustrine activity from orbital observations. *J. Geophys. Res. Planets*, 126(7), July 2021.

[52] Zhenmin Hong and Sanford A Asher. Dependence of Raman and Resonance Raman Intensities on Sample Self-Absorption. *Applied Spectroscopy*, 69(1):75–83, 2015.

[53] Qichao Hou, Dewen Cheng, Yang Li, Tian Zhang, DanYang Li, Yilun Huang, Hailong Chen, Qiwei Wang, Weihong Hou, Tong Yang, and Yongtian Wang. Stray light analysis and suppression method of a pancake virtual reality head-mounted display. *Optics Express*, 30(25):44918–44932, December 2022.

[54] James D. Ingle and Stanley R. Crouch. Infrared Spectrometry. In *Spectrochemical Measurements*, pages 404–437. Prentice-Hall, Inc., Englewood Cliffs, NJ, international edition edition, 1988.

[55] James D. Ingle and Stanley R. Crouch. Molecular Luminescence Spectrometry. In *Spectrochemical Measurements*, pages 438–493. Prentice-Hall, Inc., Englewood Cliffs, NJ, international edition edition, 1988.

[56] James D. Ingle and Stanley R. Crouch. Molecular Scattering Methods. In *Spectrochemical Analysis*, pages 494–524. Prentice-Hall, Inc., Englewood Cliffs, NJ, international edition edition, 1988.

[57] James D. Ingle and Stanley R. Crouch. Optical Components of Spectrometers. In *Spectrochemical Analysis*, pages 30–86. Prentice-Hall, Inc., Englewood Cliffs, NJ, international edition edition, 1988.

[58] James D. Ingle and Stanley R. Crouch. Optical Sources, Transducers, and Measurement Systems. In *Spectrochemical Analysis*, pages 87–134. Prentice-Hall, Inc., Englewood Cliffs, NJ, international edition edition, 1988.

[59] James D. Ingle and Stanley R. Crouch. Spectrochemical Information. In *Spectrochemical Analysis*, pages 1–12. Prentice-Hall, Inc., Englewood Cliffs, NJ, international edition edition, 1988.

[60] James D. Ingle and Stanley R. Crouch. Spectrochemical Measurements. In *Spectrochemical Analysis*, pages 13–29. Prentice-Hall, Inc., Englewood Cliffs, NJ, international edition edition, 1988.

[61] Ryan S. Jakubek, Stephen E. White, and Sanford A. Asher. UV resonance raman structural characterization of an (in)soluble polyglutamine peptide. *The Journal of Physical Chemistry B*, 123(8):1749–1763, 2019.

[62] John Jankovic, Burton R. Ogle, Tracy L. Zontek, Michael D. Biegalski, Scott M. Hollenbeck, and Tina M. Wells. Suitability of polycarbonate safety glasses for UV laser eye protection. *Journal of Chemical Health and Safety*, 23(2):29–33, March 2016.

[63] Elizabeth A. Jaramillo, Samuel H. Royle, Mark W. Claire, Samuel P. Kounaves, and Mark A. Sephton. Indigenous Organic-Oxidized Fluid Interactions in the Tissint Mars Meteorite. *Geophysical Research Letters*, 46(6):3090–3098, March 2019.

[64] Craig R. Johnson, Michael. Ludwig, and Sanford A. Asher. Ultraviolet resonance Raman characterization of photochemical transients of phenol, tyrosine, and tryptophan. *Journal of the American Chemical Society*, 108(5):905–912, 1986.

[65] Craig R. Johnson, Michael Ludwig, Stephen O'Donnell, and Sanford A. Asher. UV resonance Raman spectroscopy of the aromatic amino acids and myoglobin. *Journal of the American Chemical Society*, 106(17):5008–5010, 1984.

[66] Colleen M. Jones, Valentino L. Devito, Paul A. Harmon, and Sanford A. Asher. High-repetition-rate excimer-based UV laser excitation source avoids saturation in resonance raman measurements of tyrosinate and pyrene. *Applied Spectroscopy*, 41(8):1268–1275, 1987.

[67] Trace Jordan, Janina C. Eads, and Thomas G. Spiro. Secondary and tertiary structure of the A-state of cytochrome c from resonance Raman spectroscopy. *Protein Science*, 4(4):716–728, 1995.

[68] Michael Kasha. Characterization of Electronic Transitions in Complex Molecules. *Discussion of the Faraday Society*, 9:14–19, 1950.

[69] Sergey Kobtsev, Stepan Kandrushin, and Andrey Potekhin. Long-term frequency stabilization of a continuous-wave tunable laser with the help of a precision wave-lengthmeter. *Applied Optics*, 46(23):5840–5843, August 2007.

[70] Martin Kögler and Bryan Heilala. Time-gated Raman spectroscopy – a review. *Measurement Science and Technology*, 32(1):012002, January 2020.

[71] T. Kozu, M. Yamaguchi, M. Kawaguchi, H. Shima, J. W. Kim, M. Matsuoka, K. Nishida, and T. Yamamoto. Evaluating of diamond like carbon using deep UV raman spectroscopy. *Integrated Ferroelectrics*, 157(1):147–156, 2014.

[72] Alexander Kramida, Yuri Ralchenko, Joseph Reader, and NIST ASD Team. NIST Atomic Spectra Database (version 5.10), [Online].

[73] M R Krbetschek, J Götze, A Dietrich, and T Trautmann. Spectral information from minerals relevant for luminescence dating. *Radiat. Meas.*, 27(5-6):695–748, December 1997.

[74] Vikas Kumar, Tim Holtum, Jens Voskuhl, Michael Giese, Thomas Schrader, and Sebastian Schlücker. Prospects of ultraviolet resonance Raman spectroscopy in supramolecular chemistry on proteins. *Spectrochimica Acta Part A: Molecular and Biomolecular Spectroscopy*, 254:119622, 2021.

[75] Dmitry Kurouski, Jacqueline Washington, Mehmet Ozbil, Rajeev Prabhakar, Alexander Shekhtman, and Igor K. Lednev. Disulfide bridges remain intact while native insulin converts into amyloid fibrils. *PLOS ONE*, 7(6):1–9, June 2012.

[76] Judith Langer, Dorleta Jimenez de Aberasturi, Javier Aizpurua, Ramon A. Alvarez-Puebla, Baptiste Auguié, Jeremy J. Baumberg, Guillermo C. Bazan, Steven E. J. Bell, Anja Boisen, Alexandre G. Brolo, Jaebum Choo, Dana Cialla-May, Volker Deckert, Laura Fabris, Karen Faulds, F. Javier García de Abajo, Royston Goodacre, Duncan Graham, Amanda J. Haes, Christy L. Haynes, Christian Huck, Tamitake Itoh, Mikael Käll, Janina Kneipp, Nicholas A. Kotov, Hua Kuang, Eric C. Le Ru, Hiang Kwee Lee, Jian-Feng Li, Xing Yi Ling, Stefan A. Maier, Thomas Mayerhöfer, Martin Moskovits, Kei Murakoshi, Jwa-Min Nam, Shuming Nie, Yukihiro Ozaki, Isabel Pastoriza-Santos, Jorge Perez-Juste, Juergen Popp, Annemarie Pucci, Stephanie Reich, Bin Ren, George C. Schatz, Timur Shegai, Sebastian Schlücker, Li-Lin Tay, K. George Thomas, Zhong-Qun Tian, Richard P. Van Duyne, Tuan Vo-Dinh, Yue Wang, Katherine A. Willets, Chuanlai Xu, Hongxing Xu, Yikai Xu, Yuko S. Yamamoto, Bing Zhao, and Luis M. Liz-Marzán. Present and Future of Surface-Enhanced Raman Scattering. *ACS Nano*, 14(1):28–117, January 2020.

[77] Laser Institute of America. American National Standard for Safe Use of Lasers, Z136.1, 2014.

[78] J M T Lewis, J L Eigenbrode, G M Wong, A C McAdam, P D Archer, B Sutter, M Millan, R H Williams, M Guzman, A Das, E B Rampe, C N Achilles, H B Franz, S Andrejkovičová, C A Knudson, and P R Mahaffy. Pyrolysis of oxalate, acetate, and perchlorate mixtures and the implications for organic salts on mars. *J. Geophys. Res. Planets*, 126(4), April 2021.

[79] Jinchao Liu, Margarita Osadchy, Lorna Ashton, Michael Foster, Christopher J. Solomon, and Stuart J. Gibson. Deep convolutional neural networks for Raman spectrum recognition: A unified solution. *The Analyst*, 142(21):4067–4074, 2017.

[80] Y. Liu. An olivine cumulate outcrop on the floor of Jezero crater, Mars. *Science*, 377(6614):1513–1519, 2022.

[81] Yang Liu, Chi Ma, John R Beckett, Yang Chen, and Yunbin Guan. Rare-earth-element minerals in martian breccia meteorites NWA 7034 and 7533: Implications for fluid–rock interaction in the martian crust. *Earth Planet. Sci. Lett.*, 451:251–262, October 2016.

[82] Derek Long. Introduction to theoretical treatments of incoherent light scattering. In *The Raman Effect*, pages 19–29. John Wiley & Sons, Ltd, 2002.

[83] Derek Long. Normal and Resonance Electronic and Vibronic Raman Scattering. In *The Raman Effect*, pages 289–302. John Wiley & Sons, Ltd, 2002.

[84] Derek Long. Quantum Mechanical Theory of Rayleigh and Raman Scattering. In *The Raman Effect*, pages 49–84. John Wiley & Sons, Ltd, 2002.

[85] Derek Long. Vibrational resonance raman scattering. In *The Raman Effect*, pages 221–270. John Wiley & Sons, Ltd, 2002.

[86] Michael Ludwig and Sanford A Asher. Ultraviolet Resonance Raman Excitation Profiles of Tyrosine: Dependence of Raman Cross Sections on Excited-State Intermediates. *Journal of the American Chemical Society*, 110(4):1005–1011, 1988.

[87] Martin Maiwald, Kay Sowoidnich, and Bernd Sumpf. Portable shifted excitation Raman difference spectroscopy for on-site soil analysis. *Journal of Raman Spectroscopy*, 53(9):1560–1570, September 2022.

[88] N Mangold, S Gupta, O Gasnault, G Dromart, J D Tarnas, S F Sholes, B Horgan, C Quantin-Nataf, A J Brown, S Le Mouélic, R A Yingst, J F Bell, O Beyssac, T Bosak, F Calef, 3rd, B L Ehlmann, K A Farley, J P Grotzinger, K Hickman-Lewis, S Holm-Alwmark, L C Kah, J Martinez-Frias, S M McLennan, S Maurice, J I Nuñez, A M Ollila, P Pilleri, J W Rice, Jr, M Rice, J I Simon, D L Shuster, K M Stack, V Z Sun, A H Treiman, B P Weiss, R C Wiens, A J Williams, N R Williams, and K H Williford. Perseverance rover reveals an ancient delta-lake system and flood deposits at Jezero crater, Mars. *Science*, 374(6568):711–717, November 2021.

[89] Richard L McCreery. Instrumentation overview and spectrometer performance. In *Raman Spectroscopy for Chemical Analysis*, pages 73–94. John Wiley & Sons, Ltd, 2000.

[90] Richard L McCreery. Lasers for raman spectroscopy. In *Raman Spectroscopy for Chemical Analysis*, pages 127–148. John Wiley & Sons, Ltd, 2000.

[91] Richard L McCreery. Magnitude of raman scattering. In *Raman Spectroscopy for Chemical Analysis*, pages 15–33. John Wiley & Sons, Ltd, 2000.

[92] Friedrich Menges. Spectragryph - optical spectroscopy software, 2023.

[93] M Millan, S Teinturier, C A Malespin, J Y Bonnet, A Buch, J P Dworkin, J L Eigenbrode, C Freissinet, D P Glavin, R Navarro-González, A Srivastava, J C Stern, B Sutter, C Szopa, A J Williams, R H Williams, G M Wong, S S Johnson, and P R Mahaffy. Organic molecules revealed in Mars's Bagnold Dunes by Curiosity's derivatization experiment. *Nat. Astron.*, 6(1):129–140, November 2021.

[94] Robert C Moeller, Louise Jandura, Keith Rosette, Matt Robinson, Jessica Samuels, Milo Silverman, Kyle Brown, Elizabeth Duffy, Aaron Yazzie, Elizabeth Jens, Iona Brockie, Lauren White, Yulia Goreva, Torsten Zorn, Avi Okon, Justin Lin, Matthew Frost, Curtis Collins, Jeffrey B Williams, Adam Steltzner, Fei Chen, and Jeff Biesiadecki. The sampling and caching subsystem (SCS) for the scientific exploration of jezero crater by the mars 2020 perseverance rover. *Space Sci. Rev.*, 217(1), February 2021.

[95] P. F. Morrissey, S. R. McCandliss, P. D. Feldman, and S. D. Friedman. Vacuum-ultraviolet quantum efficiency of a phosphor-coated charge-coupled device. *Applied Optics*, 33(13):2534, May 1994.

[96] Arka Mukherjee, Michael L. McGlashen, and Thomas G. Spiro. Ultraviolet resonance raman spectroscopy and general valence force field analysis of phenolate and phenoxyl radical. *The Journal of Physical Chemistry*, 99(14):4912–4917, 1995.

[97] Steven P. Newman, Simon J. Clifford, Peter V. Coveney, Vijay Gupta, Joanna D. Blanchard, Frank Serafin, Dor Ben-Amotz, and Sidney Diamond. Anomalous fluorescence in near-infrared Raman spectroscopy of cementitious materials. *Cement and Concrete Research*, 35(8):1620–1628, 2005.

[98] M Nickerson. A review of Pound-Drever-Hall laser frequency locking. *JILA, University of Colorado and NIST*, 2019.

[99] Abraham Nitzan. Introduction to Quantum Relaxation Processes. In *Chemical Dynamics in Condensed Phases*, pages 304–346. Oxford University Press, Oxford, UK, 2006.

[100] Abraham Nitzan. Spectroscopy. In *Chemical Dynamics in Condensed Phases*, pages 640–707. Oxford University Press, Oxford, UK, 2006.

[101] Mordechai Peleg. A Raman spectroscopic investigation of the dehydration of solid magnesium nitrate hexahydrate. *Isr. J. Chem.*, 11(4):535–541, 1973.

[102] Richard C. Prince, Renee R. Frontiera, and Eric O. Potma. Stimulated Raman Scattering: From Bulk to Nano. *Chemical Reviews*, 117(7):5070–5094, April 2017.

[103] Nicole M. Ralbovsky and Igor K. Lednev. Towards development of a novel universal medical diagnostic method: Raman spectroscopy and machine learning. *Chemical Society Reviews*, 49(20):7428–7453, 2020.

[104] C. V. Raman and K. S. Krishnan. A New Type of Secondary Radiation. *Nature*, 121(3048):501–502, March 1928.

[105] Joseph Razzell Hollis, William Abbey, Luther W Beegle, Rohit Bhartia, Bethany L Ehlmann, Jasper Miura, Brian Monacelli, Kelsey Moore, Austin Nordman, Eva Scheller, Kyle Uckert, and Yen-Hung Wu. A deep-ultraviolet Raman and Fluorescence spectral library of 62 minerals for the SHERLOC instrument onboard Mars 2020. *Planet. Space Sci.*, 209(105356):105356, December 2021.

[106] Joseph Razzell Hollis, Kelsey R Moore, Sunanda Sharma, Luther Beegle, John P Grotzinger, Abigail Allwood, William Abbey, Rohit Bhartia, Adrian J Brown, Benton Clark, Edward Cloutis, Andrea Corpolongo, Jesper Henneke, Keyron Hickman-Lewis, Joel A Hurowitz, Michael W M Jones, Yang Liu, Jesús Martinez-Frías, Ashley Murphy, David A K Pedersen, Svetlana Shkolyar, Sandra Siljeström, Andrew Steele, Mike Tice, Alan Treiman, Kyle Uckert, Scott VanBommel, and Anastasia Yanchilina. The power of paired proximity science observations: Co-located data from SHERLOC and PIXL on Mars. *Icarus*, 387(115179):115179, November 2022.

[107] Joseph Razzell Hollis, Sunanda Sharma, William Abbey, Rohit Bhartia, Luther Beegle, Marc Fries, Jeffrey D Hein, Brian Monacelli, and Austin D Nordman. A deep ultraviolet Raman and fluorescence spectral Library of 51 organic compounds for the SHERLOC instrument onboard mars 2020. *Astrobiology*, 23(1):1–23, January 2023.

[108] Renata Reisfeld, Michael Gaft, and Gerard Panczer. *Modern Luminescence Spectroscopy of Minerals and Materials.* Springer, Berlin, Germany, 2005 edition, July 2004.

[109] Jane K. Rice and Roger W. Anderson. Two-photon, thermal lensing spectroscopy of monosubstituted benzenes in the 1B2u(1Lb) <- 1A1g(1A) and 1B1u(1La) <- 1A1g(1A) Transition Regions. *The Journal of Physical Chemistry*, 90(26):6793–6800, 1986.

[110] Richard E. Russo, Xianglei Mao, Jhanis J. Gonzalez, Vassilia Zorba, and Jong Yoo. Laser Ablation in Analytical Chemistry. *Analytical Chemistry*, 85(13):6162–6177, July 2013.

[111] M R Salvatore, T A Goudge, M S Bramble, C S Edwards, J L Bandfield, E S Amador, J F Mustard, and P R Christensen. Bulk mineralogy of the NE Syrtis and Jezero crater regions of Mars derived through thermal infrared spectral analyses. *Icarus*, 301:76–96, February 2018.

[112] Haley M. Sapers, Joseph Razzell Hollis, Rohit Bhartia, Luther W. Beegle, Victoria J. Orphan, and Jan P. Amend. The cell and the sum of its parts: Patterns of complexity in biosignatures as revealed by deep UV raman spectroscopy. *Frontiers in Microbiology*, 10, 2019.

[113] Eva L Scheller, Joseph Razzell Hollis, Emily L Cardarelli, Andrew Steele, Luther W Beegle, Rohit Bhartia, Pamela Conrad, Kyle Uckert, Sunanda Sharma, Bethany L Ehlmann, William J Abbey, Sanford A Asher, Kathleen C Benison, Eve L Berger, Olivier Beyssac, Benjamin L Bleefeld, Tanja Bosak, Adrian J Brown, Aaron S Burton, Sergei V Bykov, Ed Cloutis, Alberto G Fairén, Lauren DeFlores, Kenneth A Farley, Deidra M Fey, Teresa Fornaro, Allison C Fox, Marc Fries, Keyron Hickman-Lewis, William F Hug, Joshua E Huggett, Samara Imbeah, Ryan S Jakubek, Linda C Kah, Peter Kelemen, Megan R Kennedy, Tanya Kizovski, Carina Lee, Yang Liu, Lucia Mandon, Francis M McCubbin, Kelsey R Moore, Brian E Nixon, Jorge I Núñez, Carolina Rodriguez Sanchez-Vahamonde, Ryan D Roppel, Mitchell Schulte, Mark A Sephton, Shiv K Sharma, Sandra Siljeström, Svetlana Shkolyar, David L Shuster, Justin I Simon, Rebecca J Smith, Kathryn M Stack, Kim Steadman, Benjamin P Weiss, Alyssa Werynski, Amy J Williams, Roger C Wiens, Kenneth H Williford, Kathrine Winchell, Brittan Wogsland, Anastasia Yanchilina, Rachel Yingling, and Maria-Paz Zorzano. Aqueous alteration processes in Jezero crater, Mars-implications for organic geochemistry. *Science*, 378(6624):1105–1110, December 2022.

[114] Michael Schmid, David Rath, and Ulrike Diebold. Why and how Savitzky-Golay filters should be replaced. *ACS Meas. Sci. Au*, 2(2):185–196, April 2022.

[115] J William Schopf, Jack D Farmer, Ian S Foster, Anatoliy B Kudryavtsev, Victor A Gallardo, and Carola Espinoza. Gypsum-permineralized microfossils and their relevance to the search for life on Mars. *Astrobiology*, 12(7):619–633, July 2012.

[116] Mark A. Sephton. Organic compounds in carbonaceous meteorites. *Nat. Prod. Rep.*, 19(3):292–311, 2002.

[117] Bhavya Sharma and Sanford A. Asher. UV Resonance Raman Finds Peptide Bond-Arg Side Chain Electronic Interactions. *The Journal of Physical Chemistry B*, 115(18):5659–5664, May 2011.

[118] C K Shearer, P V Burger, J J Papike, F M McCubbin, and A S Bell. Crystal chemistry of merrillite from Martian meteorites: Mineralogical recorders of magmatic processes and planetary differentiation. *Meteorit. Planet. Sci.*, 50(4):649–673, April 2015.

[119] S Shkolyar, E Lalla, M Konstantindis, K Cote, M G Daly, and A Steele. Detecting Ce3+ as a biosignature mimicker using UV time-resolved laser-induced fluorescence and Raman spectroscopy: Implications for planetary missions. *Icarus*, 354(114093):114093, January 2021.

[120] David H. Sliney. UV radiation ocular exposure dosimetry. *Documenta Ophthalmologica*, 88(3):243–254, March 1995.

[121] George Socrates. *Infrared and Raman Characteristic Group Frequencies: Tables and Charts*. John Wiley & Sons, 2004.

[122] Kathryn M Stack, Nathan R Williams, Fred Calef, 3rd, Vivian Z Sun, Kenneth H Williford, Kenneth A Farley, Sigurd Eide, David Flannery, Cory Hughes, Samantha R Jacob, Linda C Kah, Forrest Meyen, Antonio Molina, Cathy Quantin Nataf, Melissa Rice, Patrick Russell, Eva Scheller, Christina H Seeger, William J Abbey, Jacob B Adler, Hans Amundsen, Ryan B Anderson, Stanley M Angel, Gorka Arana, James Atkins, Megan Barrington, Tor Berger, Rose Borden, Beau Boring, Adrian Brown, Brandi L Carrier, Pamela Conrad, Henning Dypvik, Sarah A Fagents, Zachary E Gallegos, Brad Garczynski, Keenan Golder, Felipe Gomez, Yulia Goreva, Sanjeev Gupta, Svein-Erik Hamran, Taryn Hicks, Eric D Hinterman, Briony N Horgan, Joel Hurowitz, Jeffrey R Johnson, Jeremie Lasue, Rachel E Kronyak, Yang Liu, Juan Manuel Madariaga, Nicolas Mangold, John McClean, Noah Miklusicak, Daniel Nunes, Corrine Rojas, Kirby Runyon, Nicole Schmitz, Noel Scudder, Emily Shaver, Jason SooHoo, Russell Spaulding, Evan Stanish, Leslie K Tamppari, Michael M Tice, Nathalie Turenne, Peter A Willis, and R Aileen Yingst. Photogeologic map of the Perseverance rover field site in Jezero crater constructed by the Mars 2020 Science Team. *Space Sci. Rev.*, 216(8), December 2020.

[123] A Steele, L G Benning, R Wirth, A Schreiber, T Araki, F M McCubbin, M D Fries, L R Nittler, J Wang, L J Hallis, P G Conrad, C Conley, S Vitale, A C O'Brien, V Riggi, and K Rogers. Organic synthesis associated with serpentinization and carbonation on early Mars. *Science*, 375(6577):172–177, January 2022.

[124] A Steele, L G Benning, R Wirth, S Siljeström, M D Fries, E Hauri, P G Conrad, K Rogers, J Eigenbrode, A Schreiber, A Needham, J H Wang, F M McCubbin, D Kilcoyne, and Juan Diego Rodriguez Blanco. Organic synthesis on Mars by electrochemical reduction of CO2. *Sci. Adv.*, 4(10):eaat5118, October 2018.

[125] A Steele, F M McCubbin, M Fries, L Kater, N Z Boctor, M L Fogel, P G Conrad, M Glamoclija, M Spencer, A L Morrow, M R Hammond, R N Zare, E P Vicenzi, S Siljeström, R Bowden, C D K Herd, B O Mysen, S B Shirey, H E F Amundsen,

A H Treiman, E S Bullock, and A J T Jull. A reduced organic carbon component in martian basalts. *Science*, 337(6091):212–215, July 2012.

[126] Andrew Steele, Francis M McCubbin, and Marc D Fries. The provenance, formation, and implications of reduced carbon phases in Martian meteorites. *Meteorit. Planet. Sci.*, 51(11):2203–2225, November 2016.

[127] Vivian Sun, California Institute of Technology Jet Propulsion Laboratory, Kevin P Hand, Kenneth A Farley, Kathryn Stack Morgan, Kenneth H Williford, Sarah Milkovich, Rachel Kronyak, James Bell, III, David Shuster, and Justin I Simon. Exploring the jezero crater floor: The mars 2020 perseverance rover's first science campaign, 2021.

[128] Éva Szökő and Tamás Tábi. Analysis of biological samples by capillary electrophoresis with laser induced fluorescence detection. *Journal of Pharmaceutical and Biomedical Analysis*, 53(5):1180–1192, 2010.

[129] Michael M Tice, Joel A Hurowitz, Abigail C Allwood, Michael W M Jones, Brendan J Orenstein, Scott Davidoff, Austin P Wright, David A K Pedersen, Jesper Henneke, Nicholas J Tosca, Kelsey R Moore, Benton C Clark, Scott M McLennan, David T Flannery, Andrew Steele, Adrian J Brown, Maria-Paz Zorzano, Keyron Hickman-Lewis, Yang Liu, Scott J VanBommel, Mariek E Schmidt, Tanya V Kizovski, Allan H Treiman, Lauren O'Neil, Alberto G Fairén, David L Shuster, Sanjeev Gupta, and PIXL Team. Alteration history of Séítah formation rocks inferred by PIXL x-ray fluorescence, x-ray diffraction, and multispectral imaging on Mars. *Sci. Adv.*, 8(47):eabp9084, November 2022.

[130] Kyle Uckert, Rohit Bhartia, Luther W. Beegle, Brian Monacelli, Sanford A. Asher, Aaron S. Burton, Sergei V. Bykov, Kristine Davis, Marc D. Fries, Ryan S. Jakubek, Joseph Razzell Hollis, Ryan D. Roppel, and Yen-Hung Wu. Calibration of the SHER-LOC Deep Ultraviolet Fluorescence–Raman Spectrometer on the Perseverance Rover. *Applied Spectroscopy*, 75(7):763–773, July 2021.

[131] Pauli Virtanen, Ralf Gommers, Travis E. Oliphant, Matt Haberland, Tyler Reddy, David Cournapeau, Evgeni Burovski, Pearu Peterson, Warren Weckesser, Jonathan Bright, Stéfan J. van der Walt, Matthew Brett, Joshua Wilson, K. Jarrod Millman, Nikolay Mayorov, Andrew R. J. Nelson, Eric Jones, Robert Kern, Eric Larson, C. J. Carey, İlhan Polat, Yu Feng, Eric W. Moore, Jake VanderPlas, Denis Laxalde, Josef Perktold, Robert Cimrman, Ian Henriksen, E. A. Quintero, Charles R. Harris, Anne M. Archibald, Antônio H. Ribeiro, Fabian Pedregosa, Paul van Mulbregt, Aditya Vijaykumar, Alessandro Pietro Bardelli, Alex Rothberg, Andreas Hilboll, Andreas Kloeckner, Anthony Scopatz, Antony Lee, Ariel Rokem, C. Nathan Woods, Chad

Fulton, Charles Masson, Christian Häggström, Clark Fitzgerald, David A. Nicholson, David R. Hagen, Dmitrii V. Pasechnik, Emanuele Olivetti, Eric Martin, Eric Wieser, Fabrice Silva, Felix Lenders, Florian Wilhelm, G. Young, Gavin A. Price, Gert-Ludwig Ingold, Gregory E. Allen, Gregory R. Lee, Hervé Audren, Irvin Probst, Jörg P. Dietrich, Jacob Silterra, James T. Webber, Janko Slavič, Joel Nothman, Johannes Buchner, Johannes Kulick, Johannes L. Schönberger, José Vinícius de Miranda Cardoso, Joscha Reimer, Joseph Harrington, Juan Luis Cano Rodríguez, Juan Nunez-Iglesias, Justin Kuczynski, Kevin Tritz, Martin Thoma, Matthew Newville, Matthias Kümmerer, Maximilian Bolingbroke, Michael Tartre, Mikhail Pak, Nathaniel J. Smith, Nikolai Nowaczyk, Nikolay Shebanov, Oleksandr Pavlyk, Per A. Brodtkorb, Perry Lee, Robert T. McGibbon, Roman Feldbauer, Sam Lewis, Sam Tygier, Scott Sievert, Sebastiano Vigna, Stefan Peterson, Surhud More, Tadeusz Pudlik, Takuya Oshima, Thomas J. Pingel, Thomas P. Robitaille, Thomas Spura, Thouis R. Jones, Tim Cera, Tim Leslie, Tiziano Zito, Tom Krauss, Utkarsh Upadhyay, Yaroslav O. Halchenko, Yoshiki Vázquez-Baeza, and SciPy 1.0 Contributors. SciPy 1.0: Fundamental algorithms for scientific computing in Python. *Nature Methods*, 17(3):261–272, March 2020.

[132] Daniel M Wade and Dereth J Drake. A Brief Review of Modern Uses of Scattering Techniques. *Georgie Journal of Science*, 77(2):1–11, 2019.

[133] Meenakshi Wadhwa and Ghislaine Crozaz. The igneous crystallization history of an ancient Martian meteorite from rare earth element microdistributions. *Meteorit. Planet. Sci.*, 33(4):685–692, July 1998.

[134] Rongxuan Wang, Benjamin Standfield, Chaoran Dou, Andrew C. Law, and Zhenyu James Kong. Real-time process monitoring and closed-loop control on laser power via a customized laser powder bed fusion platform. *Additive Manufacturing*, 66:103449, 2023.

[135] Dong Wei, Shuo Chen, and Quan Liu. Review of Fluorescence Suppression Techniques in Raman Spectroscopy. *Applied Spectroscopy Reviews*, 50(5):387–406, May 2015.

[136] Thomas Wriedt. A Review of Elastic Light Scattering Theories. *Particle & Particle Systems Characterization*, 15(2):67–74, April 1998.

[137] T. Yanagawa, S. Saito, and Y. Yamamoto. Frequency stabilization of 1.5-μm InGaAsP distributed feedback laser to NH3 absorption lines. *Applied Physics Letters*, 45(8):826–828, October 1984.

[138] Shengyu Yang, Hans-Martin Schulz, Brian Horsfield, Niels H Schovsbo, Kliti Grice, and Jinchuan Zhang. Geological alteration of organic macromolecules by irradiation: Implication for organic matter occurrence on Mars. *Geology*, 48(7):713–717, July 2020.

[139] Haibo Zhang, Zhijun Yuan, Jun Zhou, Jingxing Dong, Yunrong Wei, and Qihong Lou. Laser-induced fluorescence of fused silica irradiated by ArF excimer laser. *Journal of Applied Physics*, 110(1):013107, July 2011.

[140] Yinsheng Zhang, Wenhao Ma, Ruiqi Hou, Dian Rong, Xiaolin Qin, Yongbo Cheng, and Haiyan Wang. Spectroscopic profiling-based geographic herb identification by neural network with random weights. *Spectrochimica Acta Part A: Molecular and Biomolecular Spectroscopy*, 278:121348, October 2022.

[141] Zhi-Min Zhang, Shan Chen, and Yi-Zeng Liang. Baseline correction using adaptive iteratively reweighted penalized least squares. *Analyst*, 135(5):1138–1146, 2010.

[142] Janina Zięba-Palus and Aleksandra Michalska. Photobleaching as a useful technique in reducing of fluorescence in Raman spectra of blue automobile paint samples. *Vibrational Spectroscopy*, 74:6–12, 2014.